TECHNISCHE UNIVERSITÄT MÜNCHEN

Fachgebiet Organische Chemie

Optimal Robust Pulse Design for Magnetic Resonance

Yun Zhang

Vollständiger Abdruck der von der Fakultät für Chemie der Technischen Universität München zur Erlangung des akademischen Grades eines

Doktors der Naturwissenschaften

genehmigten Dissertation.

Vorsitzender:		Univ.-Prof. Dr. Bernd Reif
Prüfer der Dissertation:	1.	Univ.-Prof. Dr. Steffen J. Glaser
	2.	Assoc. Prof. Dominique Sugny, Université de Bourgogne / Frankreich

Die Dissertation wurde am 26.06.2012 bei der Technischen Universität München eingereicht und durch die Fakultät für Chemie am 20.07.2012 angenommen.

Declaration

I hereby declare that parts of this Thesis are already published/submitted or planned to be submitted in scientific journals:

List of Publications

Singular extremals for the time-optimal control of dissipative spin 1/2 particles;
M. Lapert, Y. Zhang, M. Braun, S. J. Glaser, D. Sugny, *Phys. Rev. Lett.*, **104**, 083001 (2010).

Geometric versus numerical optimal control of a spin 1/2 particle;
M. Lapert, Y. Zhang, M. Braun, S. J. Glaser, D. Sugny, *Phys. Rev. A*, **82**, 063418 (2010).

Simultaneous time-optimal control of the inversion of two spin 1/2 particles;
E. Assémat, M. Lapert, Y. Zhang, M. Braun, S. Glaser, D. Sugny, *Phys. Rev. A*, **82**, 013415 (2010).

Time-optimal control of spin 1/2 particles in presence of relaxation and radiation damping effects;
Y. Zhang, M. Lapert, M. Braun, D. Sugny, S. J. Glaser, *J. Chem. Phys.*, **134**, 054103 (2011).

Saturation of dissipative spin 1/2 particles by generalized Lyapunov control;
F. Meintert, M. Lapert, Y. Zhang, S. J. Glaser, D. Sugny, *New J. Phys.*, **13**, 073001 (2011).

Towards the time-optimal control of dissipative spin 1/2 particles in Nuclear Magnetic Resonance;
M. Lapert, Y. Zhang, S. J. Glaser, D. Sugny, *J. Phys. B*, **44**, 154014 (2011).

Shaped Optimal Control Pulses for Increased Excitation Bandwidth in EPR;
Ph. E. Spindler, Y. Zhang, B. Endeward, N. Gershernzon, T. E. Skinner, S. J. Glaser, T. F. Prisner, *J. Magn. Reson.*, **218**, 49 (2012).

Geometric optimal control of the contrast imaging problem in Nuclear Magnetic Resonance;
PB. Bonnard, O. Cots, S. J. Glaser, M. Lapert, D. Sugny, Y. Zhang, *IEEE transactions on automatic and control, to be published, 2012.*

Exploring the physical limits of contrast in Magnetic Resonance Imaging;
M. Lapert, Y. Zhang, M. Janich, S. J. Glaser, D. Sugny, *Scientific Reports, submitted, 2012*.

Optimal control of the inversion of spins in Nuclear Magnetic Resonance;
E. Assémat, L. Attar, M.-J. Penouilh, M. Picquet, A. Tabard, Y. Zhang, S. J. Glaser, D. Sugny, *Chem. Phys., submitted, 2012*.

Excitation of maximum quantum coherence: physical limits and practical pulse sequences;
Y. Zhang, S. S. Köcher, M. Reddy, S. Caldarelli, S. J. Glaser, *in preparation, 2012*.

Eidesstattliche Versicherung

Ich versichere, dass ich die von mir vorgelegte Dissertation selbständig angefertigt, die benutzten Quellen und Hilfsmittel vollständig angegeben und die Stellen der Arbeit, die anderen Werken im Wortlaut oder dem Sinn nach entnommen sind, in jedem Einzelfall als Entlehnung kenntlich gemacht habe; dass diese Dissertation noch keiner anderen Fakultät oder Universität zur Prüfung vorgelegen hat; dass sie abgesehen von unten angegebenen Teilpublikationen noch nicht veröffentlicht worden ist sowie, dass ich eine solche Veröffentlichung vor Abschluss des Promotionsverfahrens nicht vornehmen werde. Die Bestimmungen dieser Promotionsordnung sind mir bekannt. Die von mir vorgelegte Dissertation ist von Herrn Prof. Dr. S. J. Glaser betreut worden.

Publikationsliste

Singular extremals for the time-optimal control of dissipative spin 1/2 particles;
M. Lapert, Y. Zhang, M. Braun, S. J. Glaser, D. Sugny, *Phys. Rev. Lett.*, **104**, 083001 (2010).

Geometric versus numerical optimal control of a spin 1/2 particle;
M. Lapert, Y. Zhang, M. Braun, S. J. Glaser, D. Sugny, *Phys. Rev. A*, **82**, 063418 (2010).

Simultaneous time-optimal control of the inversion of two spin 1/2 particles;
E. Assémat, M. Lapert, Y. Zhang, M. Braun, S. Glaser, D. Sugny, *Phys. Rev. A*, **82**, 013415 (2010).

Time-optimal control of spin 1/2 particles in presence of relaxation and radiation damping effects;
Y. Zhang, M. Lapert, M. Braun, D. Sugny, S. J. Glaser, *J. Chem. Phys.*, **134**, 054103 (2011).

Saturation of dissipative spin 1/2 particles by generalized Lyapunov control;
F. Meintert, M. Lapert, Y. Zhang, S. J. Glaser, D. Sugny, *New J. Phys.*, **13**, 073001 (2011).

Towards the time-optimal control of dissipative spin 1/2 particles in Nuclear Magnetic Resonance;
M. Lapert, Y. Zhang, S. J. Glaser, D. Sugny, *J. Phys. B*, **44**, 154014 (2011).

Shaped Optimal Control Pulses for Increased Excitation Bandwidth in EPR;
Ph. E. Spindler, Y. Zhang, B. Endeward, N. Gershernzon, T. E. Skinner, S. J. Glaser, T. F. Prisner, *J. Magn. Reson.*, **218**, 49 (2012).

Geometric optimal control of the contrast imaging problem in Nuclear Magnetic Resonance;
PB. Bonnard, O. Cots, S. J. Glaser, M. Lapert, D. Sugny, Y. Zhang, *IEEE transactions on automatic and control, to be published, 2012.*

Exploring the physical limits of contrast in Magnetic Resonance Imaging;
M. Lapert, Y. Zhang, M. Janich, S. J. Glaser, D. Sugny, *Scientific Reports, submitted, 2012.*

Optimal control of the inversion of spins in Nuclear Magnetic Resonance;
E. Assémat, L. Attar, M.-J. Penouilh, M. Picquet, A. Tabard, Y. Zhang, S. J. Glaser, D. Sugny, *Chem. Phys., submitted, 2012.*

Excitation of maximum quantum coherence: physical limits and practical pulse sequences;
Y. Zhang, S. S. Köcher, M. Reddy, S. Caldarelli, S. J. Glaser, *in preparation, 2012.*

Abstract

Magnetic Resonance has become a powerful tool to study the state of matter in a variety of domains extending from biology and chemistry to solid-state physics and medicine. This thesis is concerned with the pulse design and development in magnetic resonance, with the use of optimal control theory (Chapter 2). Different applications include: the saturation of an NMR signal for a single spin 1/2 with relaxation (Chapter 3) and radiation damping effect (Chapter 4); excitation of the maximum quantum coherence for coupled homonuclear spin system (Chapter 5); maximization of the saturation contrast between two spins with different relaxation times in magnetic resonance imaging (Chapter 6); excitation for the increased bandwidth in electron paramagnetic resonance (Chapter 7). Some of the optimal control problems are solved both by using geometric methods and the Gradient Ascent Pulse Engineering (GRAPE) algorithm. The results of these two methds are also compared in the thesis.

Zusammenfassung

Magnetresonanz ist ein mächtiges Werkzeug geworden, um den Zustand von Materie in verschiedenen Domänen, die von Biologie und Chemie bis zu der Festkörperphysik und der Medizin reichen, zu studieren. Die Arbeit beschäftigt sich mit dem Pulsedesign und der Pulsesequenz-Entwicklung in der Magnetresonanztomographie mit Hilfe der Theorie der optimalen Steuerung (Kapitel 2). Verschiedene Anwendungen sind: die Sättigung eines NMR-Signals für einen einzelnen Spin 1/2 mit Relaxation (Kapitel 3) und radiation damping (Kapitel 4); Anregung der maximale Quanten-Kohärenz für gekoppelte homonucleare Spinsysteme (Kapitel 5); Maximierung des Sättigungs-Kontrasts zwischen zwei Spins mit verschiedenen Relaxationszeiten in der Magnetresonanztomographie (Kapitel 6); Anregung für die erhöhte Bandbreite in der Elektronenspin-Resonanz (Kapitel 7). Einige Probleme der optimalen Steuerung werden sowohl durch geometrische Methoden gelöst als auch durch den GRAPE-Algorithmus (Gradient Ascent Pulse Engineering). Die Ergebnisse beider Methoden werden in der Arbeit miteinander verglichen.

Contents

Abbreviations

- NMR: Nuclear Magnetic Resonance
- MRI: Magnetic Resonance Imaging
- EPR: Electron Paramagnetic Resonance
- PMP: Pontryagin Maximum Principle
- GM: Geometric Approach
- GRAPE: Gradient Ascent Pulse Engineering
- RF: Radio Frequency
- B_0: The Static magnetic field
- B_1: The radio frequency magnetic field
- T_1: Longitudinal relaxation time
- T_2: Transverse relaxation time
- MAXQ: Maximum Quantum coherence
- T_p or t_p: Total pulse duration
- BW: Band Width
- SLR: Shinnar-LeRoux algorithm
- TOP: Time Optimal Pulse curve

List of Figures

List of Tables

Chapter 1

Introduction

Since its discovery in the forties, Nuclear Magnetic Resonance (NMR) has become a powerful tool to study the state of matter in a variety of domains extending from biology and chemistry to solid-state physics and quantum computing. The power of magnetic resonance techniques can also be illustrated by medical imaging, which is a very important tool in medicine to produce diagnostics and to prepare surgical operation, as well as in the field of electron paramagnetic resonance (EPR) spectroscopy for the detection and identification of free radicals and paramagnetic centers.

However, fundamental problems in magnetic resonance are still unsolved, like how to steer a magnetization vector from a given initial state in an efficient way (like in minimum time or with minimum rf energy) to a desired target state including physical effects such as relaxation, radiation damping and experimental constraints such as limited pulse amplitude or pulse power, as well as possible experimental imperfections. My work focuses on solving the above question by the design of highly robust pulses to efficiently transfer the initial state to a target state for different practical applications under realistic conditions.

- **Chapter 2**

  Chapter 2 gives an overview of the basic optimal control methodologies and the general procedures of the numerical optimization, as well as its link and comparison with the geometric methods.

- **Chapter 3**

  The problem of saturation of an NMR signal for a single spin 1/2 with relaxation is analyzed with optimal control theory. This method can be useful to suppress a specific NMR signal. Both the problems of minimizing the duration of the control and its energy for a fixed duration are considered. The optimal control problems are solved by using geometric methods and a purely numerical approach, the GRAPE algorithm. A very good agreement is obtained between the two results. The optimal solutions are also implemented experimentally with available NMR techniques.

- **Chapter 4**

  Here the problem of Chapter 3 is extended to an ensemble of uncoupled spin 1/2 particles in the presence of both relaxation and radiation damping effects. The dynamics of radiation damping is governed by non-linear equations generalizing the standard linear Bloch equations. For a single spin, the optimal control strategy

can be fully characterized analytically. However, in order to take into account the inhomogeneity of the static magnetic field, an ensemble of isochromats at different frequencies must be considered. For this case, numerically optimized pulse sequences are computed and the dynamics under the corresponding optimal field is experimentally demonstrated using nuclear magnetic resonance techniques.

- **Chapter 5**

  To simplify the analysis of complicated and overlapping spectra, one possibility is to explore high quantum order coherences, up to the limiting case of the maximum quantum (MaxQ) coherence, which is just a singlet for each spin system, resulting in the largest spectral simplification. However, the standard pulse sequences for MaxQ coherence generation are far from optimal and rely on long-range J coupling. Here optimal control theory is applied for pulse design of MaxQ order excitation and compare the performance of the optimized pulses with the standard approach.

- **Chapter 6**

  Magnetic Resonance Imaging has become an indispensable tool with applications ranging from medicine to material science. However, so far the physical limits of the maximum achievable experimental contrast were unknown. An approach based on principles of optimal control theory is introduced to find these physical limits, providing a benchmark for numerically optimized robust pulse sequences which can take into account experimental imperfections. This approach is demonstrated using a model system of two spatially separated liquids corresponding to blood in its oxygenated and deoxygenated forms.

- **Chapter 7**

  In this chapter, the development of optimal control based pulses for broadband excitation in electron spin resonance spectroscopy is presented. In collaboration with the group of Prof. T. Prisner (University of Frankfurt), the pulses were implemented and tested experimentally at X-band frequency (9 GHz), using a pulse shaping unit with 1 ns time resolution. For excitation bandwidths on the order of the bandwidth of the electronics and the resonator, transient effects play an important role, resulting in systematic distortions of the pulse shape experienced by the electron spins, compared to the ideal pulse shape. These effects can be characterized using a protocol to measure the experimental impulse response of the probe with a pickup coil. Based on the measured impulse response, the transient effects can be taken into account in the optimal control based GRAPE optimization algorithm, resulting in significantly improved experimental performance of broadband pulses. The application of broadband (200 MHz) excitation pulses is presented to a quasi isolated spin 1/2 and an isotropically coupled spin 1/2 system.

Chapter 2

Optimal control methodologies

2.1 Introduction

All experiments in magnetic resonance can be described in a first approach as follows. A sample is held in a strong and uniform longitudinal magnetic field denoted B_0. The magnetization of the sample is then manipulated by a particular sequence of transverse radio-frequency magnetic pulses B_1 in order to prepare the system in a particular state. The analysis of the radio-frequency signal that is subsequently emitted by the nuclear spins leads to information about the structure of the molecule and its spatial position. One deduces from this simple description that the crucial point of this process is the initial preparation of the sample, i.e. to design a corresponding pulse sequence to reach this particular state with maximum efficiency. The maximum achievable efficiency can be determined for a transfer between the initial and target states [1] if relaxation effects can be neglected.

Within the physical conditions of the experiments, the optimal design of the pulses leads to the subject of optimal control theory. Optimal control theory was created in its modern version at the end of the 1950s with the Pontryagin Maximum Principle (PMP) [2–4]. Developed originally for problems in space mechanics, optimal control has become a key tool in a large spectrum of applications including engineering, biology and economics. Solving an optimal control problem leads to the determination of a particular trajectory, that is a solution of an associated Hamiltonian system constructed from the Pontryaguin Maximum Principle and satisfying given boundary conditions. This approach has found remarkable applications in liquid and solid state NMR spectroscopy, as well as in Magnetic Resonance Imaging (MRI) and electron-nuclear system [5].

Roughly speaking, optimal control theory can be divided into purely numerical approachs and geometric methods. In Section 2.2, one numerical approach, the Gradient Ascent Pulse Engineering (GRAPE) algorithm, is briefly discussed. Comparison and the possible coupling between the numerical approach and the geometric methods are presented in Section 2.3.

2.2 Numerical optimization

The gradient ascent algorithm is one of the most important class of numerical optimal control algorithms with the recent progress within NMR spectroscopy [5,6]. It is an iterative approach constructed to solve the optimal equations and the controls are updated in a simultaneous manner, different from the Krotov's method [7] based on a sequential

scheme. The optimization is based on the classical Euler-Lagrange formalism [8]. The goal is to find the curve or trajectory $x(t)$ optimizing the value of the functional

$$\mathcal{J}[x] = \int_{t_0}^{t_1} \mathcal{L}[t, x(t), u(t)]dt + \Phi[x(t_1)], \tag{2.1}$$

which includes a running cost function $\mathcal{L}$, that depends on the path or the trajectories of the spin and a final cost term $\Phi[x(t_1)]$, which is only determined by the final state. $x(t)$ represents the state of the system, while $u(t)$ represents controls to be optimized. For the optimal case, the gradient $\frac{\delta \mathcal{J}}{\delta u}$ at each time point $t_0 \leq t \leq t_1$ should equal to zero. In practice, the gradient can be calculated efficiently based on only one forward propagation of the state $x(t)$ (starting from the given initial state $x(t_0)$) and one back-forward propagation of the Lagrange multipliers, or the adjoint state $\lambda(t)$, starting from the $\lambda(T) = \frac{\delta \mathcal{J}}{\delta x}$. Assuming that the continuous control is digitized in N time slices (with $1 \leq j \leq N$), at each time slice j, there is the state x_j and the corresponding λ_j. Take the most simple system, an uncoupled spin 1/2 as an example. The system can be fully described by the Bloch equation and the gradient is simply the cross product of x_j and λ_j at each time slice:

$$\frac{\delta \mathcal{J}}{\delta u_j} = x_j \times \lambda_j, \tag{2.2}$$

Based on the gradient, a given initial pulse or a random pulse can be improved in an interative fashion by either following the gradient direction directly with a small step size or by using more elaborate methods such as conjugated gradient or quasi Newton methods [9, 10].

Detailed modification of the algorithms according to different applications and spin dynamics are presented in the theory part of each individual chapter.

2.3 Comparison to geometric methods

More geometric aspects of the optimal control can be formulated for quantum systems of low dimensions by using tools of geometric optimal control theory [4]. The idea is to use the methods of differential geometry and Hamiltonian dynamics to solve the optimal control problems. This geometric framework leads to a global analysis of the control problem which completes and guides the numerical computations.

Compared to the pure numerical methods, the geometric method allows a complete geometric understanding of the control problem from which one can deduce the structure of the optimal solution, a proof of global optimality, and the physical limits of a given process such as the minimum time to achieve a complete saturation. Such results can be determined essentially analytically or at least with a very high numerical precision. In addition, once the geometric analysis is done and the optimal control problem solved for one set of parameters, other optimal solutions for other values of parameters can be computed very fast.

However, the geometric method is intrinsically limited to systems of small dimensions. Not like the numerical tools, the geometric approach can not be used to solve complex problems with experimental imperfections and systems with large number of spins. On the other hand, the numerical approach is generally applicable even if a complete geometric analysis is not possible. The relative simplicity of the application of numerical algorithms makes it possible to adapt it straightforwardly to a new class of control problems.

Possible coupling between these two methods could be interesting, like first solving a simplified problem with the geometric techniques and then to use the corresponding control field as a trial field for the numerical algorithm. This allows to help the convergence of the algorithm and to guide it towards a solution similar to the geometric one. Another possibility could be to use a numerical algorithm as a first step allowing to obtain an accurate approximation of the initial adjoint state for the help to solve the shooting equation, which is mandatory in the geometric methods.

Chapter 3

Pulse optimization for single spin 1/2 with relaxation

3.1 Introduction

This chapter is a part of articles [11] and [12], and the work is a collaboration with the research group of Prof. D. Sugny in Dijon, France. In this project, my part was for the numerical optimization and the experimental realization of the optimal pulses, while the geometric analysis is mainly done by our collaboraters in Dijon (same for the projects presented in Chapter 4 and Chapter 6). The work focuses on the optimal control of a spin 1/2 particle with relaxation. As an example, following problem is considered: the saturation of the NMR signal which consists in vanishing the magnetization vector of the sample. The saturation mechanism is interesting in NMR for solvent suppression or contrast enhancement [13, 14]. The optimal control problem is defined by a cost functional which penalizes either the control duration or the energy of the pulse. This problem can be solved both by the Geometric Approach (GM) [3, 4, 15] and by the GRAPE algorithm [6]. In the first case, the Pontryagin Maximum Principle was used to determine the structure of the control field and numerical methods guided by this first analysis to compute the optimal control field. On the other hand, the GRAPE algorithm which is also based on the PMP is a purely numerical approach for solving the optimization equations. In the different computations, a very good agreement is obtained between the geometric and GRAPE results. The relative advantages and disadvantages of the two approaches are discussed. Finally, I implement experimentally the optimal solutions in the energy minimization case by using techniques of NMR.

3.2 Methodology

3.2.1 Model system

The control of the magnetization of a spin 1/2 particle, whose dynamics is governed by the Bloch equation, is considered. Starting from the equilibrium point of the dynamics which corresponds here to the north pole of the Bloch ball, the goal of the control is to reach its center in minimum time (with a maximum bound on the control field) or in fixed time but in minimizing the energy of the field. In this latter case, there is no bound on the control field but the maximum amplitude can be adjusted by changing

the control duration, assuming that the transverse magnetic field is resonant with the frequency of the spin. In this case, it can be shown that the optimal solution can be restricted to a control field in only one direction and that the spin dynamics is confined in a plane [16–20]. With this hypothesis, the Bloch equation is reduced for a control field ω_x along the x- direction to:

$$\begin{pmatrix} \dot{M}_y \\ \dot{M}_z \end{pmatrix} = \begin{pmatrix} -M_y/T_2 \\ (M_0 - M_z)/T_1 \end{pmatrix} + \omega_x \begin{pmatrix} -M_z \\ M_y \end{pmatrix}, \tag{3.1}$$

where M_y and M_z are two components of the magnetization vector $\vec{M}$, M_0 is the value of the equilibrium magnetization and T_1 and T_2 are two characteristic times describing respectively the longitudinal return to the equilibrium and the transverse relaxation of the magnetization. By introducing the normalized coordinates $\vec{X} = \vec{M}/M_0 = (y, z)$, the Bloch equations are rewrited as follows:

$$\dot{\vec{X}} = \vec{F}_0(\vec{X}) + u\vec{F}_1(\vec{X}), \tag{3.2}$$

where $\vec{F}_0 = (-\Gamma y, \gamma(1 - z))$ and $\vec{F}_1 = (-z, y)$. In (3.2), the normalized control is $u = 2\pi\omega_x/\omega_{max}$ and a normalized time which is defined by $\tilde{t} = \omega_{max}t/(2\pi)$ is used. The tilde label of the time t has been omitted in the following of the chapter when confusion is unlikely to occur. The dissipative parameters become $\Gamma = 2\pi/(w_{max}T_2)$ and $\gamma = 2\pi/(w_{max}T_1)$. The parameter ω_{max} denotes for the time-minimum problem the control bound in the original coordinates and is just a characteristic value of the control in the case of the energy minimization problem.

3.2.2 Geometric approach

The optimal control problem can be solved by using the PMP with the constraint of minimizing the duration of the control or its energy. For the time minimum cost, $|u| \leq 2\pi$ is applied, while there is no restriction on the field if the cost minimizes the energy. The PMP is formulated from the pseudo-Hamiltonian H_P [21–24] which can be written as follows:

$$H_P = \vec{P} \cdot (\vec{F}_0(\vec{X}) + u\vec{F}_1(\vec{X})) + p_0 f_0(u(t), \tag{3.3}$$

where $\vec{P} = (p_y, p_z)$ is the adjoint state and p_0 a negative constant such that $\vec{P}$ and p_0 are not simultaneously equal to 0. The cost C is related to the function f_0 via the relation $C = \int_0^T f_0(u(t))dt$, where T is the control duration. In the energy minimization and time-minimum cases, this gives respectively

$$C = \int_0^T u(t)^2 dt = E, \tag{3.4}$$

and

$$C = \int_0^T dt = T, \tag{3.5}$$

E being the energy of the control field. The PMP states that an extremal solution of the problem which is candidate to be optimal is given by the Hamiltonian equations

$$\dot{X} = \frac{\partial H_P}{\partial \vec{P}}, \ \dot{P} = -\frac{\partial H_P}{\partial \vec{X}} \tag{3.6}$$

where the control field is given by the maximization condition

$$H(\vec{X}, \vec{P}) = \max_{u(t)} H_P(\vec{X}, \vec{P}, u). \tag{3.7}$$

Since the way to solve the maximization condition depends on the cost considered, let's first begin the description with the time-minimum problem [15]. In this case, this condition can be written as $\max_{|u(t)|\leq 2\pi}[\vec{P}\cdot u(t)\vec{F}_1]$. Introducing the switching function [21–24] $\phi = \vec{P}\cdot\vec{F}_1 = -p_y z + p_z y$, in the regular case the maximization involves a control of maximum amplitude called bang such that $u = 2\pi \times \text{sign}[\phi(\vec{X},\vec{P})]$ when $\phi(\vec{X},\vec{P}) \neq 0$. If ϕ vanishes in an isolated point, the control field switches from $\pm 2\pi$ to $\mp 2\pi$, while the control is said singular if ϕ is zero in a time interval $[t_0, t_1]$. In this latter case, using the fact that ϕ and its derivative vanish, the singular control u_s can be determined as follows. Denoting $\dot{\phi} = \vec{P}\cdot\vec{V}$ with $\vec{V} = (-\gamma - \delta\gamma z, -\delta\gamma y)$ and $\delta\gamma = \Gamma - \gamma$, the singular set is defined as the set where the vectors $\vec{F}_1$ and $\vec{V}$ are collinear. After few computations, the singular set is the union of the two lines of equation $y = 0$ and $z_0 = -\gamma/(2\delta\gamma)$. To define the control on this singular set, the second derivative of ϕ is computed and $u_s = 0$ on $y = 0$ and $u_s = \frac{\gamma(\gamma-\delta\gamma)}{2\delta\gamma y}$ on $z = z_0$ are found.

For the energy-minimization problem, the Hamiltonian H_P becomes $H_P = \vec{P}\cdot(\vec{F}_0 + u\vec{F}_1) + p_0 u^2$ where the constant p_0 can be normalized to $-1/2$ in the normal case and is equal to 0 in the singular or abnormal one. Since there is no constraint on the control field, the maximization condition leads to

$$\frac{\partial H_P}{\partial u} = 0, \tag{3.8}$$

which gives the following relation in the normal case

$$u = \vec{P}\cdot\vec{F}_1. \tag{3.9}$$

Plugging the expression of u into the Hamiltonian H_P, one obtains the true Hamiltonian $H(\vec{X},\vec{P})$:

$$H = \vec{P}\cdot\vec{F}_0 + \frac{1}{2}(\vec{P}\cdot\vec{F}_1)^2. \tag{3.10}$$

In the normal situation, the extremal solutions of the PMP are the Hamiltonian trajectories of H. In the abnormal case, the maximization condition involves that $\vec{P}\cdot\vec{F}_1 = 0$ and remains equal to zero on a given time interval. This case constitutes the strict analog of the singular situation in the time-minimum control problem. In particular, the singular set and the corresponding singular controls are the same. However, while it can be shown that singular extremals are optimal in the time-minimal case [11], it is shown in [20] that the optimal solution of the saturation problem is regular in the energy minimization problem, the abnormal extremals therefore playing no role.

The last step of this approach is to solve the shooting equation. This means that the initial adjoint state has to be determined $\vec{P}(0) = (p_y(0), p_z(0))$ such that the corresponding projection $\vec{X}(t)$ of the Hamiltonian trajectory $(\vec{X}(t),\vec{P}(t))$ reaches the target state (here the center of the Bloch ball) at time $t = T$. This can be done with a straightforward numerical resolution using Newton methods and the Hamiltonian of Eq. (3.10) for the energy case. For the time-minimum cost, the structure of the control field, i.e. the way the different regular and singular parts of the control are glued together, has first to be determined from a geometric analysis [11, 15]. Since there is no global expression for the Hamiltonian of the system in this case, different shooting equations for each arc of the optimal solution have to be solved.

3.2.3 GRAPE algorithm

This section presents the numerical optimization GRAPE algorithm. Optimal control theory with the GRAPE algorithm has been described in Chapter 2 and in detail else-

where [6, 25–29]. Here the main theoretical aspects are summarized and the necessary modifications associated with time-minimum and energy-minimum cases are introduced. As described above, the spin system in normalized coordinates is consider. The optimal control problem is formulated from the PMP, i.e. via the pseudo-Hamiltonian H_P given by

$$H_P = \vec{P} \cdot (\vec{F}_0 + u\vec{F}_1) + p_0 f_0(u(t)) \tag{3.11}$$

and the cost functions Φ_t and Φ_E for the time and energy cases, respectively. The parameter p_0 and the function f_0 have the same definition as for the GM, but only the regular situation is considered in the algorithm. The performance index Φ can be defined flexibly for different applications. In the current situation, where the target state is the center of the Bloch ball, the cost function can be chosen as

$$\Phi_t = \sqrt{y^2 + z^2}. \tag{3.12}$$

For the energy minimization problem, an additional cost is introduced to minimize the energy of the whole pulse:

$$\Phi_E = \sqrt{y^2 + z^2} + \alpha \int_0^T u(t)^2 dt \tag{3.13}$$

where α is a weight of the penalty imposed to minimize the energy. There is always a compromise between the overlap of the final state to the target state and the energy minimization for the pulse by choosing different values of α. The larger the parameter α is, the worse the overlap but the better the energy minimization is. To guarantee a reasonable overlap of the final state to the target state, a relative small value of α should be used.

The extremal solutions are given by the Hamiltonian equations $\dot{\vec{X}} = \frac{\partial H_P}{\partial \vec{P}}$ for the state and $\dot{\vec{P}} = -\frac{\partial H_P}{\partial \vec{X}}$ for the adjoint state with the parameters $(p_0 = -1, f_0 = 1)$ and $(p_0 = -1/2, f_0 = \alpha u^2(t))$ respectively for the time and energy cases. The optimal control also satisfies the initial condition $\vec{X}(0)$ at the beginning of the pulse, and the final condition $\vec{P}(T) = p_0 \frac{\partial}{\partial \vec{X}}[\sqrt{y^2 + z^2}]$ required at the end of the pulse. The gradients $\partial H_P/\partial u = \vec{P} \cdot \vec{F}_1$ for the time-minimum case and $\partial H_P/\partial u = \vec{P} \cdot \vec{F}_1 - \alpha u(t)$ for the energy minimization problem are computed at each step of the algorithm to indicate how each control field $u(t)$ should be modified in the next iteration to improve the cost function Φ. In this version of the GRAPE algorithm, there is no bound on the control and the control duration is fixed. In the time-minimum case, at each iteration the control field is cut with a maximum amplitude equal to the bound. The computations are done for different control durations. The value of the cost function Φ_t increases as the duration increases but with slower and slower rate (see Fig. 3.1 for an example). Therefore, at a certain control duration, the pulse performance is saturated and the cost Φ_t of this control duration is regarded as the time minimum cost. From a numerical point of view, normally 10-20 control durations are considered to search the area where the duration of the time minimum pulse is located and another 5-10 control durations are used to finalize the computation. To expedite the convergence process, different approaches like the steepest descent method, conjugated gradient method [30] or BFGS method [9, 10, 31, 32] can be adopted.

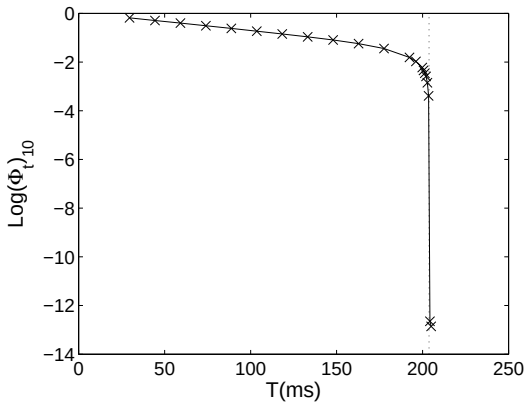

Figure 3.1: Evolution of the cost function Φ_t (crosses) generated by numerical optimization with the GRAPE algorithm as a function of the control duration (see the text for the definition of Φ_t). The solid line is just to guide the eye. Numerical parameters correspond to the first case of Sec. 3.3.1. The vertical dashed line indicates the value of the limit time T for which $\Phi_t \to 0$ (see the text).

3.3 Time minimization case

3.3.1 Numerical results

This section presents the results of the time-minimum problem. The first example used for illustration is defined by the relaxation parameters γ^{-1} and Γ^{-1} (expressed in the normalized time unit defined above) of 23.9 and 1.94, respectively and $M_0 \approx 2.15 \times 10^{-5}$. Note that the value of M_0 is irrelevant for the control problem. The optimal control law with an intuitive one used in NMR are compared. The intuitive solution, the so-called inversion recovery (IR) sequence [13,14], is composed of a bang pulse to reach the opposite point of the initial state along the z- axis followed by a zero control where the dissipation acts up to the center of the Bloch ball. The optimal and the IR solutions are plotted in Fig. 3.2. Geometric tools allow to show that the optimal control is the concatenation of a bang pulse, followed successively by a singular control along the horizontal singular line, another bang pulse and a zero singular control along the vertical singular line. Figure 3.2 displays also the switching curve which has been determined numerically by considering a series of trajectories with $u = +2\pi$ originating from the horizontal singular set where $\phi = 0$. The points of the switching curve correspond to the first point of each trajectory where the switching function vanishes. The second bang pulse of the optimal sequence does not cross the switching curve up to the vertical singular axis. In this example, a gain of 58% is obtained for the optimal solution over the intuitive one, which clearly shows the importance of singular extremals.

Figure 3.3 displays the evolution of the optimal solution and of the intuitive one when the maximum amplitude of the control field varies. The ratio between the two control durations T_{opt} and T_{IR} is also plotted as a function of $\omega_{max}/2\pi$. For low values of ω_{max}, the optimal pulse and the IR sequence are very similar and the ratio is close to 1. Note that for $\omega_{max}/2\pi \leq 2.7$, the target state cannot be reached from the initial point so the ratio cannot be defined. A rapid decrease of this ratio is observed when ω_{max} increases showing the crucial role of the horizontal singular line. The gain tends asymptotically to a constant value when $\omega_{max} \to +\infty$ for fixed values of T_1 and T_2. In this limit, the duration of the different bang controls is neglected. Using the relation $\omega_s = \frac{\omega_{max}}{2\pi} u_s = \frac{T_2 - 2T_1}{2T_1(T_1 - T_2)y}$, one obtains by a direct integration of the Bloch equation

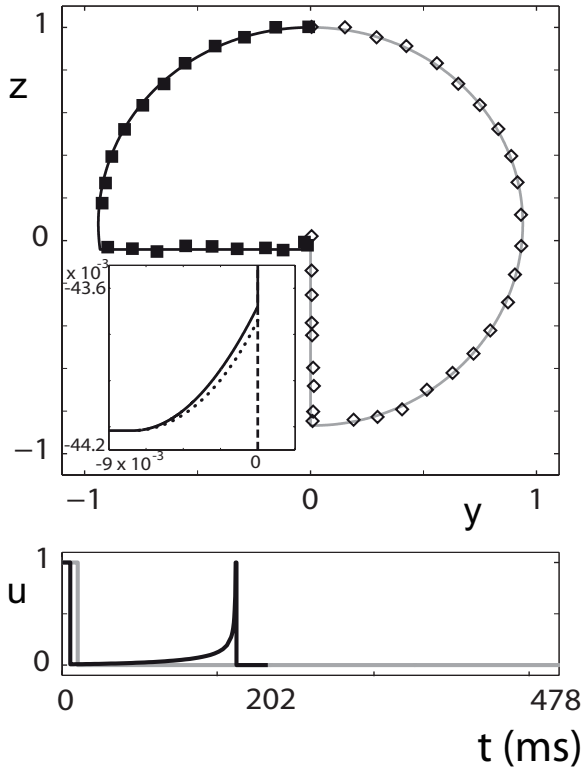

Figure 3.2: Plot of the optimal trajectories (black curve) and of the inversion recovery sequence (grey curve) in the plane (y, z) for $T_1 = 740$ ms, $T_2 = 60$ ms and $\omega_{max}/(2\pi) = 32.3$ Hz. The experimentally measured trajectories are represented by filled squares and open diamonds, respectively. The corresponding control laws are represented in the lower panel. In the upper panel, the small insert represents a zoom of the optimal trajectory near the origin. The dotted line is the switching curve originating from the horizontal singular line. The vertical dashed line corresponds to the intuitive solution. The solid black curve is the optimal trajectory near the origin.

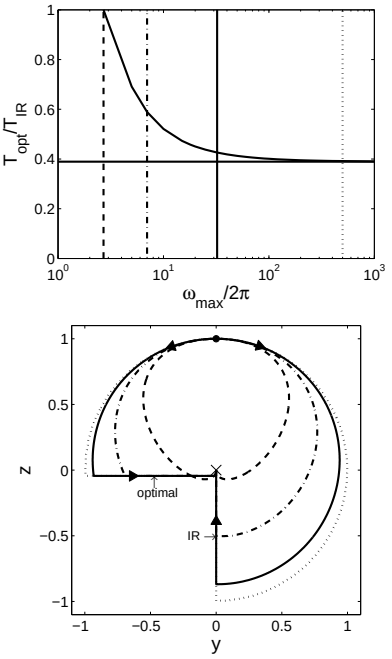

Figure 3.3: (top) Ratio T_{opt}/T_{IR} as a function of $\omega_{max}/(2\pi)$. The horizontal line indicates the position of the limit ratio when $\omega_{max} \to +\infty$. (bottom) Optimal trajectories (left part) and the inversion recovery sequences (right part) for four values of $\omega_{max}/(2\pi)$. The vertical lines of the top panel correspond to the four solutions of the bottom panel. The solid curve is the case considered in Fig. 3.1. The different values of $\omega_{max}/(2\pi)$ are taken to be 2.7, 7, 32.3 and 1000 Hz. The black dot and the cross represent respectively the positions of the initial and final points. The small arrows indicate the way the trajectories are traveled.

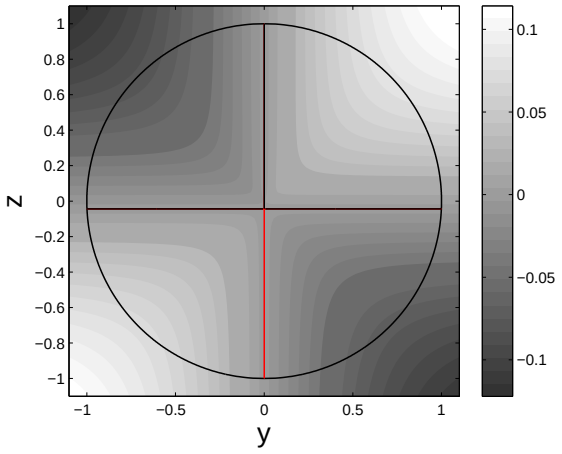

Figure 3.4: Contour plot of the function $d\dot{r}/d\theta$ as a function of y and z. The solid lines represent the set of zeros of $d\dot{r}/d\theta$ or the singular set S (see the text). The time-minimum and time-maximum singular lines are plotted respectively in black and red (light gray).

that

$$T_{opt} \rightarrow_{\omega_{max}\rightarrow+\infty} \frac{T_2}{2}\log(1-\frac{2}{\alpha T_2}) + T_1\log(\frac{2T_1-T_2}{2(T_1-T_2)}),$$
$$T_{IR} \rightarrow_{\omega_{max}\rightarrow+\infty} T_1\log 2,$$

where $\alpha = \frac{T_2(T_2-2T_1)}{2T_1(T_1-T_2)^2}$, which leads to a limit ratio of 0.389.

Physical interpretation of the optimal control strategy. In the example considered, the role of singular extremals can be physically interpreted in light of the dissipation effects. We introduce the polar coordinates (r,θ) such as $y = r\cos\theta$ and $z = r\sin\theta$. A straightforward computation then leads to:

$$\dot{r} = -(\Gamma\cos^2\theta + \gamma\sin^2\theta)r + \gamma\sin\theta,$$
$$d\dot{r}/d\theta = -(\gamma-\Gamma)r\sin(2\theta) + \gamma\cos\theta.$$

One immediately sees that the control field u cannot modify the radial velocity but only the orthoradial one $\dot{\theta}$. To reach in minimum time the center of the Bloch ball, the idea is then at each time to be on the point where $|\dot{r}|$ is maximum for a fixed value of the radial coordinate r. The singular control u_s is determined so that the dynamics stays on the line of maximum variation of the radius r. In other words, this means that the set of solutions of the equation $d\dot{r}/d\theta = 0$ is exactly the set S. One deduces that the strategy of the optimal control can be thought of as follows. A first bang pulse is applied to the system to reach the horizontal singular line. The radius r is then optimally reduced along this curve as long as the control field satisfies the constraint of the control problem. The local optimality of this line can be recovered by showing that the points of this set are associated to maxima of the function $|\dot{r}|(r,\theta)$ for r fixed. When the limit of admissibility is attained, a new bang pulse is applied to reach the vertical singular line in a region where this set is optimal.

3.3.2 Comparison of the analytical and the numerical results

Figure 3.5 displays a comparison between the geometric and the GRAPE solutions for two different sets of dissipative parameters. Very good and similar results have been obtained in the two cases. Unlike the geometric solution, the GRAPE control field is smooth by construction since in the GRAPE method the singular control is not implemented. The GRAPE solution is for instance very close to the horizontal singular set but does not reproduce the second bang pulse. For the first pulse in Fig. 3.5a, the final cost function obtained from the geometric solution is $\Phi_t = 1 - 5.34\times10^{-16}$ while the cost function obtained from the GRAPE optimization is $\underline{1-2.25\times10^{-13}}$. A similar result is found for the second pulse in Fig. 3.5b in which $\Phi_t = 9.88\times10^{-15}$ for the geometric solution and $\underline{1-6.13\times10^{-8}}$ for the GRAPE one.

Using the results of Fig. 3.1, one can have an estimation with the GRAPE algorithm of the control duration as the limit of the time T when $\Phi_t \rightarrow 1$ [33]. One get $T = 6.60$ ($T = 204.3$ ms) which is similar but larger than the value obtained with the GM, $T = 6.58$ ($T = 203.7$ ms).

At this point, some details have to be given about the numerical computations. The geometric results have been obtained by solving the Bloch equation with Runge-Kutta methods (5.10^5 points are used in this propagation), the control field being determined

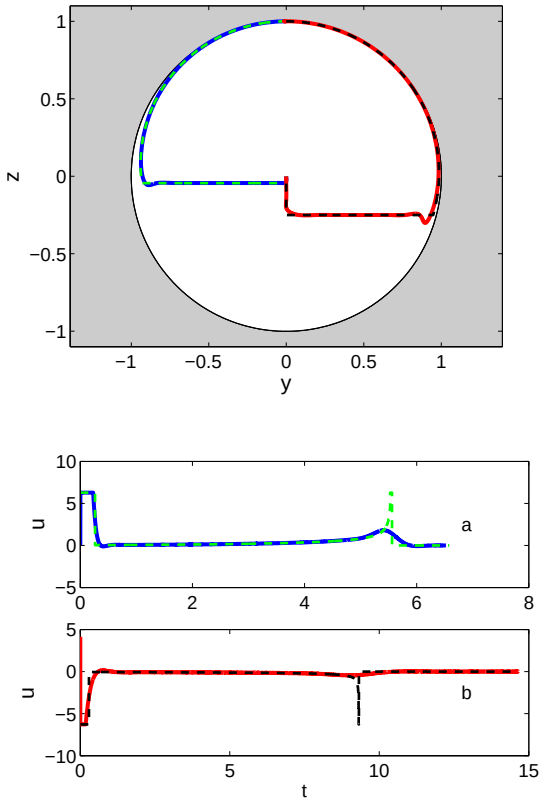

Figure 3.5: (top): Evolution of the magnetization vector in the (y, z)- plane for the numerical (solid line) and the geometrical solutions (dashed line). In the left part of the figure, the green (light gray) and blue (dark gray) trajectories correspond to $T_1 = 740$ ms and $T_2 = 60$ ms, while the red (dark gray) and black trajectories correspond to $T_1 = 740$ ms and $T_2 = 246$ ms in the right part of the figure. The bottom panel displays the corresponding control fields for (a) the left trajectories and (b) the right trajectories.

as a continuous function from the PMP. However, the field implemented experimentally by NMR spectrometers is not continuous but piecewise constant. Therefore one has to discretize the solution over a finite number of points to simulate a realistic NMR experiment. Since the time-optimal solution is a concatenation of different regular and singular arcs whose duration does not have a common divider, a discretization with a constant step size cannot reproduce exactly the continuous optimal sequence leading thus to smaller costs. One get a cost Φ_t equal respectively to $1-1.71\times10^{-3}$ and $1-5.70\times10^{-3}$ in the first and second examples when using 5000 points in the discretization. Note that a better accuracy can be reached with an adaptative step size depending upon the nature of the arc, which requires however some informations about the structure of the control field. The GRAPE algorithm does not encounter such a problem since it optimizes only the discretized values of the control field. From an experimental perspective, the accuracy of the GRAPE solution is therefore better but it depends on the number of points used in the discretization, which is not the case for the geometric control field.

3.3.3 Experimental application

Both the analytical and the IR pulse sequences of Figure 3.2 were implemented experimentally on a Bruker Avance 250MHz spectrometer with linearized amplifiers. The experiments were performed using the proton spins of H_2O. The sample consists of 10% H_2O, 45% D_2O and 45% deuterated Glycerol, saturated with $CuSO_4$. At room temperature (298 K) the relaxation times were $T_1 = 740$ ms, $T_2 = 60$ ms, which correspond to the unitless values given above for $\omega_{max}/(2\pi) = 32.3$ Hz. For this value of ω_{max}, the duration of the intuitive IR sequence is 478 ms, whereas the optimal sequence has a duration of only 202 ms. The experimentally measured trajectories of the Bloch vector are also shown in Fig. 3.2 for the optimal sequence (filled squares) and the IR sequence (open diamonds). The reasonable match between theory and experiment confirms that the complex pulse sequences required for optimization can be implemented with modern NMR spectrometers.

3.4 Energy minimization case

3.4.1 Numerical results

The same work has been done in this section for the energy minimization case. In [20], the singular extremals play no role in this problem, so only regular extremals are considered in the following of the chapter.

The results of the geometric and the GRAPE solutions for the energy minimization problem are also very comparable. Table 3.1 (top) lists the comparison of the two methods for one set of relaxation constants ($T_1 = 740$ ms, $T_2 = 60$ ms) but with different control durations. Three cases are illustrated here, $K = 1.1$, 1.5, and 2, where K is defined as the ratio of the control duration used in the energy minimization (T_E) with that of the time minimization (T_t) in the GM. Note that the energy used by the geometric solution is lower than for the GRAPE one in particular for values of K close to 1. Figure 3.6 displays the optimal trajectories of the magnetization vector and the corresponding control fields for these three durations. In Table 3.1 (bottom), the control fields are optimized for different T_1 and T_2 values and the result are still comparable. In the GM column, the distance to the target with Runge-Kutta methods are indicated.

Next the structure of the control field is analyzed. Figure 3.7 shows that the energy of the control field decreases as the control duration increases, but becomes infinite when

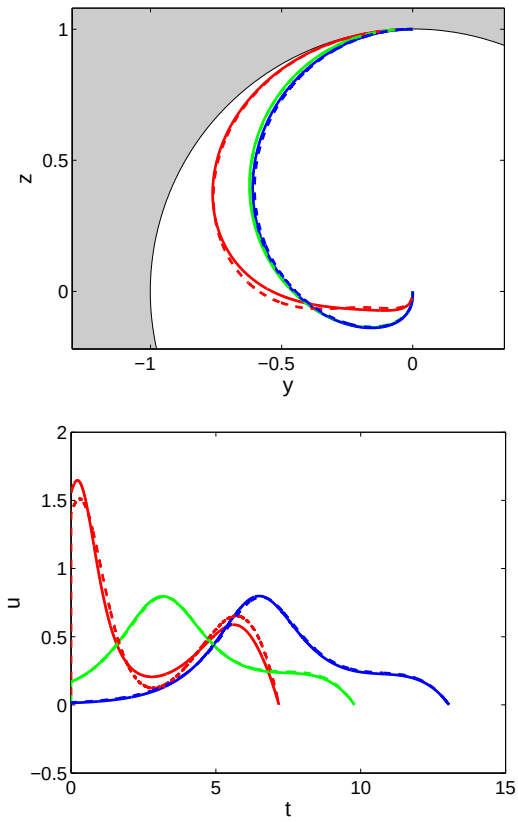

Figure 3.6: (top) Evolution of the magnetization vector in the (y, z)- plane. The solid line corresponds to the geometric solution and the dotted line to the numerical computations with the GRAPE algorithm. Numerical values are taken to be $K = 1.1$ in red (dark gray), $K = 1.5$ in green (light gray) and $K = 2$ in blue (black). The bottom panel represents the corresponding control fields.

T tends to the minimum time of the control [11]. This behavior can be understood from the time-optimal solution. When there is no bound on the control, the control duration is limited intrinsically by the dissipative parameters of the system [11]. The two bang pulses of the optimal sequence have an infinite amplitude but an instantaneous duration and therefore a negligible energy. The singular arc along the vertical singular line has also a zero energy since the corresponding control field is equal to 0. The horizontal singular arc requires however an infinite energy to be followed. This can be shown as follows. The energy E of the singular arc can be expressed as:

$$E = \int_{t_0}^{t_1} \omega_s(t)^2 dt = \int_{-\sqrt{1-z_0^2}}^{0} \omega_s(y)^2 \frac{dy}{\dot{y}}, \tag{3.14}$$

where

$$\omega_s = \frac{\omega_{max}}{2\pi} u_s = \frac{T_2 - 2T_1}{2T_1(T_1 - T_2)y} \tag{3.15}$$

is the singular control in the original coordinates. In Eq. (3.14), t_0 and t_1 are the initial and final times along the arc. In a neighborhood of $y = 0$, $\dot{y} = -\Gamma y - u_s z_0$ is of the order of $-u_s z_0$ since u_s scales as $1/y$. One deduces that the integrand of Eq. (3.14) scales also as $1/y$ and that E has a logarithmic divergence when $y \to 0$. One can conclude that the limit of the energy of the control pulse is infinite in the time-minimum case when the bound of the control goes to infinity.

Figure 3.7 shows that a minimum pulse energy appears when the time increases. This limit is due to the fact that this minimum is reached for a given finite time. For longer durations, the control field has almost the same shape but shifted in time. This behavior is confirmed by the results of Fig. 3.8 where the solid line represents the maximum amplitude of the control field as a function of the control duration. The maximum amplitude tends to a constant value when T increases. The position of this maximum $T(\max(u))$ is represented in the same figure by the dashed-dotted line. It can be checked that $T(\max(u))$ varies linearly with T for T sufficiently large. Finally, note that a compromise between the minimization of the energy and of the control duration can be found as displayed in Fig. 3.7. It can be shown that the product $T \times E(T)$ admits a minimum for a finite time.

Methods	GRAPE	GM	GRAPE	GM	GRAPE	GM
K	1.1		1.5		2	
Energy	3.1876	3.1272	1.8967	1.8963	1.8789	1.8781
Distance	5.37×10^{-12}	1.85×10^{-12}	1.51×10^{-12}	4.99×10^{-13}	3.24×10^{-12}	8.18×10^{-13}
$\delta\gamma$	0.4742		0.2373		0	
Energy	1.8780	1.8798	1.3034	1.3031	0.5879	0.5881
Distance	4.22×10^{-11}	1.34×10^{-14}	1.16×10^{-11}	6.05×10^{-14}	4.75×10^{-11}	3.68×10^{-14}

Table 3.1: (Top) Comparison of the geometrical (GM column) and numerical (GRAPE column) methods for different values of the control duration $K = T_e/T_t = 1.1$, 1.5 and 2. (Bottom) Comparison of the two methods for different values of $\delta\gamma$ with fixed $K = 10$. The parameter $\delta\gamma$ is defined as $2\pi/\omega_{max}(T_1 - T_2)/T_1T_2$. The length $D = \sqrt{y^2 + z^2}$ is the distance to the center of the Bloch ball.

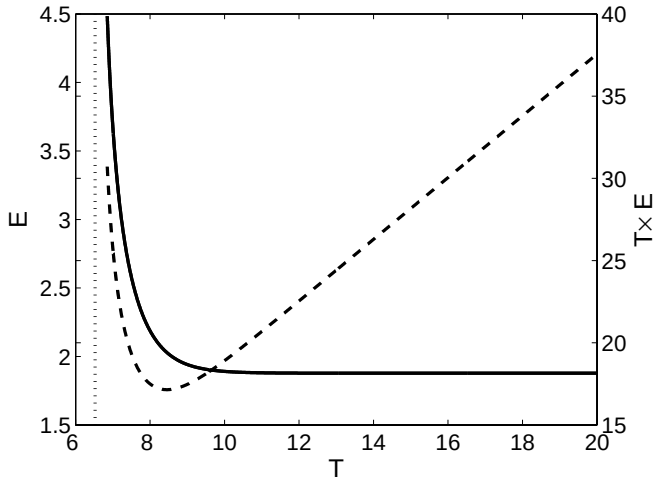

Figure 3.7: (Left vertical axis-solid line) Evolution of the energy of the control field as a function of the control duration. (Right vertical axis-dashed line) Evolution of the product $T \times E(T)$ as a function of T.

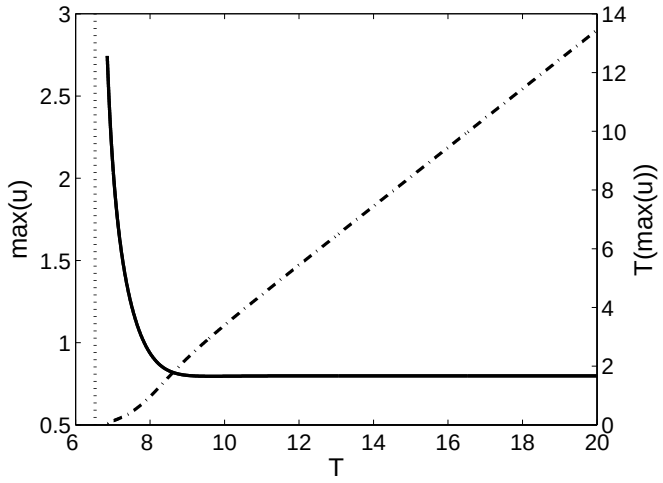

Figure 3.8: (Left vertical axis-solid line) Evolution of the maximum of the absolute value of the control field as a function of the control duration. (Right vertical axis-dashed-dotted line) Evolution of the position of the maximum of the amplitude of the field as a function of the control duration.

3.4.2 Experimental application

This section presents experimental data for $K = 1.1$ in the energy minimization problem where $\omega_{max}/2\pi = 113.8$ Hz. For this case, the optimal pulse with minimum enegy derived using the GM is shown in Fig. 3.7a and was experimentally implemented on a Bruker Avance 600MHz spectrometer with linearized amplifiers. The experiments were performed using the 1H spins of HDO. The sample consisted of 70% D_2O and 30% deuterated glycerol, saturated with $CuSO_4$. At room temperature (298K), the relaxation time constants are $T_1 = 210$ ms, $T_2^* = 17$ ms and $T_2 = 22$ ms (as determined from CPMG-experiment [34, 35]). A simulation shows that very similar trajectories are obtained when using $T_2^* = 17$ ms (with $1/T_2^* = 1/T_2 + \pi\Delta u_{inhomo} = 58.8$, where $\Delta u_{inhomo} \approx 4$ Hz, contributes to the full width at half height of a lorentzian shaped B_0 inhomogeneity distribution) or $T_2 = 17$ ms (assuming negligible B_0 inhomogeneity). The optimal sequence has a duration of 63 ms. In order to determine the experimental y and z components of the trajectory $\vec{X}(t)$, the pulse shape was interrupted at time t. The y- component was then measured directly, while the z- component was isolated by dephasing the transverse magnetization components using a sine shaped magnetic field gradient with a duration of 0.2 ms and measured after bringing it to the transverse plane using a $\pi/2$ pulse. The experimentally measured trajectory of the Bloch vector is shown in Fig. 3.9. The reasonable match between theoretical and experimental curves confirms that such kind of trajectories can be implemented with modern NMR spectrometers. However, due to the experimental accuracy which is of the order of few percents, one sees that the geometric and the GRAPE solutions are equivalent and cannot be clearly distinguished from this experimental result.

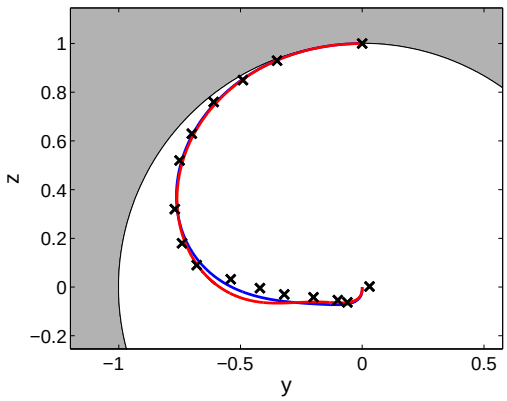

Figure 3.9: Plot of the geometric (blue or dark-gray) and the GRAPE (red or light-gray) optimal trajectories in the energy minimization problem for $K = 1.1$. The experimentally measured points are represented by black crosses.

3.5 Summary

Hoping that these different examples of applications of optimal control theory to spin systems in NMR will motivate a systematic investigation of these aspects in quantum control. As a first example, the optimal control of the saturation of a dissipative spin 1/2 particle is analyzed. In this context, an open question is the generalization of the geometric methods to more complex quantum systems having for instance four or eight

levels or corresponding to two or three spin systems in interaction [36–38]. The complexity of such systems renders difficult the direct resolution of the shooting equation, i.e. the computation of the initial adjoint state. The determination of the optimal control law will require a more extensive numerical analysis than the one presented in this chapter. A possible solution could be the use of a coupling between purely numerical algorithms and GM. Numerical methods such as the GRAPE algorithm could be used as a first step allowing to give an accurate approximation of the initial adjoint state. In each situation, a geometric analysis will be however necessary to understand the role and the optimality of singular extremals.

Chapter 4

Pulse optimization for single spin 1/2 with relaxation and radiation damping effect

4.1 Introduction

This chapter is a part of article [39] (collaboration with the research group of Prof. D. Sugny in Dijon, France). It can be seen as an extended work of Chapter 3, focusing on the time-optimal control of an ensemble of uncoupled spin 1/2 particles in the presence of relaxation and radiation damping effects whose dynamics is governed by non-linear equations generalizing the standard linear Bloch equations.

This chapter is motivated by the desire to systematically use optimal control theory to control the dynamics of spin systems [40]. In chapter 3 both the time-optimal control and the energy minimization problem of a dissipative single spin 1/2 obeying the Bloch equations [11,12] are investigated. Here In this chapter the more general case is analyzed, where radiation damping effects [41–46] are included, resulting in additional non-linear terms in the equation of motion. Radiation damping is a result of the reaction field created by the current induced in the receiver coil. For example in liquid state NMR experiments with large solvent signals or in experiments with hyperpolarized nuclear spins, it is well known that radiation damping effects play an important role.

4.2 Model system

To illustrate our study, considering one of the basic control problems in NMR, that is the saturation problem which consists in vanishing the magnetization vector of a sample in minimum time by using an adequate pulse sequence [11, 13, 14]. Both the cases of a *homogeneous* and of an *inhomogeneous* ensemble of uncoupled spin 1/2 particles with different resonance offsets are analyzed. In the rotating frame, the equation of motion for a homogeneous ensemble irradiated on resonance is given by [41, 45]

$$\begin{pmatrix} \dot{M}_x \\ \dot{M}_y \\ \dot{M}_z \end{pmatrix} = \begin{pmatrix} \omega_y M_z \\ -\omega_x M_z \\ \omega_x M_y - \omega_y M_x \end{pmatrix} + \begin{pmatrix} -M_x/T_2 \\ -M_y/T_2 \\ (M_0 - M_z)/T_1 \end{pmatrix}$$

$$+\frac{1}{M_0 T_r}\begin{pmatrix} -M_x M_z \\ -M_y M_z \\ M_x^2+M_y^2 \end{pmatrix}, \tag{4.1}$$

where the Bloch vector $(M_x,\ M_y,\ M_z)^t$ represents the state of the system. The first term on the right hand side represents the effect of the control amplitudes ω_x and ω_y. The second term corresponds to the longitudinal and transverse relaxation rates T_1^{-1} and T_2^{-1}. The last term is associated to the effect of radiation damping and is non-linear in the components of the Bloch vector. The radiation damping constant T_r depends on the rf coil filling factor and the rf circuit figure of merit [41, 45]. M_0 is the magnitude of the Bloch vector at thermal equilibrium. In the case of an inhomogeneous ensemble with different resonance offsets ω, each isochromat is characterized by a Bloch vector $\mathbf{M}(\omega)$ $=(M_x(\omega),\ M_y(\omega),\ M_z(\omega))^t$. The transverse magnetization components of the isochromats are collectively coupled to the rf coil to produce a unique reaction field, resulting in [46]

$$\begin{pmatrix} \dot{M}_x(\omega) \\ \dot{M}_y(\omega) \\ \dot{M}_z(\omega) \end{pmatrix} = \begin{pmatrix} -\omega M_y(\omega)+\omega_y M_z(\omega) \\ \omega M_x(\omega)-\omega_x M_z(\omega) \\ \omega_x M_y(\omega)-\omega_y M_x(\omega) \end{pmatrix}$$

$$+\begin{pmatrix} -M_x(\omega)/T_2 \\ -M_y(\omega)/T_2 \\ (M_0-M_z(\omega))/T_1 \end{pmatrix}$$

$$+\frac{1}{M_0 T_r}\begin{pmatrix} -\overline{M}_x M_z(\omega) \\ -\overline{M}_y M_z(\omega) \\ \overline{M}_x M_x(\omega)+\overline{M}_y M_y(\omega) \end{pmatrix}. \tag{4.2}$$

The average Bloch vector for the entire inhomogeneous ensemble is denoted:

$$\overline{\mathbf{M}} = (\overline{M}_x, \overline{M}_y, \overline{M}_z)^t = \int_{\omega=-\infty}^{+\infty} g(\omega)\mathbf{M}(\omega)\mathrm{d}\omega \tag{4.3}$$

where $g(\omega)$ is a weighting function specifying the relative weight of the magnetization vectors $\mathbf{M}(\omega)$. In the following, I approximate the experimental weighting function $g(\omega)$ by a simple Lorentzian distribution of the form:

$$g(\omega) = \frac{\Delta\omega_L}{\omega^2+(\Delta\omega_L/2)^2} \tag{4.4}$$

where $\Delta\omega_L$ is the full width at half height of the distribution. The chapter is organized as follows. In Sec. 4.3, the time optimal control of a homogeneous ensemble of dissipative spin 1/2 particles in the presence of radiation damping [c.f. Eq. (4.1)] is established using tools of geometric optimal control theory. In Sec. 4.4, the effect of this control field is simulated for a more realistic inhomogeneous ensemble in the presence of static magnetic field inhomogeneities, resulting in a distribution of offsets ω [c.f. Eq. (4.2)]. In Sec. 4.5, the optimal control problem for the inhomogeneous ensemble is solved numerically using the GRAPE algorithm [47]. The optimal trajectories are implemented experimentally using liquid state NMR techniques. A summary of the results is presented in Sec. 4.6.

4.3 Time optimal control of a homogeneous ensemble

This section briefly summarizes the geometric tools needed to solve the optimal control problem for a homogeneous ensemble of spins. This analysis is based on the application of the Pontryagin Maximum Principle (PMP). The reader is referred to [16–20] for a more complete and mathematical presentation of this problem and to standard textbooks for a review of the PMP [15].

Here considers a homogeneous ensemble irradiated on resonance. Using the symmetry of revolution of the system around the z-axis, it can first be shown that without loss of generality, the problem can be restricted to only one control field. In the following of the chapter, one assumes that $\omega_y = 0$ which implies that the x- coordinate of the magnetization vector is not coupled to the others. Introducing the normalized coordinates $Y = M_y/M_0$ and $Z = M_z/M_0$, the dynamics which takes places in the (Y, Z)- plane is ruled by the following equations:

$$\begin{array}{l} \dot{Y} = -\omega_x Z - Y/T_2 - YZ/T_r \\ \dot{Z} = \omega_x Y + (1-Z)/T_1 + Y^2/T_r \end{array} . \tag{4.5}$$

The goal of the control is to bring the magnetization vector from the north pole of the Bloch ball to its center in minimum time with the constraint $|\omega_x| \leq \omega_{max}$ on the field. The application of the PMP leads to the introduction of the pseudo-Hamiltonian $\mathcal{H}$ defined by

$$\mathcal{H} = P_y \dot{Y} + P_z \dot{Z} \tag{4.6}$$

where (P_y, P_z) are the components of the adjoint state. The PMP states that the optimal trajectories are solutions of the system

$$\begin{array}{l} \dot{Y} = \dfrac{\partial \mathcal{H}}{\partial P_y};\ \dot{Z} = \dfrac{\partial \mathcal{H}}{\partial P_z} \\ \dot{P}_y = -\dfrac{\partial \mathcal{H}}{\partial Y};\ \dot{P}_z = -\dfrac{\partial \mathcal{H}}{\partial Z} \end{array}$$

where the optimal control is determined from the maximization condition $\max_{|\omega_x| \leq \omega_{max}} \mathcal{H}(Y, P_y, Z, P_z, \omega_x)$ and the final Hamiltonian satisfies $\mathcal{H} \geq 0$. The standard way to handle the maximization condition is to introduce the switching function $\Phi = -P_y Z + P_z Y$. It is straightforward to see that in the regular case where Φ is different from 0 or vanishes in an isolated point, the corresponding control field is given by $\omega_x = \omega_{max} \text{sign}[\Phi]$. When Φ vanishes, the field switches from $\pm\omega_{max}$ to $\mp\omega_{max}$. In the singular case where Φ is zero in a time interval, the situation is more involved. In particular, one has $\dot{\Phi} = \ddot{\Phi} = 0$ on this interval. A straightforward computation leads to

$$\dot{\Phi} = P_y \left(\frac{T_2(Z-1) - T_1 Z}{T_2 T_1} - \frac{Z^2}{T_r} \right) + P_Z \left(\frac{1}{T_r} YZ + \frac{T_2 - T_1}{T_1 T_2} Y \right). \tag{4.7}$$

The conditions $\Phi = 0$ and $\dot{\Phi} = 0$ are compatible only on the singular set S which is the union of the two lines of equations $Y = 0$ and $Z = Z_0 = T_2/[2(T_2 - T_1)]$. On the set S, the dynamics is controlled by singular fields $\omega_{x,s}$ which are determined from the condition $\ddot{\Phi} = 0$. One arrives at $\omega_{x,s} = 0$ for the vertical line and

$$\omega_{x,s} = \frac{1}{2T_1} \left(\frac{T_2 - 2T_1}{T_1 - T_2} \right) \frac{1}{Y} - \frac{Y}{T_r} \tag{4.8}$$

for the horizontal one. Note that this singular control depends on the radiation damping parameter T_r, while it is not the case for the two singular lines. The extremal trajectories

constructed from the PMP are finally concatenations of regular and singular arcs. The crucial point is however that not every extremal is optimal and other tools have to be used to get optimality results [16–20]. For the saturation problem of this chapter, it can be shown that the optimal solution is the succession of a regular arc of maximum amplitude to reach the horizontal singular line, followed by a singular arc along this latter line up to the point of coordinates (Y_0, Z_0). At this point, a new regular arc is used to reach the vertical singular line where a zero control brings the dynamics towards the target state. Note that here the radiation damping has only a smooth effect on the optimal solution in the sense that it does not change its structure. A detailed construction of this solution and a proof of its optimality can be found in [11] and [16–20].

The optimal and the Inversion Recovery (IR) solutions [13,14] are plotted in Fig. 4.1 for a set of experimentally relevant parameters. The IR sequence, which is a standard NMR technique to saturate a spin, is composed of a bang pulse to invert the direction of the spin and a zero control along the vertical axis to reach the target state with the relaxation. The control durations are equal to 127.14 ms for the optimal sequence and to 979.22 ms for the IR one. The center of the Bloch ball is reached with an accuracy better than 10^{-15} in this case. The comparison between the optimal and the IR sequences allows to highlight the importance of determining the time-optimal solution in such a spin system.

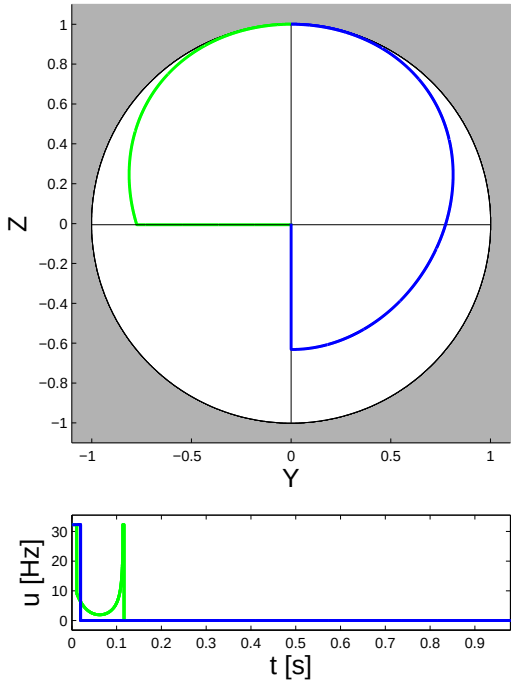

Figure 4.1: Plot of the optimal trajectories (green or gray curve) and of the inversion recovery sequence (blue or dark gray curve) in the plane (Y, Z) for $T_1 = 2000$ ms, $T_2 = 23$ ms, $T_r = 13.7$ ms and $\omega_{max} = 2\pi \times 32.3$ Hz. Numerical computations lead to $Y_0 = -3.3955 \times 10^{-3}$ and $Z_0 = -5.8169 \times 10^{-3}$ for the point where the dynamics leaves the singular line. The corresponding control laws are represented in the lower panel.

4.4 Dynamics of inhomogeneous ensembles

Considering experimental implementations of the optimal trajectories, it is important to distinguish *homogeneous* and *inhomogeneous* ensembles. In the absence of radiation damping, the line width (full width at half height) of a homogeneous ensemble of spins with identical resonance frequencies, is given by $\Delta\omega_{hom} = 2/T_2$ and for an ensemble with a Lorentzian distribution $g(\omega)$ (c.f. Eq. (4.3) and Eq. (4.4)) of resonance frequencies with width $\Delta\omega_L$, the inhomogeneous line width is given by $\Delta\omega_{inh} = \Delta\omega_{hom} + \Delta\omega_L$. This corresponds to an observed time constant $T_2^* = 2/\Delta\omega_{inh}$ for the exponential decay of transverse magnetization in a free induction decay (FID) without radiation damping. Hence, an experimentally determined line width Δ_{exp} is consistent with a wide range of possible values of T_2 and $\Delta\omega_L$. However, the value of T_2 can be independently determined using standard spin echo experiments, in which the effect of different resonance frequencies is refocused [48].

In the presence of radiation damping, the situation is more complicated as radiation damping leads to additional line shape distortions and a non-exponential decay of the FID. We experimentally determined T_2 using a train of 180° refocusing pulses (CPMG sequence) [34, 35], which not only cancels offset terms ω but also radiation damping effects [49]. Assuming a Lorentzian distribution function $g(\omega)$ (c.f. Eq. (4.4)), I determined the width $\Delta\omega_L$ and the radiation damping constant T_r by fitting the experimentally measured trajectories of the average magnetization vector $\overline{\mathbf{M}}$ (c.f. Eq. (4.3)) for different initial points to simulate trajectories using Eq. (4.2). In our simulations, a weighted distribution of the isochromats $\mathbf{M}(\omega)$ was considered and was digitized in $N = 61$ steps for offsets -30 Hz$\leq \omega/(2\pi) \leq 30$ Hz. For each isochromat $\mathbf{M}(\omega_k)$, the evolution was calculated based on Eq. (4.2). Starting at thermal equilibrium, three different initial points were prepared in the different experiments, using a hard pulse with flip angle of 45°, 90°, or 135°. The value of T_1 was measured independently by observing the buildup of longitudinal magnetization after saturation [50]. In order to determine the experimental y and z component of the trajectory $\overline{\mathbf{M}}$, the pulse shape was interrupted at time t. The y component was then measured directly. The z component was measured in a second experiment. It was isolated by dephasing the transverse magnetization components using a sine shaped magnetic field gradient with a duration of 0.2 ms and measured after bringing it to the transverse plane using a $\pi/2$ pulse.

The experiments were performed using a Bruker Avance 600MHz spectrometer with linearized amplifiers and a TXI 5mm probe with z- gradient and the proton spins of H_2O were measured. In order to create conditions, where T_r and T_2 are of comparable magnitude, I prepared a sample consisting of 70% H_2O, 20% deuterated glycerol and 10% D_2O, saturated with $CuSO_4$. A Shigemi tube (with magnetic susceptibility matched for H_2O) with a diameter of 5 mm and a sample height of about 1 mm was used to achieve a relatively homogeneous rf field, allowing us to neglect effects of rf inhomogeneity. At room temperature (298K), the measured time constants were $T_r = 13.7$ ms, $T_2 = 86$ ms and $T_1 = 2$ s. The width $\Delta\omega_L$ of the distribution function $g(\omega)$ was determined to be $\Delta\omega_L = 2\pi \times 10.1$ Hz. This relatively large inhomogeneity of the static magnetic field is a result of the sample geometry and incomplete match of the magnetic susceptibility of the sample tube, and of practical limitations of magnetic field shimming due to the large relaxation rates and the strong radiation damping effect. This inhomogeneity has a significant effect on the experimental trajectories and has to be taken into account in order to achieve a reasonable match between experimental and simulated trajectories.

A naive approach would be to approximate the inhomogeneous ensemble by a homogeneous ensemble with an effective transverse relaxation time $T_2' = T_2^* = 23$ ms, where

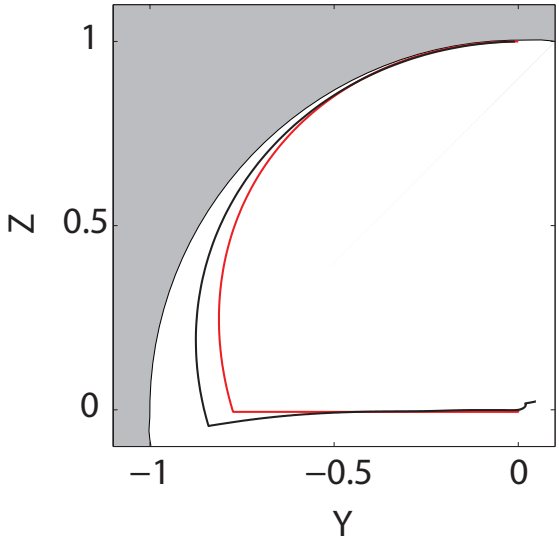

Figure 4.2: Trajectory of the average magnetization vectors for the optimal pulse derived in section 4.3 and applied to a homogeneous ensemble of spin 1/2 (red or grey curve) and an inhomogeneous ensemble (black curve).

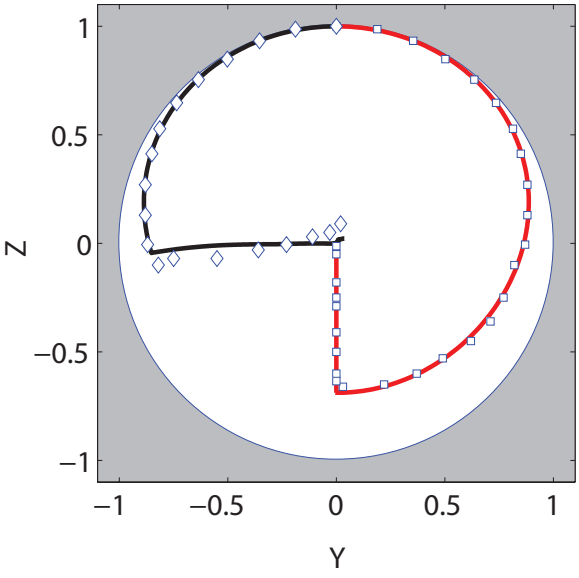

Figure 4.3: Trajectory for the optimal control (black curve) and the conventional inversion recovery (IR) pulse (grey or red curve) for the inhomogeneous ensemble. Experimentally measured trajectories are also shown for the optimal sequence (diamond) and IR sequence (square).

$T_2^{*-1} = T_2^{-1} + \Delta\omega_L/2$. However, this does not provide an accurate representation of the spin dynamics in the presence of pulses and/or radiation damping due to spin-lock effects [48]. This is illustrated in Fig. 4.2, which shows the optimal trajectory derived in Sec. 4.3 for a single spin (corresponding to a homogeneous ensemble) with an effective transverse relaxation time $T_2' = 23$ ms (red or grey curve). The black solid curve shows a realistic simulation for an inhomogeneous ensemble with the experimentally determined parameters given above. The two trajectories are similar but obviously not identical, as expected. In particular, the length of the final magnetization vector of the inhomogeneous ensembles is 4.4% of M_0, i.e. it is not reduced to zero as in the homogeneous case, corresponding to the assumptions of Sec. 4.3.

Fig. 4.3 shows experimental trajectories (diamonds) for the optimized pulse (Fig. 4.1) and for the conventional inversion recovery sequence (squares). A reasonable match is found with the corresponding simulations of the inhomogeneous ensemble shown by black and red/grey curves, respectively. In the next section, I numerically calculate optimal control sequences for the inhomogeneous ensemble using the GRAPE algorithm based on the evolution of isochromats according to Eq. (4.2). This will improve the optimal pulse sequence of Sec. 4.3 in the case of an inhomogeneous ensemble, but at the price of a longer time required for the numerical optimizations.

4.5 Gradient-based optimization for an inhomogeneous ensemble

For a fixed duration T, the GRAPE algorithm [47] can be used to optimize a given figure of merit. Note that similar results could be obtained with other optimization schemes such as the monotonic algorithms [51–56]. For the saturation problem, two possible figures of merit can be defined:

$$\Phi_a = (\overline{M}_x)^2 + (\overline{M}_y)^2 + (\overline{M}_z)^2 \tag{4.9}$$

and

$$\Phi_b = \overline{(M_x)^2 + (M_y)^2 + (M_z)^2}, \tag{4.10}$$

where the bar indicates an ensemble average. Whereas Φ_a only requires the average Bloch vector $\overline{\mathbf{M}}$ to vanish in order to approach its minimum value of 0, the cost function Φ_b only reaches its minimum value of 0 if the Bloch vectors $\mathbf{M}(\omega)$ vanish for all offsets ω with non-zero weight $g(\omega)$ of the inhomogeneous ensemble. Depending on the application, Φ_a or Φ_b, or a combination of both may be most appropriate.
The first order gradient of $\Phi_{a,b}$ with respect to the control amplitudes $\omega_x(t)$ and $\omega_y(t)$ can be expressed as

$$\frac{\delta\Phi_{a,b}}{\delta\omega_x} = -(\overline{M_y(\omega)\lambda_z(\omega) - M_z(\omega)\lambda_y(\omega)}), \tag{4.11}$$

$$\frac{\delta\Phi_{a,b}}{\delta\omega_y} = -(\overline{M_z(\omega)\lambda_x(\omega) - M_x(\omega)\lambda_z(\omega)}). \tag{4.12}$$

For Φ_a, the adjoint state $\boldsymbol{\lambda}(\omega)$ is given at the final time T by $\boldsymbol{\lambda}_f(\omega) = -2\overline{\mathbf{M}}_f$, where $\overline{\mathbf{M}}_f$ is the averaged magnetization at the final time T. For Φ_b, for each isochromat, the adjoint state vector $\boldsymbol{\lambda}(\omega)$ is given at the final time T by $\boldsymbol{\lambda}_f(\omega) = -2\mathbf{M}_f(\omega)$, where $\mathbf{M}_f(\omega)$ is the state of $\mathbf{M}(\omega)$ at the final time T. For $0 \le t < T$, $\boldsymbol{\lambda}(\omega)$ can be determined

by evolving $\boldsymbol{\lambda}_f(\omega)$ backwards in time using the equation of motion

$$\begin{pmatrix} \dot{\lambda}_x(\omega) \\ \dot{\lambda}_y(\omega) \\ \dot{\lambda}_z(\omega) \end{pmatrix} = \begin{pmatrix} -\omega\lambda_y(\omega) + \omega_y\lambda_z(\omega) \\ \omega\lambda_x(\omega) - \omega_x\lambda_z(\omega) \\ \omega_x\lambda_y(\omega) - \omega_y\lambda_x(\omega) \end{pmatrix}$$

$$+ \begin{pmatrix} \lambda_x(\omega)/T_2 \\ \lambda_y(\omega)/T_2 \\ \lambda_z(\omega))/T_1 \end{pmatrix}$$

$$+ \frac{1}{M_0 T_r} \begin{pmatrix} -\overline{M}_x\lambda_z(\omega) \\ -\overline{M}_y\lambda_z(\omega) \\ \overline{M}_x\lambda_x(\omega) + \overline{M}_y\lambda_y(\omega) \end{pmatrix}. \tag{4.13}$$

As in the homogeneous case, the trajectory of the average magnetization vector is in a plane when using one control field. Using the homogeneous solution as a starting point for the optimization in the inhomogeneous case, a modified pulse was found (bottom panel of Fig. 4.4) with $\Phi_a = 0.7\%$. The upper panel shows the trajectories of the average magnetization vector of the inhomogeneous ensemble for this pulse and for the pulse derived in Sec. 4.3, demonstrating a significant improvement compared to the naive application of the homogeneous solution to the inhomogeneous ensemble.

Experimental results are also shown in Fig. 4.4 using the same instrumental setting as detailed in the previous section. Using further optimizations based on the gradient $\frac{\delta\Phi_a}{\delta\omega_x}$ and starting from random pulse sequences, I was able to reduce Φ_a down to 1.7×10^{-9} for the same duration. For the inhomogeneous ensembles, even shorter sequences reach very good saturation levels. For example, for a pulse duration of only 80% of the homogeneous optimized pulse, I found $\Phi_a = 1.1 \times 10^{-8}$. The optimal sequences did not require any control along the y direction. Optimizing Φ_b, this quality factor could be improved from 0.28 for the homogeneous solution to 0.24 for the same pulse duration. It is easier to reach $\Phi_a = 0$ than $\Phi_b = 0$ since in the first case it is not necessary that all the magnetizations are zero. Therefore, for inhomogeneous ensembles, shorter pulse durations for the cost Φ_a are sufficient compared to the homogeneous case.

4.6 Summary

Here I studied the problem of time-optimal control of spins 1/2 in the presence of radiation damping and relaxation, for which the equation of motion is a non-linear extension of the familiar Bloch equations. A homogeneous ensemble of spins can be modeled exactly by a single spin 1/2 particle, for which the control problem was fully analyzed using geometric methods and the important role of singular extremals was pointed out. The minimum pulse duration for the saturation problem was determined and the corresponding optimal pulse was derived. In order to find a reasonable agreement between theoretical and experimental results, an inhomogeneous ensemble had to be modeled using the numerical GRAPE algorithm. Numerical optimization methods were used to find improved saturation pulses in this setting.

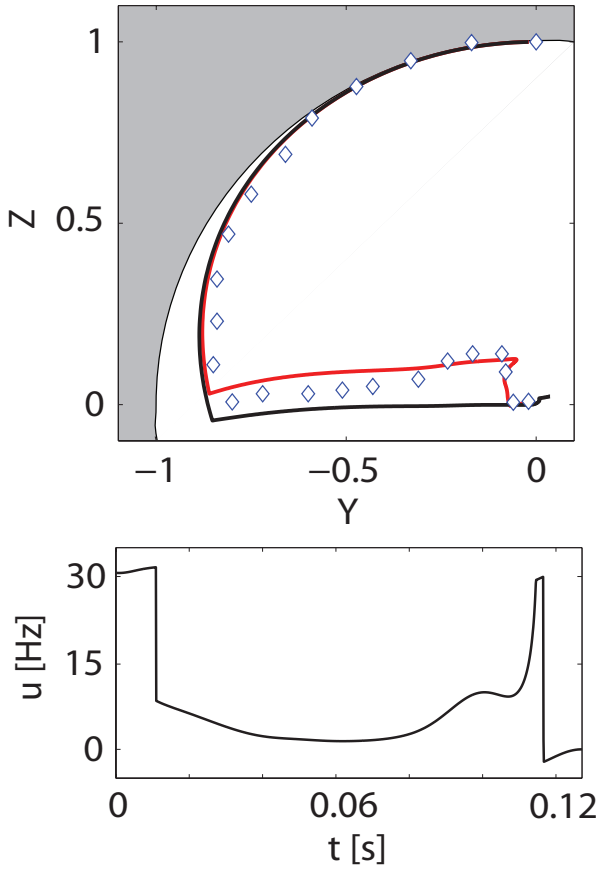

Figure 4.4: (top) Trajectory of the numerically optimized pulse for the inhomogeneous ensemble (grey or red line) and of the analytical solution of section 4.3 (black curve). (bottom) Corresponding pulse sequence from the numerical optimization (black line).

Chapter 5

Excitation of maximum quantum coherence: physical limits and practical pulse sequences

5.1 Introduction

This chapter is a part of article [57], and it focuses on the excitation of maximum quantum coherence (MaxQ) order for a coupled spin system. The simplification and editing of complicated and overlapping spectra is highly desirable in many applications, such as the analysis of complex mixtures or of large biomolecules. To a certain extent, this can be achieved by using two-dimensional NMR spectroscopy, where in addition to the detection period t_2, the frequency of nuclear transitions is also probed in the evolution period t_1 [58, 59]. In two-dimensional multiple quantum NMR experiments, multiple quantum coherence is excited and evolves during t_1 [60,61]. The largest spectral simplification is obtained by exciting and evolving the maximum quantum order that can be created in a given spin system [62–65]. A variety of pulse sequence elements have been developed for the excitation of multiple quantum coherence [58–62]. The standard pulse sequence element based on non-selective pulses has the basic form 90°-Δ-90°, i.e. it consists of two 90° pulses separated by a delay [59]. In practice, an additional 180° pulse is applied in the center of the delay Δ to refocus chemical shift evolution [60]. The delay Δ between the 90° pulses can be optimized based on the theoretical transfer functions if all coupling constants are known or it can be determined experimentally to achieve the best signal-to-noise ratio for a given application.

However, in general the simple 90°-Δ-90° pulse sequence element is not optimal in terms of MaxQ excitation efficiency for a given spin system. In order to generate MaxQ coherence, this sequence requires that there is at least one spin in the spin system that is directly coupled to all other spins. For large spin systems, the size of long-range J coupling constants rapidly decreases with the number of intervening chemical bonds and the smallest coupling constant forms a bottleneck for the speed of multiple-quantum generation, resulting in long inter-pulse durations Δ and concomitant signal loss due to relaxation. Furthermore, the transfer function from polarization to MaxQ coherence is a superposition of oscillating terms and in general the interference of these terms results

in relatively small overall amplitudes of MaxQ coherence. Hence, the excitation of high quantum orders by simple 90°-Δ-90° sequence elements is in general quite inefficient, resulting in a relatively low S/N ratio in the resulting spectra. Significantly improved MaxQ excitation efficiency can be achieved by using more sophisticated sequences adapted to specific coupling topologies [66, 67].

This poses a number of fundamental question that addresses in the following. Ultimately it is interesting of the best possible pulse sequence for a given application for a defined set of potential spin systems. More specifically, here focuses on the following questions:

(a) What is the physical limit of the efficiency with which multiple quantum coherence of a desired order can be created in a given spin system with defined coupling constants and resonance frequencies?

(b) What is the shortest possible time T^* to reach this physical limit for a given spin system?

(c) What is the maximum possible efficiency of multiple quantum generation for shorter times, i.e. if the duration T of the pulse sequence is limited to $T < T^*$?

The answers to questions (a)-(c) provide a benchmark that allows to judge the relative performance of any known or future pulse sequence. Further questions of immediate practical relevance are:

(d) What is the best possible pulse sequence for a given coupling network with defined coupling constants that is robust with respect to variations of resonance frequencies within a desired range?

(e) What is the best performance of relatively simple pulse sequences based on a small number of hard pulses and how large is the achievable gain relative to the simple 90°-Δ-90° pulse sequence element?

Question (a) can be answered based on the general concept of universal bounds of spin dynamics [1, 68–70] and questions (b)-(e) can be addressed using optimal-control based numerical optimization algorithms, such as GRAPE (gradient ascent pulse engineering) [47, 71–73] to optimize MQ excitation sequences. Previously, this algorithm has been successfully used for a large range of NMR applications of uncoupled spins, see e.g. [27, 74]. In coupled spin systems, the GRAPE algorithm was used to optimize the transfer of polarization or single-quantum coherence [47, 75–78] and to create desired unitary transformations [33]. The GRAPE algorithm has also been used for solid state NMR applications to optimize excitation schemes for multiple-quantum magic-angle spinning for quadrupolar nuclei [79]. Although it has been demonstrated that relaxation effects can be fully taken into account in GRAPE optimizations [29, 47, 76, 77, 80, 81], for simplicity here focuses on the excitation of MaxQ coherence in liquid state NMR of small molecules, where relaxation effects can be neglected.

Here methods of pulse design for excitation of maximum-quantum (MaxQ) order are demonstrated, focusing on specific exemplary families of spin systems, which are in part motivated by recent experimental work on mixtures of poly- and monocyclic aromatic hydrocarbons [63]. I discuss the theory and apply it to weakly coupled homonuclear spin systems consisting of up to five spins 1/2. The significantly improved performance of numerically optimized pulse sequences is also demonstrated experimentally.

M	topology	Q_{max}	$T^* \left[J_{max}^{-1}\right]$
2	A	$1/\sqrt{2} = 0.7071$	0.50
3	B	$\sqrt{3/8} = 0.6124$	0.89
	E	$\sqrt{3/8} = 0.6124$	1.49
	F	$\sqrt{3/8} = 0.6124$	0.93
4	C	$1/2 = 0.5$	1.26
5	D	$\sqrt{5/32} = 0.3953$	1.26

Table 5.1: The unitary bound for the maximum quantum excitation efficiency Q_{max} and the numerically determined minimum time T^* to achieve it. M is the number of spins in the coupling network and the coupling topologies labled A-F are represented in Fig. 5.2

5.2 Methodology

The state of a spin system is characterized by the density operator $\rho(t)$ and its equation of motion is given by the Liouville-von Neuman equation [58]:

$$\dot{\rho}(t) = -i[(H_0 + 2\pi(u_x(t)F_x + u_y(t)F_y), \rho(t)], \tag{5.1}$$

where $u_x(t)$ and $u_y(t)$ are the amplitudes of the x and y components of the radio-frequency (rf) field, $F_\alpha = \sum_{k=1}^{M} I_{k\alpha}$ (for $\alpha \in \{x, y, z\}$) and M is the number of spins in the coupling network. The free evolution Hamiltonian

$$H_0 = H_{off} + H_c \tag{5.2}$$

consists of the offsets term

$$H_{off} = \sum_{k=1}^{M} 2\pi\nu_k I_{kz} \tag{5.3}$$

and of the homonuclear coupling Hamiltonian H_c, which is assumed to be isotropic:

$$H_c^{iso} = \sum_{k<n} 2\pi J_{kn}(I_{kx}I_{nx} + I_{ky}I_{ny} + I_{kz}I_{nz}). \tag{5.4}$$

In the weak coupling limit, the coupling term simplifies to

$$H_c^{weak} = \sum_{k<n} 2\pi J_{kn} I_{kz} I_{nz} \tag{5.5}$$

if $|\nu_k - \nu_n| \ll |J_{kn}|$ and in the absence of rf irradiation. However, note that the isotropic coupling term H_c^{iso} can be made fully active by irradiating an isotropic mixing sequences [82, 83]. Therefore, in the following elements of isotropic mixing are also considered, although for simplicity assuming weak coupling conditions during periods without rf irradiation.

The problem of pulse sequence optimization amounts to finding the optimal amplitudes $u_x(t)$ and $u_y(t)$ that steer a given initial density operator $\rho(0)$ in a specified time T to a density operator $\rho(T)$ which has maximum overlap with a desired target operator. Starting at thermal equilibrium, the initial density operator is proportional to

$$\rho(0) = F_z = \sum_k I_{kz} \tag{5.6}$$

and the target state of the density operator is the multiple quantum operator

$$F^+ = \prod_{k=1}^{M} I_k^+ = \prod_{k=1}^{M} (I_{kx} + iI_{ky}) \tag{5.7}$$

of MaxQ order M.

The efficiency of MaxQ generation by a given pulse sequence can be quantified by the quality factor [1]

$$Q = \frac{|\langle F^+ | \rho(T) \rangle|}{||F^+|| \cdot ||\rho(0)||}, \tag{5.8}$$

i.e. by the absolute value of the scalar product between the (normalized) final density operator $\rho(T)$ and the (normalized) target operator F^+, where $||\rho(T)|| = ||\rho(0)||$ if relaxation can be neglected.

The first order gradient of the quality factor Q with respect to the control amplitudes $u_x(t)$ and $u_y(t)$ can be efficiently calculated using the GRAPE algorithm and based on this gradient, a given initial pulse can be optimized in an iterative fashion [47, 72, 73].

Here three different approaches of pulse sequence optimization are considered, corresponding to three classes of pulse sequences (c.f. Fig. 5.1).

Approach I: In the most general approach, arbitrary pulse shapes $u_x(t)$ and $u_y(t)$ are considered that are irradiated during a given duration T (c.f. Fig. 5.1 A). The spins are assumed to have large offset differences (on the order of 100 J_{max}), where J_{max} is the largest coupling constant in the spin system, to be in the weak coupling limit in the absence of rf irradiation and to allow for selective manipulation of the spins. In practice, $u_x(t)$ and $u_y(t)$ are digitized in steps that are small compared to $|\nu_{max}|^{-1}$, where $|\nu_{max}|$ is the largest absolute frequency offset $|\nu_k|$ of the spin system. For example for M=3 spins, with J_{max}=10 Hz, the offsets are $\nu_1 = -1$ kHz, $\nu_2 = 0$ Hz, and $\nu_3 = 1$ kHz and the pulse is digitized in steps of 100 μs. The performance of the resulting pulses forms a benchmark for the achievable efficiency of MaxQ order as a function of the pulse sequence duration T. However, in approach I the pulse sequences are not optimized to be robust with respect to offset, i.e. they are not broadband. (In principle, robustness with respect to offset could be achieved by considering an ensemble of spin systems with a range of offsets for each spin [47], however, this approach is computationally significantly more expensive and was not applied here.)

Approach II: The second approach considered sequences of N_B basic building blocks (c.f. Fig. 5.1 B), where each block consists of (a) a hard pulse of arbitrary flip angle α_k and phase φ_k, (b) a period Δ_k^{weak} of weak coupling evolution and (c) an optional period Δ_k^{iso} of isotropic mixing. In practice, sequences consisting of $N_B = 4$ and N_B =16 blocks were focused and the sequence parameters α_k, φ_k, Δ_k^{weak} and Δ_k^{iso} were optimized for $1 \leq k \leq N_B$. The resulting sequences of basic building blocks can be translated into practical broadband pulse sequences in a straight-forward way by introducing 180° refocusing pulses in the center of the weak coupling evolution periods Δ_k^{weak} and by applying broadband homo-nuclear isotropic mixing sequences such as DIPSI-2 [84] during the periods Δ_k^{iso}.

Approach III: The third approach focused on simple sequences consisting only of N_P pulses with fixed flip angles of 90° separated by periods Δ_k^{weak} of weak coupling evolution (c.f. Fig. 5.1 C). In each optimization, the phases φ_k of the pulses were fixed to either x or y and all possible combinations of these phases were investigated. In this case, the simulation of the quality factor is fast enough and the number of optimization parameters Δ_k^{weak} is small enough to perform an exhaustive grid search to find the global optimum of performance for this simple class of pulse sequences. As in case (II), the

resulting sequences can be made broadband by introducing 180° refocusing pulses in the center of the weak coupling evolution periods Δ_k^{weak}. Note that the basic 90°-Δ-90° sequence shown in Fig. 5.1 D is a special case of the class of pulse sequences considered in approach III (c.f. Fig. 5.1 C) with $N_P = 2$ and phase difference $\varphi_2 - \varphi_1 = \pi/2$ or 0 for excitation of multiple-quantum coherence of odd or even order, respectively [59, 60]. Similarly, the class of pulse sequences shown in Fig. 5.1 C is a special case of the class of pulse sequences used in approach II (c.f. Fig. 5.1 B) if N_P=N_B.

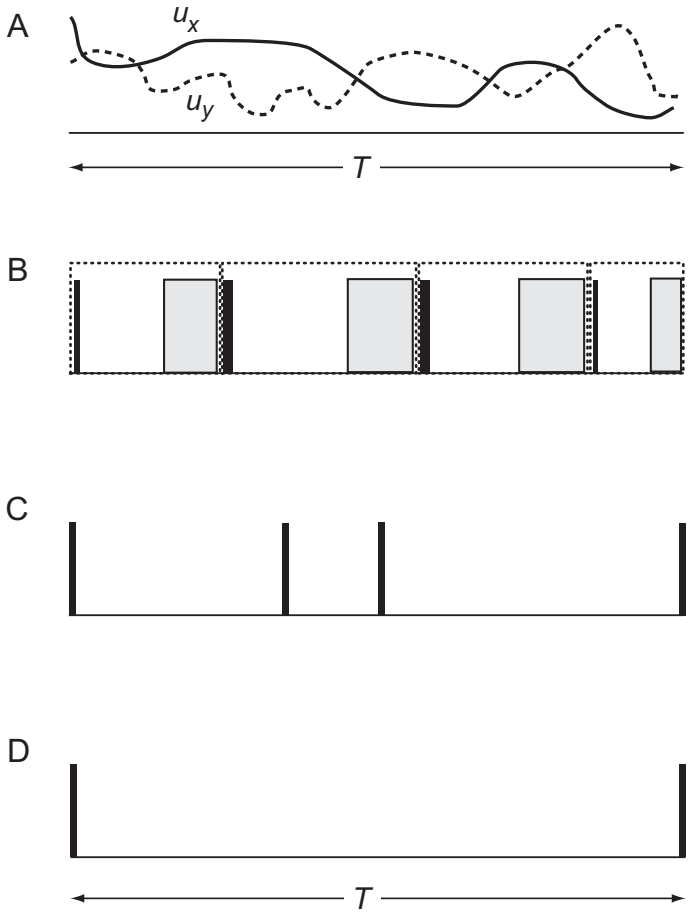

Figure 5.1: Schematic representation of the the families of pulse sequences considered here for excitation of multiple quantum coherence: (A) arbitrary pulse shapes $u_x(t)$ and $u_y(t)$ of duration T that are optimized in *approach I*, (B) sequence of N_B basic building blocks (represented by dotted boxes) that is used in *approach II*, where in the given example the number of blocks N_B is four. Each block consists of a hard pulse of arbitrary flip angle α_k and phase φ_k, a period Δ_k^{weak} of weak coupling evolution and an optional period Δ_k^{iso} of isotropic mixing (represented by a grey box), (C) sequences consisting of N_P pulses with fixed flip angles of 90° separated by periods Δ_k^{weak} of weak coupling evolution, where in the given example $N_P = 4$. The $(N_P - 1)$ delays Δ_k^{weak} are optimized in *approach III*. The phases φ_k of the pulses are fixed to either x or y and all possible combinations of these phases were considered, (D) basic 90°-Δ-90° sequence with phase difference $\varphi_2 - \varphi_1 = \pi/2$ or 0 for excitation of multiple-quantum coherence of odd or even order, respectively [59, 60].

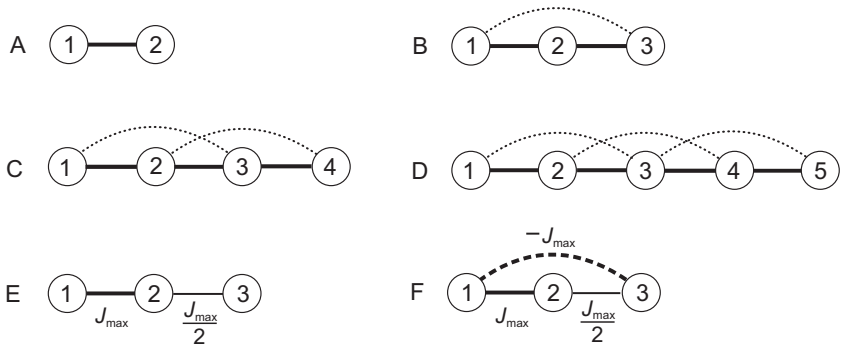

Figure 5.2: Schematic representation of the considered idealized coupling topologies: (A-D) show spin chains consisting of up to five spins 1/2. In addition to the identical next neighbor couplings $J_{k,k+1} = J_{max}$, the case of non-zero second-nearest neighbor couplings $J_{k,k+2}$ were also considered. (E) shows the case of a three-spin chain with unequal coupling constants ($J_{12} = J_{max}$, $J_{23} = J_{max}/2$) and (F) shows the case of a triangular coupling topology with couplings $J_{12} = J_{max}$, $J_{13} = J_{max}/2$ and $J_{23} = -J_{max}$.

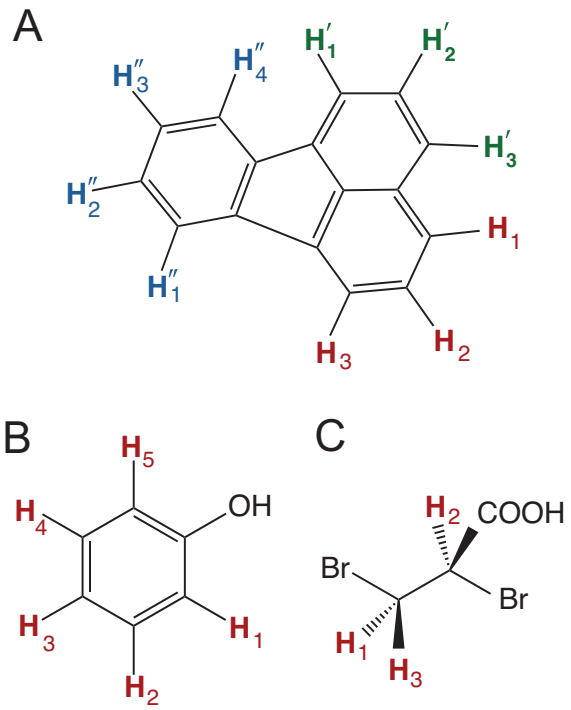

Figure 5.3: Examples of ^{1}H spin systems that are approximately represented by some of the idealized coupling topologies shown in Fig. 5.2 (A) In Fluoranthene, the protons labeled H_1-H_3 (red) and H'_1-H'_3 (green) form two (approximately isolated) three-spin chains (Fig. 5.2 B)and the protons labeled H''_1-H''_4 (blue) form a four-spin chain (Fig. 5.2 C). (B) The proton spin system of Phenol can be approximated by a five-spin chain (Fig. 5.2 D). (C) The proton spin system of 2,3-Dibromopropionic acid with $J_{12} = 11.4$ Hz, $J_{23} = 4.4$ Hz, and $J_{13} = -10.15$ Hz is approximated by the idealized triangular coupling topology of Fig. 5.2 F.

5.3 Results and discussion

The efficiency of MaxQ excitation for the idealized spin system was investigated, shown in Fig. 5.2. Motivated by previous MaxQ experiments on mixtures of mono- and polycyclic aromatic hydrocarbons [63], I studied idealized linear chains of coupled spins with only nearest-neighbor couplings $J_{k,k+1} = J_{max}$ (solid lines in Fig. 5.2 A-D). In order to make the systems more realistic, I also considered linear spin chains with additional second-nearest neighbor couplings $J_{k,k+2}$ (dashed lines in Fig. 5.2 A-D). Fig. 5.3 shows examples of molecules with coupling topologies that are approximated by some of the idealized coupling topologies show in Fig. 5.2. For example, for the ^{1}H spin systems of mono- and polycyclic aromatic hydrocarbons such as Fluoranthene and Phenol (c.f. Fig. 5.3 A and B), typical ^3J couplings between nearest neighbor proton spins are on the order of J_{max} = 7-8 Hz, whereas the ^4J couplings between second-nearest neighbor proton spins are only on the order of 1-2 Hz, resulting in $J_{k,k+2}/J_{max} \approx 0.2$. Long range ^5J couplings are on the order of 0-0.5 Hz and are neglected here. The relative size of the coupling constants of the idealized spin system shown in Fig. 5.2 F with $J_{12} = J_{max}$, $J_{23} = J_{max}/2$ and $J_{13} = -J_{max}$ closely approximate the situation in the ^{1}H spin system of 2,3-Dibromopropionic acid (Fig. 5.3 C)with the experimentally determined coupling constants J_{12} = 11.4 Hz, J_{23} = 4.4 Hz, and $J_{13} = -10.15$. Finally, the coupling network shown in Fig. 5.2 E is identical to the case of Fig. 5.2 F except for $J_{13} = 0$, and forms an example of a linear three-spin chain with unequal nearest neighbor coupling constants ($J_{23} = J_{12}/2$) and vanishing second-nearest neighbor couplings, and it forms an intermediate coupling topology between Fig. 5.2 B and F.

For each coupling topology, I systematically optimized the efficiency of MaxQ excitation as a function of the pulse sequence duration T using approaches (I)-(III) and the results are summarized in Fig. 5.4 and Fig. 5.5. The unitary bound [1, 68–70] for the achievable efficiency of MaxQ excitation (summarized in Table 5.1) is indicated in each panel of Fig. 5.4 by a horizontal dotted line.

The maximum possible MaxQ excitation efficiency as a function of pulse duration can be numerically approximated using approach (I) and its graphical representations (marked by solid circles in Fig. 5.4 A-F) are called TOP (time optimal pulse) curves [75, 85]. The numerical TOP curves provide a benchmark to judge the relative performance of simple pulse sequences based on approach II or III. The shaded areas in Fig. 5.4 represent the "forbidden" regions of the graphs, i.e. all possible experimental MaxQ excitation schemes are bounded by the TOP curve (and the unitary bound). The minimum time required to reach the unitary bound depends on the specific spin system. It can be estimated (within numerical accuracy) by plotting the logarithm of the difference between the unitary bound Q_{max} and the numerically found TOP curve $Q(T)$ as a function of the pulse sequence duration T (c.f. Fig. 5.5). For each coupling topology, the minimum time T^* required to approach the unitary bound with an error of less than 10^{-10} is summarized in Table 5.1 and is shown as a vertical dashed line in Fig. 5.5. For the case of linear spin chains, T^* increases from $0.5/J_{max}$ (for M=2), to $0.89/J_{max}$ (for M=3), to $1.26/J_{max}$ (for M=4). Surprisingly, the same numerical approximation of T^* of $1.26/J_{max}$ is found for M=4 and M=5.

In addition to the unitary bound and the TOP curves, in each panel of Fig. 5.4 the MaxQ excitation efficiency of the basic 90°_y-Δ-90°_ϕ pulse sequence element (with $\phi = y$ if M is odd and $\phi = x$ if M is even [60]) is shown by dash-double-dotted red curves ($-\cdot\cdot$) for comparison (assuming $J_{k,k+2} = 0$ for the spin chains in Fig. 5.4 B-D). The basic two-pulse sequence reaches the unitary bound only for the simple two-spin system (Fig. 5.4 A). For the considered three-spin systems, the basic two-pulse sequence reaches only

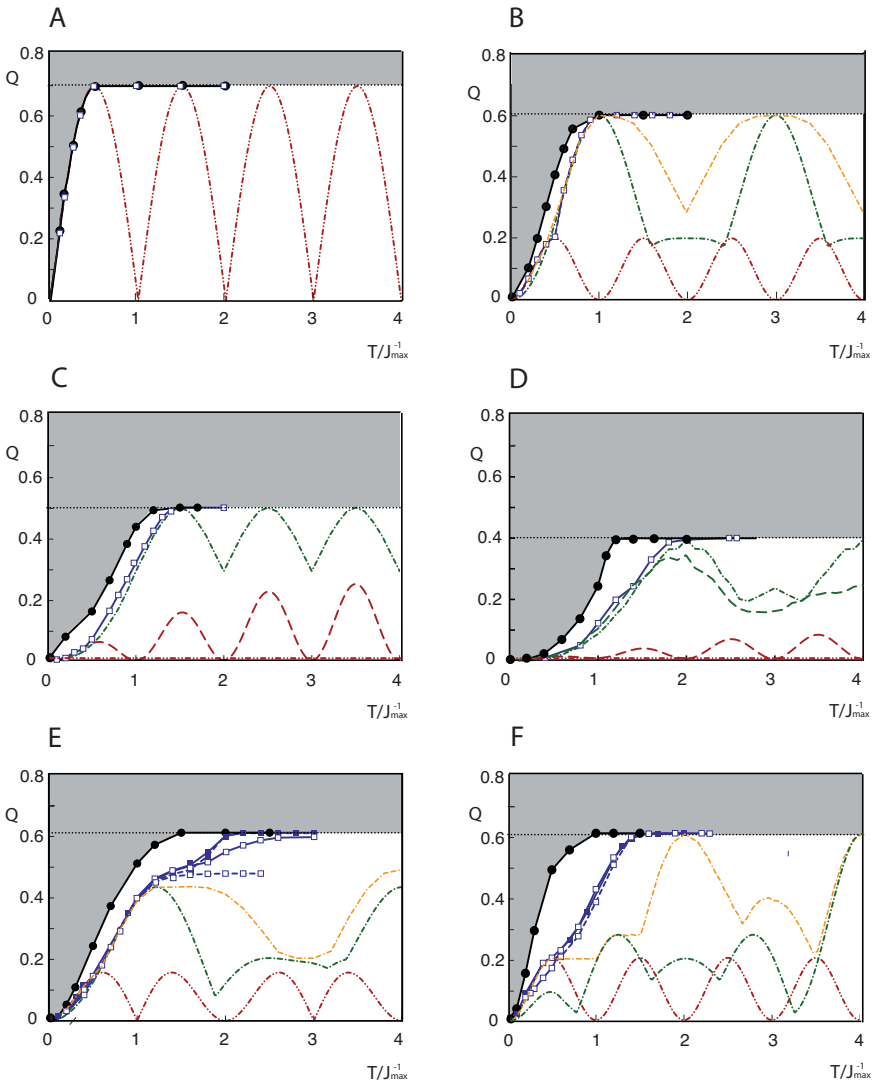

Figure 5.4: Panels A-F show the maximum quantum (MaxQ) excitation efficiency Q (c.f. Eq. 8) for several excitation schemes as a function of pulse sequence duration T for the corresponding idealized coupling topologies of Fig. 5.2 A-F. The unitary bound for the maximum efficiency of MaxQ generation (c.f. Table 5.1) is indicated in each panel by a horizontal dotted line, the maximum achievable efficiency Q for any given pulse sequence duration T is given by the time-optimal pulse (TOP) curve (marked by solid circles), which is found using approach I. The shaded area limited by the TOP curve and the unitary bound represents the "forbidden" regions of the graphs. The achievable transfer efficiency of the conventional building block consisting of two 90° pulses (corresponding to approach III with $N_p = 2$ pulses) is represented by red curves $(- \cdot \cdot)$. For $N_p = M$ and $M + 1$ pulses (where M is the number of spins) the results are represented by green $(-\cdot)$ and orange $(- - \cdot)$ curves, respectively, assuming $J_{k,k+2} = 0$. For the case $J_{k,k+2} = J_{max}/7$, the corresponding transfer functions are represented by dashed curves $(--)$ of the same color. Open and solid squares represent results of block optimizations (approach II) without and with periods Δ_k^{iso} of isotropic mixing, respectively. Squares connected by dashed lines lines correspond to the optimization of $N_B = 4$ blocks, whereas squares connected by solid lines correspond to the optimization of $N_B = 16$ blocks. The pulse sequence duration T is given relative to the inverse of the largest coupling constant J_{max} in each spin system.

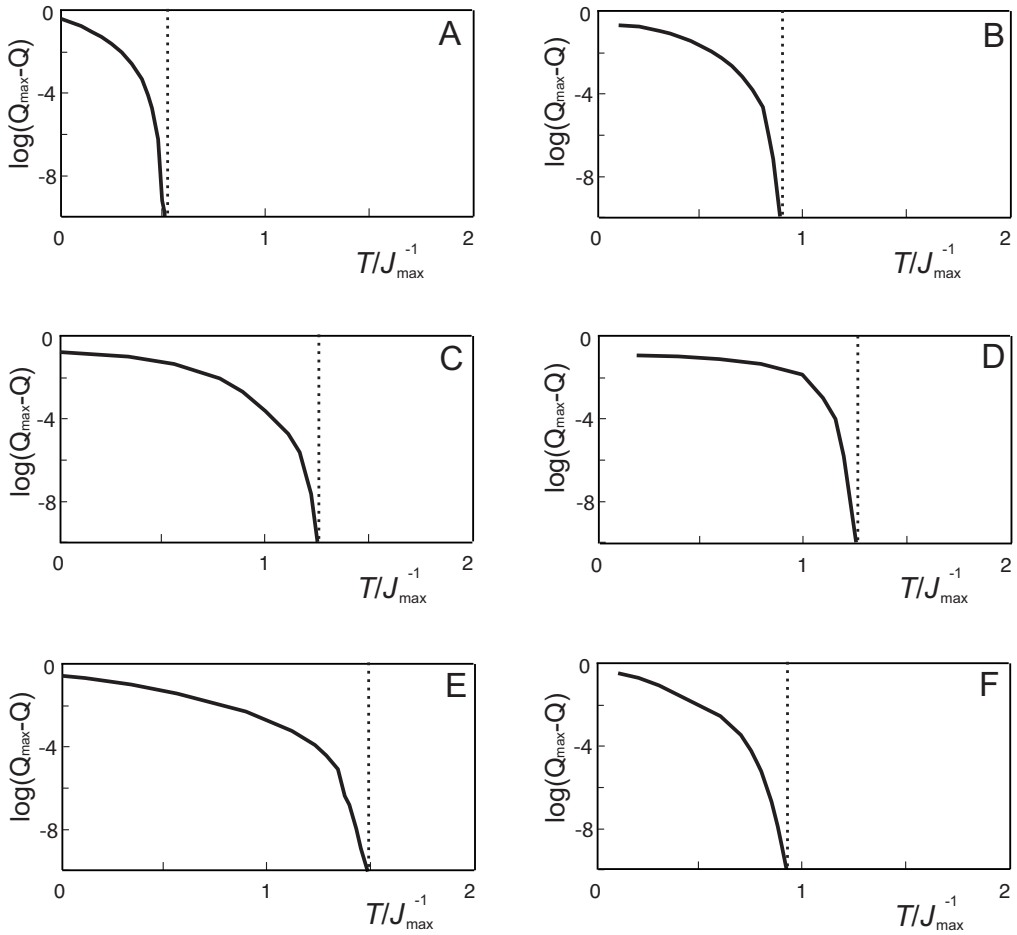

Figure 5.5: Panels A-F show the logarithm of the difference between the unitary bound Q_{max} and the numerically found TOP curve $Q(T)$ (c.f. Fig. 5.4)as a function of the pulse sequence duration T. The vertical dashed line represents the minimal time T^* that is required to approach the unitary bound with a an error of less than 10^{-10}.

about 30% of the unitary bound (Fig. 5.4 B, E, F). No MaxQ coherence can be created by the simple two-pulse sequence for spin chains consisting of four and five spins (Fig. 5.4 C and D) if only nearest neighbor couplings are non-zero ($J_{k,k+2} = 0$). This is expected as in this case there exists no spin that is coupled to all remaining spins in the coupling network (see Fig. 5.2 C, D). Only for the case of non-vanishing second-nearest neighbor coupling ($J_{k,k+2} > 0$), MaxQ coherence is created by the simple two-pulse sequence, see dashed red curves $(--)$ in Fig. 5.4 C and D. Even in this case, the transfer efficiency of the two-pulse sequence is small compared to the unitary bound and the buildup of MaxQ coherence is slow. The low transfer efficiency is explained by the fact that only a fraction of the spins are coupled to all other spins of the chain. For example, in the five-spin chain (Fig. 5.4 D), only the center spin (I_3) is coupled to all remaining spins of the chain, i.e. the initial polarization of spins I_1, I_2, I_4 and I_5 cannot be converted to MaxQ coherence, resulting in a low overall transfer efficiency of the simple two-pulse sequence compared to the unitary bound for the transfer between F_z and F^+. The slow buildup of MaxQ coherence is a result of the bottleneck formed by the relatively small second-nearest neighbor couplings $J_{13} = J_{35} \approx J_{max}/7$ as for the basic two-pulse experiment the transfer function is proportional to $\sin(\pi J_{13}T)\ \sin(\pi J_{23}T)\ \sin(\pi J_{34}T)\ \sin(\pi J_{35}T)$ in the five-spin chain.

Significantly larger and faster excitation of MaxQ coherence can be achieved using more than two 90 degree pulses (approach III). In Fig. 5.4, the green dashed dotted curves $(-\cdot)$ represent the achievable transfer efficiency based on approach III for the case of $N_p = M$, where M is the number of spins, assuming $J_{k,k+2} = 0$ for the spin chains in Fig. 5.4 A-D. Obviously approach III with $N_p = M$ is identical to the case of the conventional two-pulse sequence for the system consisting of $M = 2$ spins (Fig. 5.2 A). All possible combinations of pulse phases x or y were simulated and only the curves for the best combinations are presented in Fig. 5.4. For the spin chains (Fig. 5.4 A-D), approach III yields simple and quite efficient pulse sequences for $N_p = M$ pulses. The necessary time to reach the unitary bound is about 1.12 T^* for M=3 spins, 1.19 T^* for M=4 and 1.59 T^* for M=5 spins

While for the case of linear chains (or symmetric coupling topologies) with equal coupling constants it is possible to derive sequences with reasonable transfer efficiencies by hand using the well-known rules of the product operator formalism [66, 67], finding optimal pulse sequence in the case of unequal couplings or complex coupling networks is a non-trivial task. The effect of including second-nearest neighbor couplings is shown in Fig. 5.4 D for $N_p = M = 5$. In contrast to the case of the two-pulse sequence, the dashed green line (for the case $J_{k,k+2} = J_{max}/7$) and the dash-dotted green line (for the case $J_{k,k+2} = 0$) are quite similar because the sequence exploits the large nearest neighbor couplings and does not critically rely on the smaller $J_{k,k+2}$ coupling. In fact, for $T < 1.6/J_{max}$, the optimized five-pulse sequence is able to exploit the small $J_{k,k+2}$ couplings to yield a slightly larger transfer amplitude, whereas for longer pulse durations the additional small $J_{k,k+2}$ couplings result in slightly smaller transfer amplitudes. For the three-spin systems of Fig. 5.2 E with unequal couplings, the largest transfer amplitude of the sequence consisting of $N_p = M = 3$ 90° pulses is only about 70% of the unitary bound (c.f. Fig. 5.4 E). For the three-spin systems of Fig. 5.2, the unitary bound is reached but only for a relatively long pulse duration of 4 $/J$, corresponding to more than three times the duration of T^* (c.f. Fig. 5.4 F), whereas for $T < 3.6/J$ the maximum achievable transfer amplitude is less than half of the unitary bound. Increasing the number of 90° pulses from $N_p = M = 3$ to $N_p = M + 1 = 4$ (orange double-dash-dotted curves $--\cdot$) only slightly improves the achievable transfer efficiency in Fig. 5.4 E. However in Fig. 5.4 F it reduces the pulse duration to achieve

the unitary bound by 50% to only about 1.6 T^*. In the three-spin system of Fig. 5.4 B, the use of four 90° pulses only improves the transfer efficiency compared to sequences consisting of two or three 90° pulses for pulse sequence durations that are longer than the time $T = 1/J_{max}$ to reach the unitary bound.

Finally, Fig. 5.4 also shows the results of block optimizations using approach II. Open and solid squares represent results of block optimizations without and with periods Δ_k^{iso} of isotropic mixing, respectively. Squares connected by dashed lines lines correspond to the optimization of $N_B = 4$ blocks, whereas squares connected by solid lines correspond to the optimization of $N_B = 16$ blocks. In spin chains, the ability to use isotropic mixing periods does not lead to improved pulse sequence performance and no (Fig. 5.4 A, B) or relatively small (Fig. 5.4 C, D) gains are found compared to approach III. However, in Fig. 5.4 E and F, significantly improved performance is found using approach II compared to approach III. Compared to the performance of 4 blocks, 16 blocks yield slightly larger quality factors Q but in the triangular coupling topology of Fig. 5.4 F, the ability to used periods of isotropic mixing did not lead to improved efficiency of MaxQ coherence. However, the linear coupling topology with unequal couplings (Fig. 5.2 E) is an example of a spin system, where the use of isotropic mixing periods is in fact beneficial (see Fig. 5.4 E). Here, even with only four blocks, approach II with isotropic mixing periods yields pulse sequences that closely approach the unitary bound near $T = 2/J_{max}$, which is only about 60% longer than T^*, whereas for the same time the four-block sequences without isotropic mixing reaches only about 80% of the bound.

Fig. 5.6 compares the maximum quantum (MaxQ) excitation efficiency Q (c.f. Eq. 5.8) for the linear spin chain of 5 spins (c.f. Fig. 5.2 D) for the cases with and without the second-nearest neighbor coupling $J_{i,i+2}$, as a function of pulse sequence duration T. Panel A summarizes cases without weak second-nearest neighbor coupling ($J_{i,i+2} = 0$) for the delay optimization (approach III) with $N_p = N - 3 = 2$ (the red curve), $N_p = N-2 = 3$ (the blue curve), $N_p = N-1 = 4$ (the black curve) and $N_p = N = 5$ (the green curve), respectively. One can see that, without the second-nearest neighbor coupling $J_{i,i+2}$, the two 90° pulses (the red curve) generate no MaxQ coherence at all, while the efficiency of $N_p = 3$ and $N_p = 4$ is also low with the maximum transfer of less than 10%. Panel B displays the simulation results for the sequence with $N_P = N$ (same as the green curve of panel A) but with the weak second-nearest neighbor coupling $J_{i,i+2} \neq 0$. The green dash-dotted curve shows the original simulation of $J_{i,i+2} = 0$ as a reference. The solid curves with different colours correspond to simulations for different values of $J_{i,i+2} = J_{i,i+1}/28, J_{i,i+1}/14, J_{i,i+1}/7$, respectively. As expected, with the increased value of $J_{i,i+2}$, the performance of the pulse (the Q factor) decrease gradually since the original pulses are optimized for the case without $J_{i,i+2}$.

Note that the current work is focused on the MaxQ transfer case, however the presented approach can also be applied to the efficient generation of multiple quantum coherence of arbitrary order.

5.4 Experimental application

For an experimental demonstration of optimized MaxQ excitation sequences, I chose the ^{1}H spin system of 2,3-Dibromopropionic acid (c.f. Fig. 5.3 C) dissolved in $CDCl_3$. The experiments were performed at room temperature using a Bruker Avance 600 MHz spectrometer. The experimentally determined coupling constants are $J_{12} = 11.4$ Hz, $J_{23} = 4.4$ Hz, and $J_{13} = -10.15$ Hz. A Shigemi tube (magnetic susceptibility matched for $CDCl_3$) with a diameter of 5 mm was used to achieve a rf field with high homogeneity.

In the experiments, spin 1 was set on resonance ($\nu_1 = 0$), and the offsets for spins 2

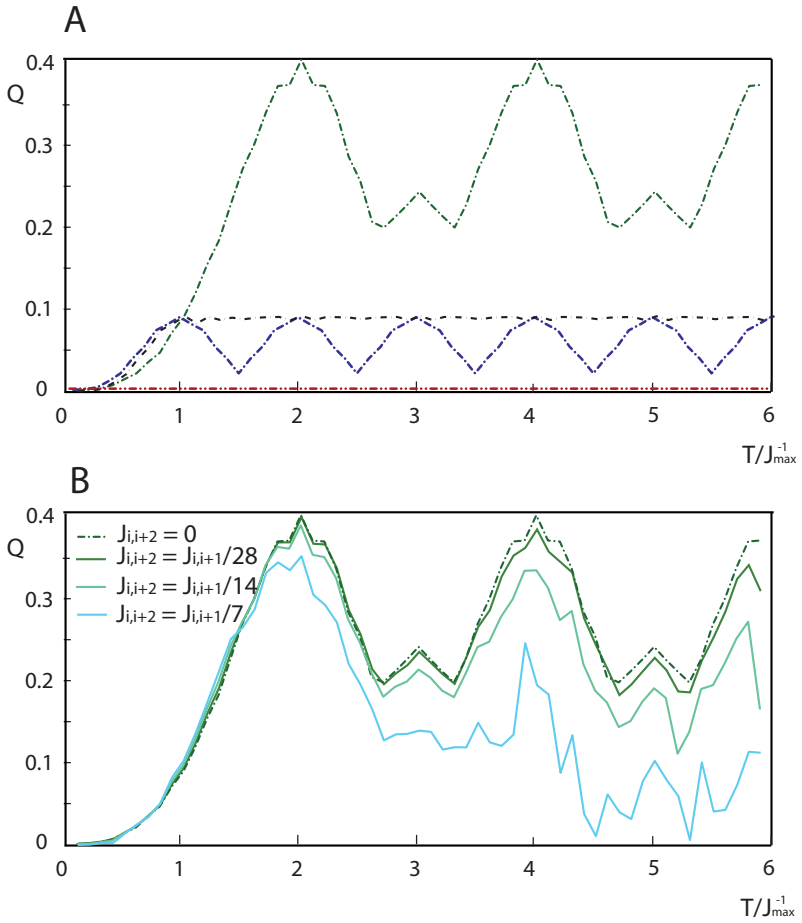

Figure 5.6: The Maximum quantum (MaxQ) excitation efficiency Q (c.f. Eq. 5.8) for the linear spin chain of 5 spins (c.f. Fig. 5.2 D) for the cases with and without the second-nearest neighbor coupling $J_{i,i+2}$, as a function of pulse sequence duration T. Panel A summarizes case without weak second-nearest neighbor coupling ($J_{i,i+2} = 0$) for the delay optimization (approach III) with $N_p = N - 3 = 2$ (the red curve), $N_p = N - 2 = 3$ (the blue curve), $N_p = N - 1 = 4$ (the black curve) and $N_p = N = 5$ (the green curve), respectively. Panel B displays the simulation results for the sequence with the number of 90° pulses of $N_P = N$ with different weak second-nearest neighbor coupling constants, $J_{i,i+2} = J_{i,i+1}/28, J_{i,i+1}/14, J_{i,i+1}/7$, respectively.

and 3 were 347 Hz and −130 Hz, respectively. After the excitation of MaxQ coherence of coherence order 3, other coherences were eliminated using a six-step phase cycling procedure. In all experiments, the same sequence was used to convert MaxQ coherence to detectable single quantum coherence.

Fig. 5.7 shows the experimental excitation efficiencies and the corresponding theoretical curves. Although the experimental relative coupling constants are similar to the ideal case shown in Fig. 5.2 F and Fig. 5.4 F, I recalculated the TOP curve (using approach I) and the maximum excitation efficiency for approaches (II) and (III) for the actual experimental coupling constants. A reasonable match is found between simulations and experiments. The minimum time to reach the unitary bound of MaxQ excitation for the block optimization (approach II) is about 0.14 s.

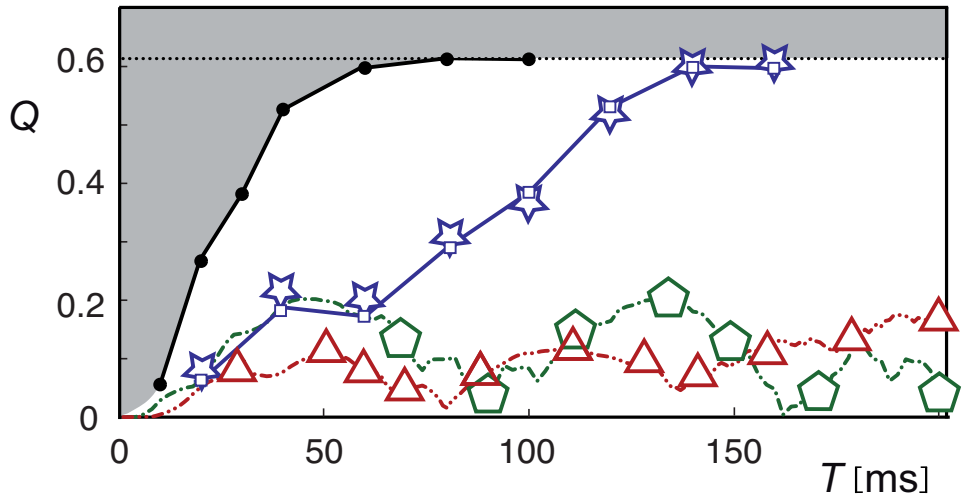

Figure 5.7: Experimental and theoretical MaxQ excitation efficiencies Q of conventional and optimized pulse sequences for the ^{1}H spin system of 2,3-Dibromopropionic acid (Fig. 5.3) with $J_{12} = 11.4$ Hz, $J_{23} = 4.4$ Hz, and $J_{13} = -10.15$ Hz for pulse sequence durations $0 \leq T \leq 200$ ms$= 2.28/J_{max}$. Red triangles and dash-double-dotted curves represent experimental and simulated Q values for the simple standard sequence consisting of two 90° pulses, respectively. Green pentagons and dash-dotted curves ($-\cdot$) show the experimental and theoretical performance of optimized pulse sequences using approach III consisting of three 90° pulses separated by optimal delays. Blue stars and open squares (which are connected by straight lines to guide the eye) represent experimental and simulated results of N_B=4 blocks (approach II without periods of isotropic mixing).

Chapter 6

Exploring the physical limits of saturation contrast in magnetic resonance imaging

6.1 Introduction

This chapter is a part of article [86] (collaboration with the research group of Prof. D. Sugny in Dijon, France) and it focuses on exploring the physical limits of the maximum achievable experimental contrast using optimal control theory. In imaging applications, where relaxation forms the basis for contrast, a very large number of different strategies have been proposed and implemented so far with the rapid improvement of NMR and MRI technology [87, 88]. However, there was no general approach to provide the maximum possible performance and the majority of these pulse sequences have been built on the basis of intuitive and qualitative reasonings or on inversion methods such as the Shinnar-Le Roux algorithm [89]. Note that this latter can be applied only in the case where there is no relaxation effect and radio-frequency inhomogeneity.

Despite the efficiency of MRI techniques currently used in clinics, some aspects still pose fundamental problems of both theoretical and practical interest. The enhancement of contrast remains one of the crucial questions for improving image quality and the corresponding medical diagnosis. The use of particular pulse sequences to generate image contrast based on relaxation rates is not new in MRI, since this question was raised at the beginning of the development of MRI in the 1970s. Different strategies have been proposed, such as the Inversion Recovery sequence [13,90] for T_1 contrast and pulses for ultra short echo time experiments for T_2 contrast [91] (see Eq. (6.1) for the definition of T_1 and T_2 parameters). Here, let's go beyond such intuitive methods by using the powerful machinery of optimal control, which provides in this case not just an improved performance but the global optimum, i.e. the best possible contrast within the experimental constraints. This optimized contrast is demonstrated in a laboratory benchmark experiment.

6.2 Methodology

6.2.1 Model system

In its simplest form, the contrast problem can be stated by assuming that the signal is composed of two different contributions. One considers as a benchmark example the case of (a) oxygenated vs. (b) deoxygenated blood, where the spins that are probed are the ones of the hydrogen atoms of water (H_2O). This is e.g. an important issue in functional studies of the human brain. These spins have different relaxation rates due to the interaction with other molecules such as hemoglobin in its oxygenated or non-oxygenated form, leading thus to two different signatures of the relaxation dynamics of the magnetization, which is governed by the Bloch equations:

$$\left\{ \begin{array}{lcl} \frac{dM_x^i}{dt} & = & -\omega M_y^i + \omega_y M_z^i - M_x^i/T_2^i \\ \frac{dM_y^i}{dt} & = & \omega M_x^i - \omega_x M_z^i - M_y^i/T_2^i \\ \frac{dM_z^i}{dt} & = & -\omega_y M_x^i + \omega_x M_y^i - (M_z^i - M_0)/T_1^i, \end{array} \right. \tag{6.1}$$

where $\vec{M}^i = (M_x^i, M_y^i, M_z^i)$ is the magnetization vector considered with $i = (a, b)$, M_0 is the equilibrium magnetization, T_1^i and T_2^i the longitudinal and transverse relaxation rates, ω the resonance offset and ω_x and ω_y the components in a rotating frame of the transverse magnetic field along the x- and y- directions. While different definitions of contrast exist in the literature [88], here a particular case is considered that it is called the *saturation contrast*, where the objective of the control problem is to find the pulse sequence which completely suppresses the contribution of one of the two magnetization vectors while maximizing the modulus of the other. If such a pulse module can be found, it can be used in combination with a large number of possible host sequences for imaging and spectroscopy (see Chapter 14 of Ref. [88] for details).

6.2.2 Geometric approach

In this section, first the ideal situation of a homogeneous ensemble of spin 1/2 particles irradiated on resonance is analyzed. It is described by Eq. (6.1) with $\omega = 0$. The normalized vectors $\vec{V}^i = \vec{M}^i/M_0$ with coordinates (X^i, Y^i, Z^i) are introduced to eliminate the equilibrium magnetization M_0. Due to the symmetry of revolution of the system around the z- axis (see [17,92] for details), One can restrict the dynamics to a meridian plane by assuming, e.g. $\omega_y = 0$. Using advanced techniques of geometric optimal control theory [11], it is possible to find the desired control field $\omega_x(t)$ which provides the global contrast optimum by a direct solution of the PMP. The details of the theoretical approach are given as following:

Here some indications are given about the optimal control theory used to solve the contrast problem. Labeling the two spins by the indices a and b, recalling that the objective of the control is to determine a field $\vec{\omega} = (\omega_x, \omega_y)$ bringing the vector $\vec{V}_a$ to the center of the Bloch ball while maximizing the modulus $|\vec{V}_b|$. A bound ω_{max} on the control field is introduced such that $|\vec{\omega}| \leq \omega_{max}$. This constraint can be mathematically justified to rigorously define the optimal control problem, but also physically since only magnetic fields with a finite intensity can be produced experimentally.

The optimization problem is solved by two complementary methods, the geometric [15] and the numerical ones [5, 25], in the homogeneous and inhomogeneous cases, respectively.

First the homogeneous situation is analyzed. Our approach is based on the Pontryagin Maximum Principle (PMP) which is formulated from a pseudo-Hamiltonian $\mathcal{H}$, given by $\mathcal{H} = \vec{P}\cdot\dot{\vec{X}}$ where $\vec{X}$ is a four dimensional vector of coordinates (Y^a, Z^a, Y^b, Z^b) describing the state of the system and $\vec{P} = (P_y^a, P_z^a, P_y^b, P_z^b)$ the adjoint state, playing the role of a Lagrange multiplier. The optimal trajectory is solution of the Hamiltonian equations

$$\dot{\vec{X}} = \frac{\partial\mathcal{H}}{\partial\vec{P}} \; ; \; \dot{\vec{P}} = -\frac{\partial\mathcal{H}}{\partial\vec{X}} \tag{6.2}$$

with the boundary conditions $Y^a(T) = Z^a(T) = 0$, $Y^b(T) = -P_y^b(T)$ and $Z^b(T) = -P_z^b(T)$ at the final time T, which are required to optimize the contrast. The $\vec{X}$-coordinates satisfy the Bloch equations:

$$\left\{\begin{array}{rcl} \frac{dY^i}{dt} & = & -\omega_x Z^i - Y^i/T_2^i \\ \frac{dZ^i}{dt} & = & \omega_x Y^i + (1-Z^i)/T_1^i, \end{array}\right. \tag{S2}$$

while the dynamics of the $\vec{P}$- components is governed by the system:

$$\left\{\begin{array}{rcl} \frac{dP_y^i}{dt} & = & \omega_x P_z^i + P_y^i/T_2^i \\ \frac{dP_z^i}{dt} & = & -\omega_x P_y^i + P_z^i/T_1^i, \end{array}\right. \tag{6.3}$$

where $i = (a, b)$. The optimal control field ω_{opt} is obtained from the maximization condition $\mathcal{H}(\vec{X}, \vec{P}, \omega_{opt}) = \max_{|\omega_x|\leq\omega_{max}} \mathcal{H}(\vec{X}, \vec{P}, \omega_x)$, which leads to two types of solutions: the bang or regular ones where $\omega_x = \pm\omega_{max}$ and the singular ones for which $|\omega_x| \leq \omega_{max}$. Writing the Bloch equations in a compact form

$$\dot{\vec{X}} = \vec{F}(\vec{X}) + \omega_x\vec{G}(\vec{X}), \tag{S4}$$

where $\vec{F}$ and $\vec{G}$ are respectively two vectors of coordinates $(-Y^a/T_2^a, (1-Z^a)/T_1^a, -Y^b/T_2^b, (1-Z^b)/T_1^b)$ and $(-\omega_x Z^a, \omega_x Y^a, -\omega_x Z^b, \omega_x Y^b)$, we introduce the switching function $\phi(t) = \vec{P}\cdot\vec{G}$. It is then straightforward to see that the Hamiltonian $\mathcal{H}$ is maximized in the case where $\phi(t)$ is different from 0 (or vanishes in an isolated point) if $\omega_x(t) = \omega_{max} \times \text{sign}[\phi(t)]$. This corresponds to the regular situation. When ϕ is zero in a time interval, the problem associated to the singular case is more involved. However, by using the fact that $\dot{\phi}(t) = \ddot{\phi}(t) = 0$ on the considered interval, one can derive an analytic formula for the singular control field ω_x^s. Then:

$$\left\{\begin{array}{rcl} \dot{\phi}(t) & = & \vec{P}\cdot[\vec{F}, \vec{G}] \\ \ddot{\phi}(t) & = & \vec{P}\cdot[\vec{F}, [\vec{F}, \vec{G}]] + \omega_x^s[\vec{G}, [\vec{F}, \vec{G}]], \end{array}\right. \tag{6.4}$$

where the commutator $[\cdot,\cdot]$ of two vectors is defined in the coordinates x_i by:

$$[\vec{F}, \vec{G}]_j = \sum_i \left(\frac{\partial G_j}{\partial x_i}F_i - \frac{\partial F_j}{\partial x_i}G_i\right). \tag{6.5}$$

In addition, when the control duration is not fixed, one also know from the PMP that $\mathcal{H} = 0$, which leads to $\vec{P}\cdot\vec{F} = 0$ since $\vec{P}\cdot\vec{G} = 0$. Using the different constraints on the singular control, one finally arrives to the following analytic expression:

$$\omega_x^s = -\frac{\det(\vec{F}, \vec{G}, [\vec{F}, \vec{G}], [\vec{F}, [\vec{F}, \vec{G}]])}{\det(\vec{F}, \vec{G}, [\vec{F}, \vec{G}], [\vec{G}, [\vec{F}, \vec{G}]])}. \tag{6.6}$$

The last step of this approach consists of solving the shooting equation, that is to determine the initial adjoint state such that the corresponding Hamiltonian trajectories $(\vec{X}(t), \vec{P}(t))$ satisfy the boundary conditions at the final time.

6.2.3 Numerical approach

Due to its geometric character, this efficient method is however intrinsically limited to systems of small dimensions. Purely numerical approaches have to be used to simultaneously control the large number of spins of inhomogeneous ensemble. Due to the offset frequencies, the symmetry of revolution around the z-axis is broken and two control fields with amplitudes ω_x and ω_y have to be considered. The control problem has been solved with the GRAPE algorithm which is a standard iterative algorithm in quantum control [25]. In this case, the figure of merit to be maximized is defined as $\Phi = \overline{V_x^b(T)} - \alpha|\vec{V}^a(T)|$, where V_x^b is the x- component of the vector $\vec{V}^b$ and the bar indicates an ensemble average over all the spins of the ensemble. The parameter α measures the relative weights between the two contributions to Φ. To guarantee a reasonable final result, a relatively large value of α should be used. Note that in the original formulation of the problem for the homogeneous case, the magnitude $|\vec{V}^b(T)|$ was maximized, which requires an additional hard pulse to bring the magnetization into the transverse plane for detection. In the inhomogeneous case corresponding to the experimental setting, the given figure of merit Φ is chosen to directly maximize the detectable x- component of the average vector $\overline{\vec{V}^b(T)}$, eliminating the need for an additional hard pulse to rotate $\overline{\vec{V}^b(T)}$ into the transfer plane. The GRAPE algorithm is also based on the PMP with the pseudo-Hamiltonian $\mathcal{H} = \vec{P} \cdot \dot{\vec{X}}$, where $\vec{X}$ is now a six-dimensional vector. The extremal trajectory solution of the control problem satisfies the Hamiltonian equations

$$\dot{\vec{X}} = \frac{\partial H}{\partial \vec{P}};\ \dot{\vec{P}} = -\frac{\partial H}{\partial \vec{X}} \tag{6.7}$$

with the boundary conditions $\vec{P}(T) = -\frac{\partial \Phi}{\partial \vec{X}}(T)$ at the fixed final time T. The gradients $\partial\mathcal{H}/\partial\vec{\omega}$ are computed at each step of the iterative algorithm to indicate how each control ω_x and ω_y should be modified in the next iteration to improve the cost Φ. No bound on the control amplitudes was required during the optimizations as the resulting control amplitudes were well within the experimentally achievable limits.

6.3 NMR experiment

As a test case, typical relaxation parameters are choosen for (a) oxygenated and (b) deoxygenated blood with identical T_1 values ($T_1^{a,b} = 1.35$ s) but different T_2 values ($T_2^a = 200$ ms, $T_2^b = 50$ ms). Note that in this situation, the conventional Inversion Recovery experiment, which relies on T_1 differences cannot provide useful contrast. However, applying the optimal control approach for these parameters the global maximum of the modulus of $\vec{V}^a$ (under the condition that $|\vec{V}^b| = 0$) is found to be $|\vec{V}^a| = 0.4663$, representing the maximum achievable saturation contrast in this system. For the blood example, it can be shown that the optimal solution is the concatenation of a bang and a singular trajectory. Since the bang pulse is of negligible duration, only the singular trajectory is represented in Fig. 6.1. Note that a similar computation can be done to saturate the spin (a) and maximize $|\vec{V}^b|$, with a final result of $|\vec{V}^b| = 0.4731$. We think this saturation contrast is optimal or at least the best known results, therefore it gives the benchmark of the physical upper limit that can be reached within the experimental constraints given here by the values of the relaxation rates. The shape of the optimal pulse is shown in Fig. 6.1a. For our demonstration experiments, I did not use actual blood samples but prepared two different solutions with similar physical characteristics. The relaxation properties of oxygenated blood were approached by solution (a) consisting

of 90% D_2O, 10% glycerol and doped with $CuSO_4$ with relaxation times $T_1^a = 1.8$ s, $T_2^a = 260$ ms (as determined from CPMG-experiment) and $T_2^{*,a} = 100$ ms (as determined from the experimental line width). Deoxygenated blood was modeled by solution (b) consisting of 70% D_2O, 30% glycerol and doped with $CuSO_4$ with $T_1^b = 1.4$ s, $T_2^b = 60$ ms and $T_2^{*,b}$=30 ms. As the experimental T_2^* values [87] of the test sample were only about 2/3 of the T_2 values assumed for the optimized pulse, the pulse duration and amplitude were scaled by 2/3 and 3/2, respectively, resulting in a scaled pulse duration of 0.214 s and a maximum pulse amplitude of the order of 10 Hz (see Fig. 6.1a). The optimal control field was implemented experimentally as a shaped pulse on a standard Bruker Avance III 600 MHz spectrometer and the experimental trajectories were measured using two different samples in different test tubes in order to approach ideal experimental conditions with negligible magnetic field inhomogeneities. Under these conditions, the dynamics is described with high accuracy by the Bloch equations (6.1). The simulated and experimental trajectories of the two magnetization vectors $\vec{V}^a(t)$ and $\vec{V}^b(t)$ are shown in Fig. 6.1b and a good match is found between theory and experiment.

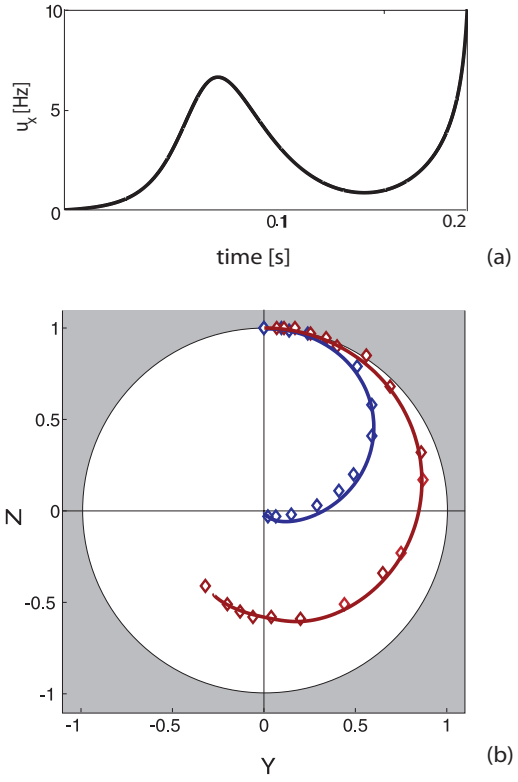

Figure 6.1: Optimal pulse sequence and trajectories for negligible B_0 and B_1 inhomogeneities. (a), The control amplitude $u_x(t) = \omega_x(t)/(2\pi)$ is shown for the optimal pulse sequence to maximize $|\vec{V}^a|$ under the condition that $|\vec{V}^b| = 0$. **(b)**, Corresponding simulated (solid curves) and experimental (open diamonds) trajectories of $\vec{V}^a(t)$ (red) and $\vec{V}^b(t)$ (blue) in the (Y, Z) plane for a homogeneous ensemble of spin particles.

So far, I assumed that there is no experimental imperfection due to magnetic field inhomogeneities, which are however not negligible in realistic imaging experiments and have therefore to be taken into account. Nevertheless, it is important to point out that the analytical PMP-based optimal solution in the absence of experimental imperfections

provides a previously unavailable physical upper limit of the maximum achievable saturation contrast, the inhomogeneities having a detrimental effect on the final result. This bound, which can be determined for any set of relaxation parameters, is thus relevant for any imaging contrast problem. Hence, it gives a fundamental benchmark to assess the performance of standard methods and numerically optimized pulse sequences in this domain.

6.4 Imaging experiment

6.4.1 Test sample and field inhomogeneity

To perform a realistic imaging experiment, I designed a test sample consisting of a small test tube in a larger tube with an outer diameter of 8 mm, forming two compartments filled with solutions (a) and (b) corresponding to the relaxation rates of deoxygenated and oxygenated blood, see Fig. 6.2 for a schematic representation. In general, the frequency offsets created by the B_0 inhomogeneities are negligible if they are dominated by the amplitude of the control field (in units of Hz). However, the control amplitude of the analytically optimal pulse sequence shown in Fig. 6.1a is less than 10 Hz, which is smaller than the resonance offset variation due to B_0 inhomogeneities (see Fig. 6.3a) and therefore, the optimal sequence derived analytically for an ideal case is not expected to work in the experimental micro imaging setting. In addition, the experimental variation of B_1 scaling was not considered in the analytical solution and is also expected to have detrimental effects on the pulse performance. Figure 6.3 shows the experimentally measured spatial B_0 and B_1 distributions in the central slice of the sample. The variation of B_0 corresponds to resonance frequency shifts ω between 0 and -30 Hz, while the experimental scaling of the B_1 field (which is proportional to the control amplitude) is $\pm 20\%$.

Measurement method of the B_0 and B_1 field maps. Mapping of local B_0 offsets was accomplished by evaluating the signal phase evolution between two echoes acquired in a dual-echo gradient pulse sequence [88]. The echo times of the 3D image acquisition were $TE_1 = 1.5$ ms and $TE_2 = 11.5$ ms. Figure 3a of the main text shows the B_0 field map in the central axial slice. The amplitude of the B_1 excitation field was measured by using the cosine-like dependence of the remaining signal after a saturation pulse and fitting to a curve measured with multiple saturation flip angles [93]. The applied saturation flip angles were $10°, 20°, \ldots, 300°$. Robust B_1 mapping was achieved by fitting a signal model to the acquired slice-selective gradient echo signal in a linear least-squares sense.

6.4.2 Numerical pulses

In order to take into account the experimentally measured B_0 and B_1 distributions, numerically optimized pulse sequences were computed with the GRAPE algorithm [25], which is a standard iterative algorithm to solve the optimization equations. The pulses are designed to work for an ensemble of spins approximately within the range of the B_0 and B_1inhomogeneities experimentally measured. The pulses are designed to work for an ensemble of spins with variations of the offset frequency of ± 20 Hz and for a variation of the B_1 scaling factor of $\pm 20\%$. In the numerical optimizations, I fixed the pulse duration to the duration of the corresponding analytic-PMP pulse for the homogeneous case. Compared to the fundamental contrast benchmark ($|V^a| = 0.47$ and $|V^b| = 0$) provided by the PMP-based analytical solution, the minimum value (worst case) of $|V^a|$ for the considered range of B_0 and B_1 inhomogeneities is 0.37 (that is 79%

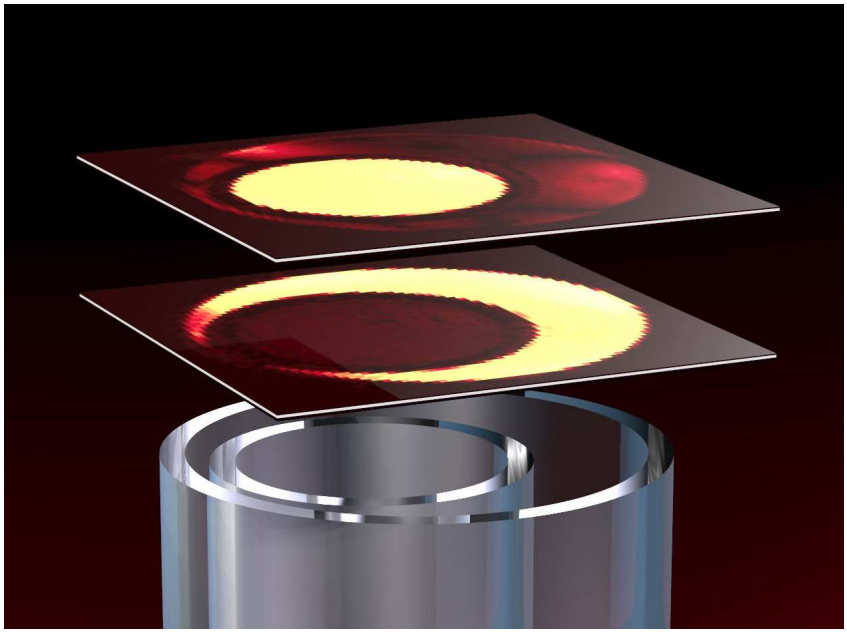

Figure 6.2: Geometry of the test sample used for the imaging experiments. In the micro imaging experiments, the sample consists of two test tubes with outer diameters of 5 mm and 8 mm. The outer and inner volumes were respectively filled with the two solutions corresponding to (a) oxygenated and (b) deoxygenated blood. The two slices represent the experimental results after the saturation of the samples (a) (top) and (b) (bottom). (see also the results of Fig. 6.15)

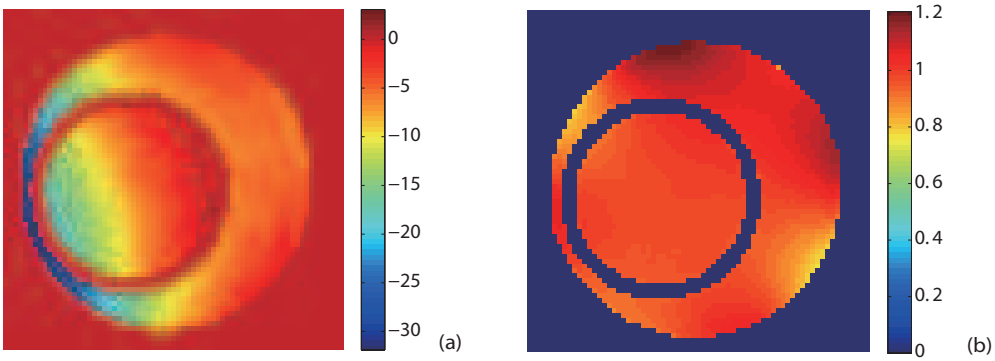

Figure 6.3: Experimental spatial B_0 and B_1 distributions. Spatial distributions of the B_0 (a) and B_1 (b) amplitudes in the central slice of the sample. The B_0 variation is represented by the corresponding ^{1}H frequency offsets in units of Hz as a function of the spatial position, while the B_1 variation is described by a dimensionless scaling factor.

of the physically maximum saturation contrast achievable) while the maximum value (worst case) of the incompletely suppressed $|V^b|$ is 0.054. Conversely, when the goal is to saturate spin (a) and to maximize the magnetization vector of spin (b), the optimal pulse sequence yields $|\vec{V}^a| = 0.047$ and $|\vec{V}^b| = 0.33$.

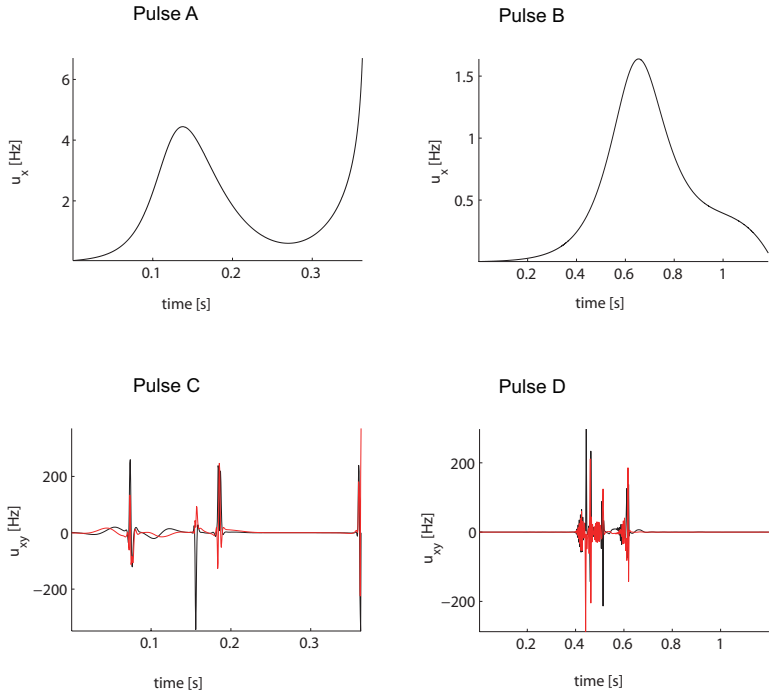

Figure 6.4: The pulse shapes of the analytically optimized pulse A (top left panel) and B (top right panel), as well as the numerically optimized pulse C (bottom left panel) and D (bottom right panel). Pulses A and C are optimized to maximize $|\vec{V}^a|$ (the oxygenated spin) under the condition that $|\vec{V}^b| = 0$ (the deoxygenated spin), while B and D are optimized to maximize $|\vec{V}^b|$ (the deoxygenated spin) under the condition that $|\vec{V}^a| = 0$ (the oxygenated spin).

Figure 6.4 shows the pulse shapes of the analytically optimized pulses A and B (top left and right panels, respectively) and the numerically optimized robust contrast pulses C and D (bottom left and right panels, respectively). Pulses A and C are optimized to maximize $|\vec{V}^a|$ (the oxygenated spin) under the condition that $|\vec{V}^b| = 0$ (the deoxygenated spin), while B and D are optimized to maximize $|\vec{V}^b|$ (the deoxygenated spin) under the condition that $|\vec{V}^a| = 0$ (the oxygenated spin). As expected, the optimized pulses contain periods with very strong pulse amplitudes (note the different vertical scale of the plots) to refocus the effects of B_0 inhomogeneity. In order to compensate B_1 inhomogeneity, pulses C nad D have not only x but also y amplitudes.

Magnetization trajectories for pulses A (top left) , B (top right), C (bottom left) and D (bottom right) are shown for ideal B_0 and B_1 ($B_0 = 0$ and $B_1 = 1$) values in Figure 6.5 (for the relaxation parameters of "deoxygenated spin") and Figure 6.6 (for the relaxation parameters of "oxygenated spin"). As for pulses C and D the trajectories are not limited to the yz plane, I plotted the transverse component $xy = \sqrt{x^2 + y^2}$ and the z component of the trajectories.

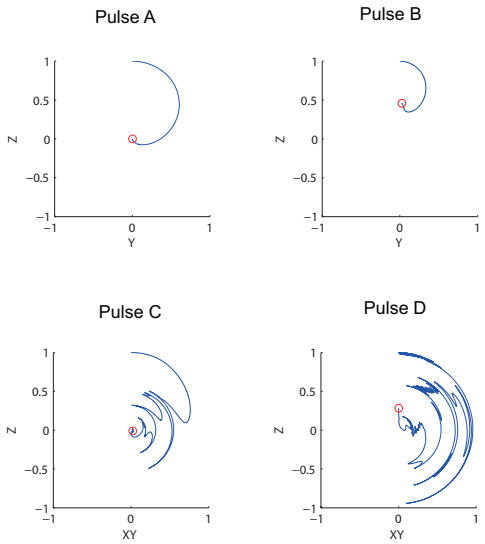

Figure 6.5: The corresponding trajectories for the deoxygenated spin of pulses A-D in Figure 6.4.

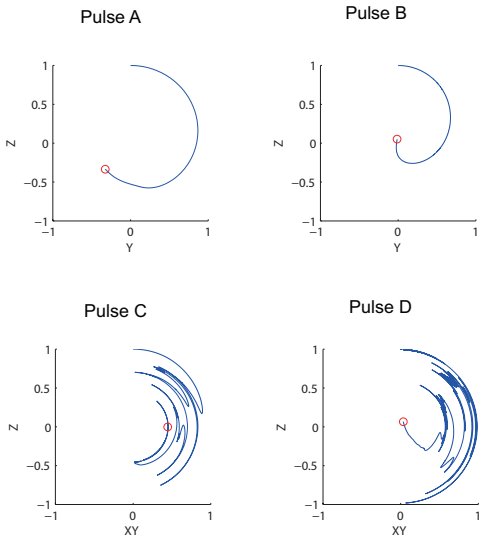

Figure 6.6: The corresponding trajectories for the oxygenated spin of pulses A-D in Figure 6.4.

Robustness against the field inhomogeneity The robustness of the numerical pulses C and D (Figure 6.4, bottom panels) compared to the analytical pulses A and B (Figure 6.4, top panels) against the field inhomogeneity is demonstrated in Figure 6.8 (for the relaxation parameters of "deoxygenated spin") and Figure 6.9 (for the relaxation parameters of "oxygenated spin"). The figures show the simulated magnitude of the final magnetization after pulses A, pulse B, pulse C and pulse D for variations of the offset frequency (corresponding to B_0 inhomogeneity) of ± 20 Hz and for variations of the B_1 scaling factor of $\pm 20\%$. As expected, the numerical pulses work well for the whole range of field inhomogeneity chosen for the optimization while the analytical pulse function only in the area close to the ideal case. For more details, figure 6.7 shows the simulation of the final contrast of the numerical pulses for the same range of B_0 and B_1 variations.

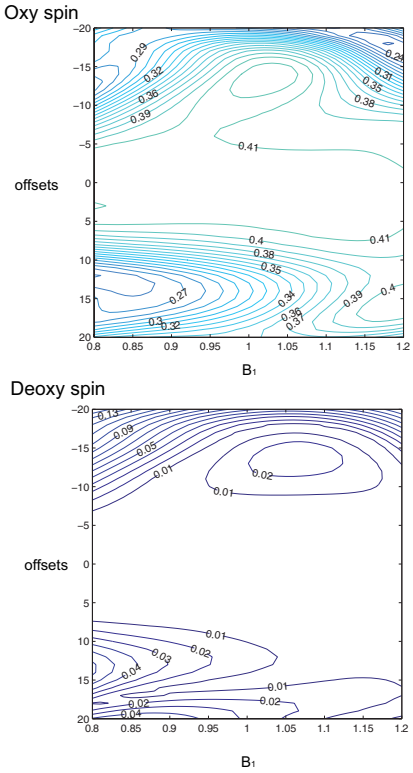

Figure 6.7: Simulated final contrast: Contour plot of the final contrast, the saturation of the deoxy II sample) as a function of the B_0 and B_1 inhomogeneities, which range respectively from -20Hz to 20Hz and from -20% to 20%. The optimized pulse of the experiment has been used in the numerical computation.

Robustness against T_1 and T_2 Figure 6.10 demonstrates the simulation results of the analytical and the numerical pulses against the variations of the relaxation parameters: $0 \leq T_1 \leq 5$ and $0 \leq T_2 \leq 0.6$. It shows that the contrast changes very little for T_1 variations, while changes quite dramatically for T_2 variations.

From the analytic to the experimental optimal pulses. Here presents a series of optimizations for successively decreasing field inhomogeneities, down to inhomogeneities that no longer result in massive qualitative changes in optimum trajectoryes from the perfectly homogeneous case. Figures 6.4 show that the optimal pulse sequence has a very complicated structure due to the strong B_0 and B_1 inhomogeneities measured in

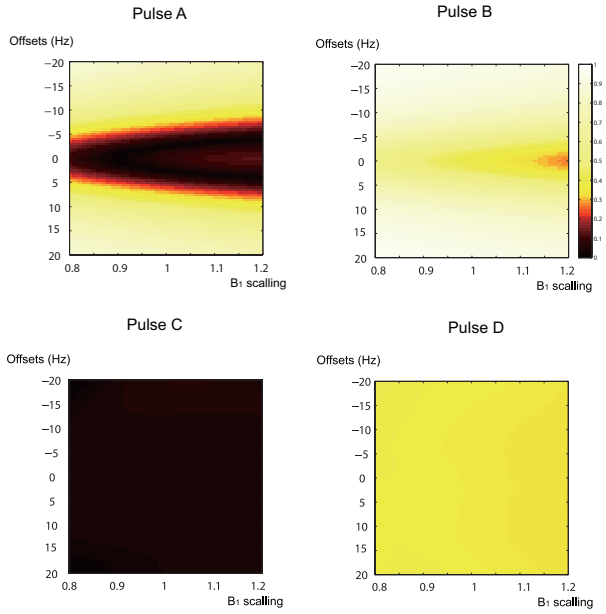

Figure 6.8: The simulated robustness of the analytical and the numerical pulses (see Fig. 6.4 A-D) against the B_0 and B_1 inhomogeneity. Here shows the final magnetization after the pulses A-D for the deoxygenated spin.

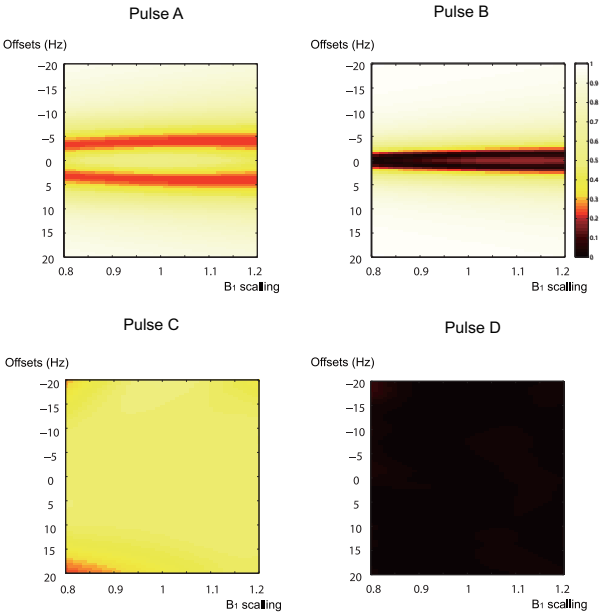

Figure 6.9: Same as Fig. 6.8, but for the oxygenated spin.

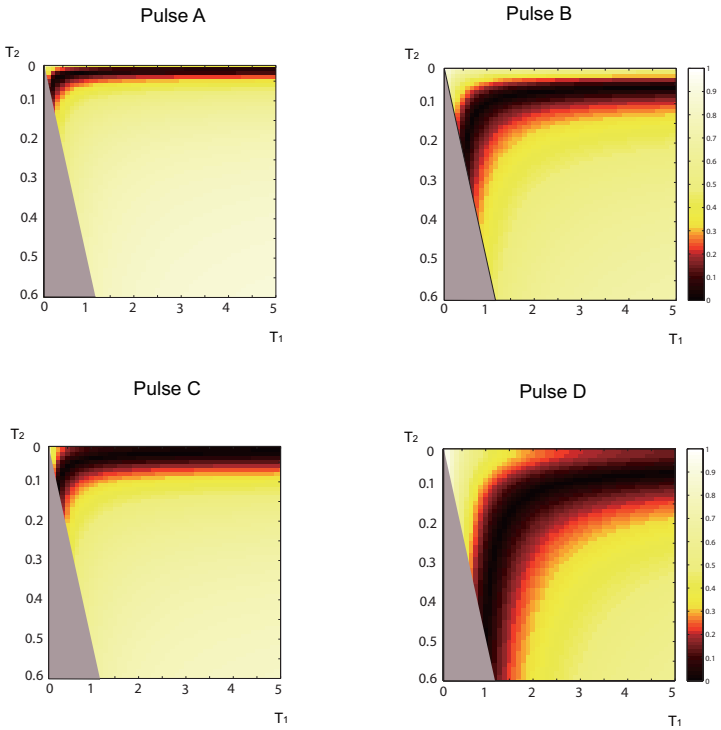

Figure 6.10: The simlated robustness of the analytical and the numerical pulses against variation of T_1 and T_2 relaxation times. The grey area represents the physically forbidden region due to the rule that $2 * T_1 \geq T_2$.

the experiment. This complexity makes the interpretation of the final optimal solution difficult. In particular, no insight is given about the transition from the analytic pulse used in the homogeneous case to the purely numerical solution suited to the experimental situation. This section presents different numerical results which illustrate the respective properties of the two pulses.

One of the main characteristics of the numerical GRAPE solution with respect to the analytic one is its robustness with respect to B_0-inhomogeneities. This point is illustrated in Figs. 6.8 and 6.9, as well as in Figs. 6.11 and 6.12, which plot the time evolution of XYZ magnetization for different offsets. Note that the final magnetization vectors are very different according to the offset in the case of the analytic pulse, while the final vectors are almost the same for the robust GRAPE pulse. This behavior was expected since the analytic solution has been optimized only for the on-resonant dynamics.

Different optimizations with the GRAPE algorithm have been then undertaken to explore the transition from one solution to the other. The results are represented in Fig. 6.13 and 6.14, where, to simplify the structure of the pulse, only the offset inhomogeneities have been taken into account. The same work could also be done for the B_1-imperfections. The offset ranges extend from 0 Hz to 30 Hz from left to right, while the last column corresponds to the experimental pulse. Note that the analytic solution is very close to the pulse depicted in the first column of Fig. 6.13 and 6.14, which was designed here by the GRAPE algorithm. The only difference between the two solutions is the final bang pulse which is due to the two different definitions used for the contrast. Observed that short and intense peaks appear at different times with increasing offset range. They can be associated to standard refocusing pulses, which are used to improve the robustness of the control pulse with respect to the B_0 inhomogeneities. The number and the amplitude of the peaks increase as the offset range increases. For sake of illustration, the dynamics of the on-resonance spin and of the spin with the maximum offset (e.g. a spin with an offset of 10 Hz for a range of 20 Hz) have been represented in Fig. 6.13 and Fig. 6.14, respectively.

6.4.3 Application of the optimized pulse sequence

For the imaging experiment, the H_2O content was increased in the sample in order to have a sufficient signal-to-noise ratio. The outer and inner volumes of the sample were filled with the following solutions: "oxy sample II" (80% D_2O, 10% H_2O, 10% glycerol doped with $CuSO_4$ with relaxation times of T_1=2.6 s and T_2^*=100 ms) and "deoxy sample II" (60% D_2O, 10% H_2O, 30% glycerol doped with $CuSO_4$ with relaxation times of T_1=1.4 s and T_2^*=30 ms). The optimal pulses were implemented into a gradient echo pulse sequence [94] without slice selection. The experiments were performed with a 600MHz Bruker Avance III spectrometer equipped with a micro-imaging unit. The field of view (FOV) was 15mm x15 mm, and in the third dimension it was limited to approximately 10 mm by coil sensitivity. The repetition time (TR) is 7 s and the echo time (TE) is 2 ms with the matrix size 128x128. Figure 6.15 shows the experimental imgaging results, which are in the good agreement with the simulation data.

6.5 Summary

The maximized saturation contrast based on different relaxation times T_1 and T_2 is demonstrated in magnetic resonance imaging within given experimental constraints.

Starting from the analytic optimal solution of the homogeneous case, I have then designed a particular pulse sequence using numerical tools of optimal control theory to approach in a realistic experiment this physical limit. One of the main advantages of this contrast enhancement is its general character since the optimal control fields can be computed with standard routines published in the literature and implemented on a standard NMR spectrometer without requiring specific materials and process techniques.

The efficiency of this approach was shown in a laboratory experiment using a model system for the relaxation parameters of deoxygenated and oxygenated blood. The presented method fully exploits the differences of both T_1 and T_2 to create the maximum possible saturation contrast as opposed to conventional approaches based on T_1 or T_2 differences. The combined analytical and numerical optimal control approach is not limited to the definition of saturation contrast (motivated by typical magnitude mode imaging experiments) used here for demonstration, but can also be applied to more general definitions of relaxation-based contrast, e.g. for phase-sensitive images and for a wide variety of possible host imaging sequences that can be applied after the contrast pulse module [88]. Furthermore, the flexibility of the optimal control approach makes it possible to include experimental constraints such as bounds on the control amplitude or pulse energy or non-linear effects such as radiation damping [39].

Hope that the presented principles will find practical applications in MRI and in particular in medical imaging, where increased contrast and sensitivity could not only help in the diagnosis but could also reduce the required concentration of commonly used contrast agents, which could be beneficial to the patient.

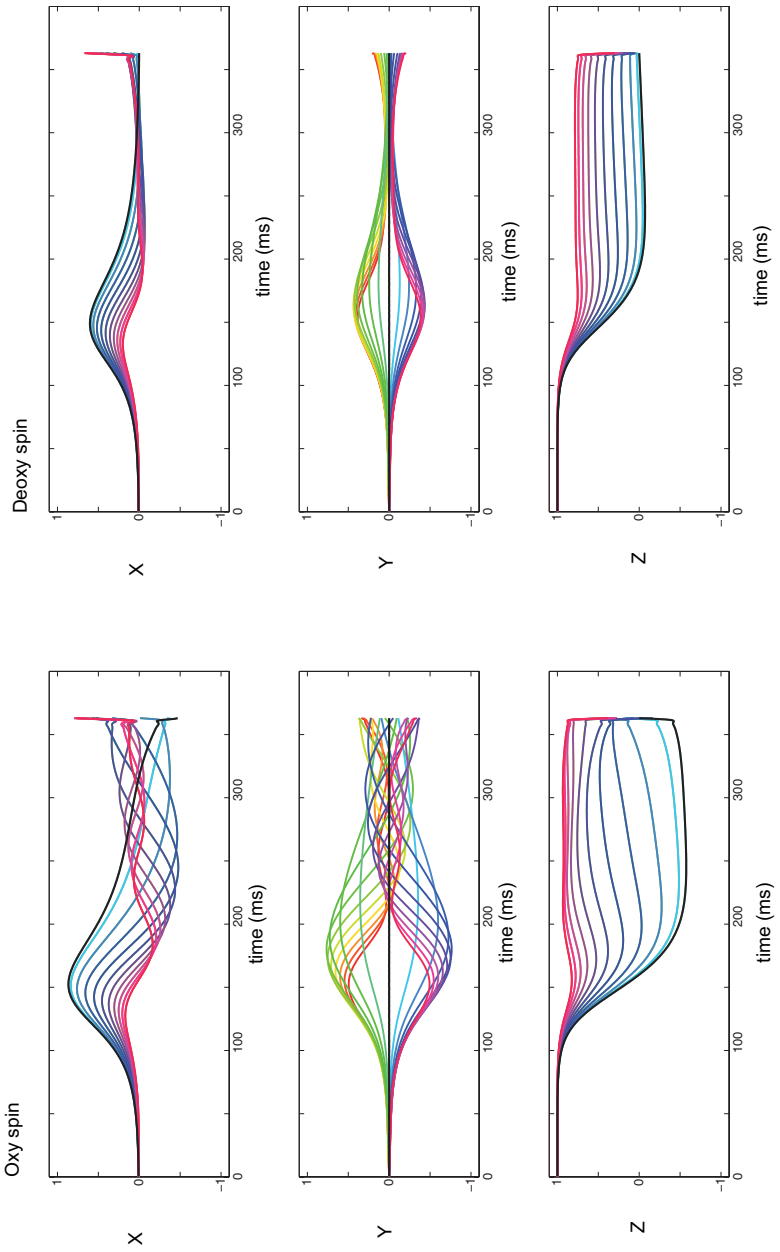

Figure 6.11: Evolution of the X, Y and Z components of the magnetization vectors corresponding to the oxygenated and desoxygenated blood samples under the effect of the analytic pulse. The different trajectories are associated to different offsets in the range from -10 kHz to 10 kHz (the on-resonance case is plotted in black). The goal of the control is to saturate the desoxygenated spin, while maximizing the transverse component of the oxygenated one.

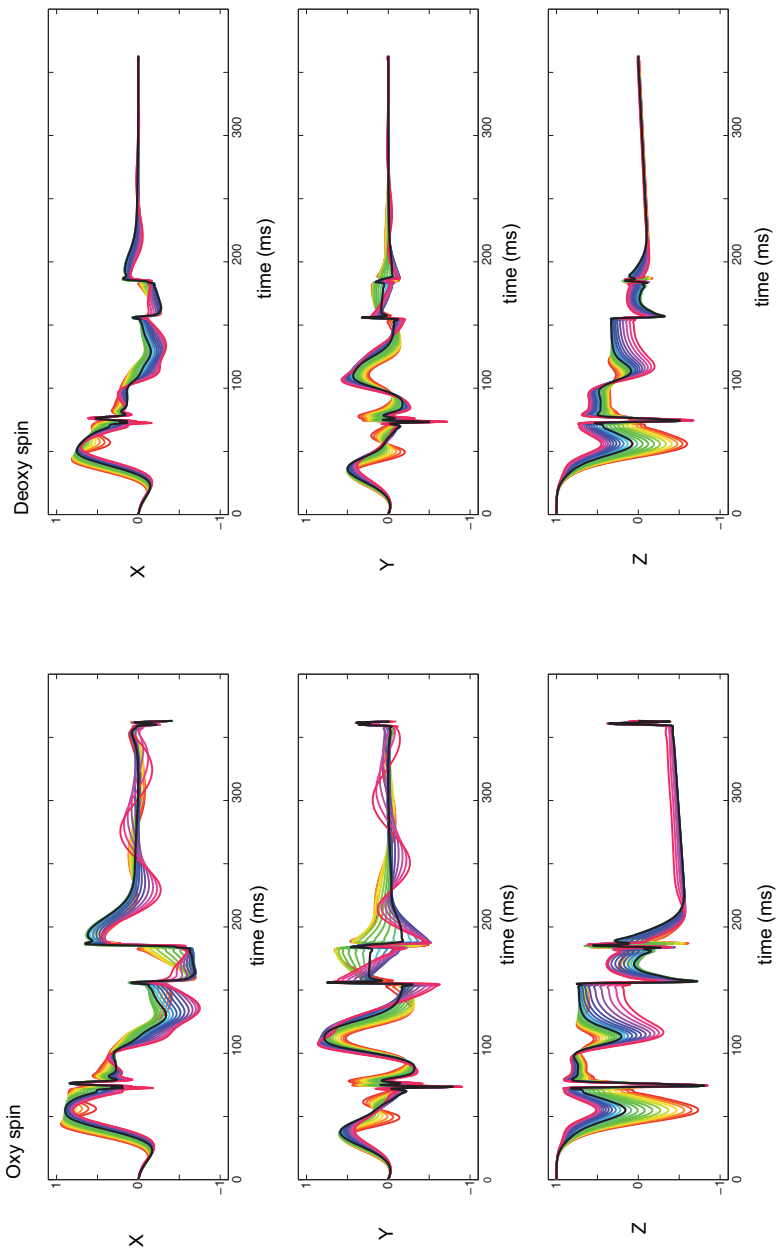

Figure 6.12: Same as in Fig. 6.11 but for a numerical optimized pulse. Since this solution is robust within the offset range, the final magnetization vectors associated to the different offset terms are almost the same.

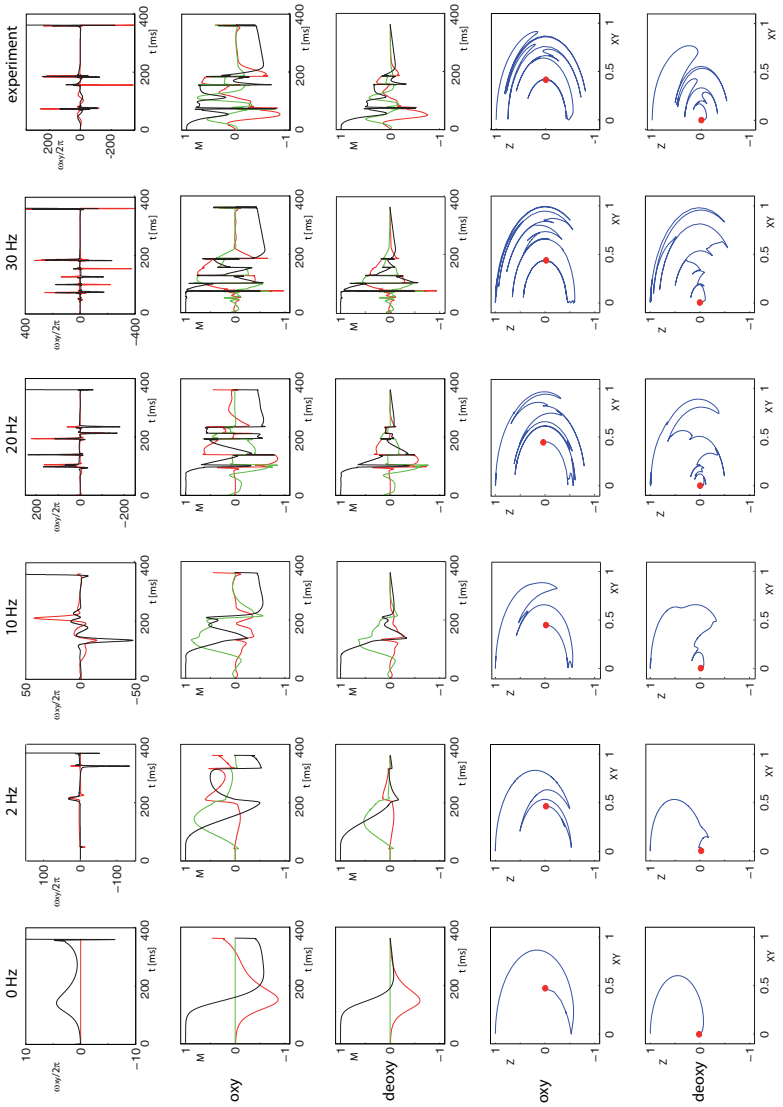

Figure 6.13: Transition from the analytic to the experimental pulses: The first row displays the evolution of the optimized pulses along the x- (red) and y- (black) directions for an offset range extending from 0 Hz (on-resonance case) to 30 Hz and no B_1 inhomogeneity. The last column recalls the results obtained for the experimental conditions (i.e. with B_0- and B_1-inhomogeneities). The second and third rows represent, in the on-resonance case, the corresponding trajectories of the magnetization vectors for the two spins as a function of time. The black, red and green curves depict respectively the z-, x- and y- components. The evolution of the Z- coordinate versus the $XY = \sqrt{M_x^2 + M_y^2}$ component is plotted in the last two rows.

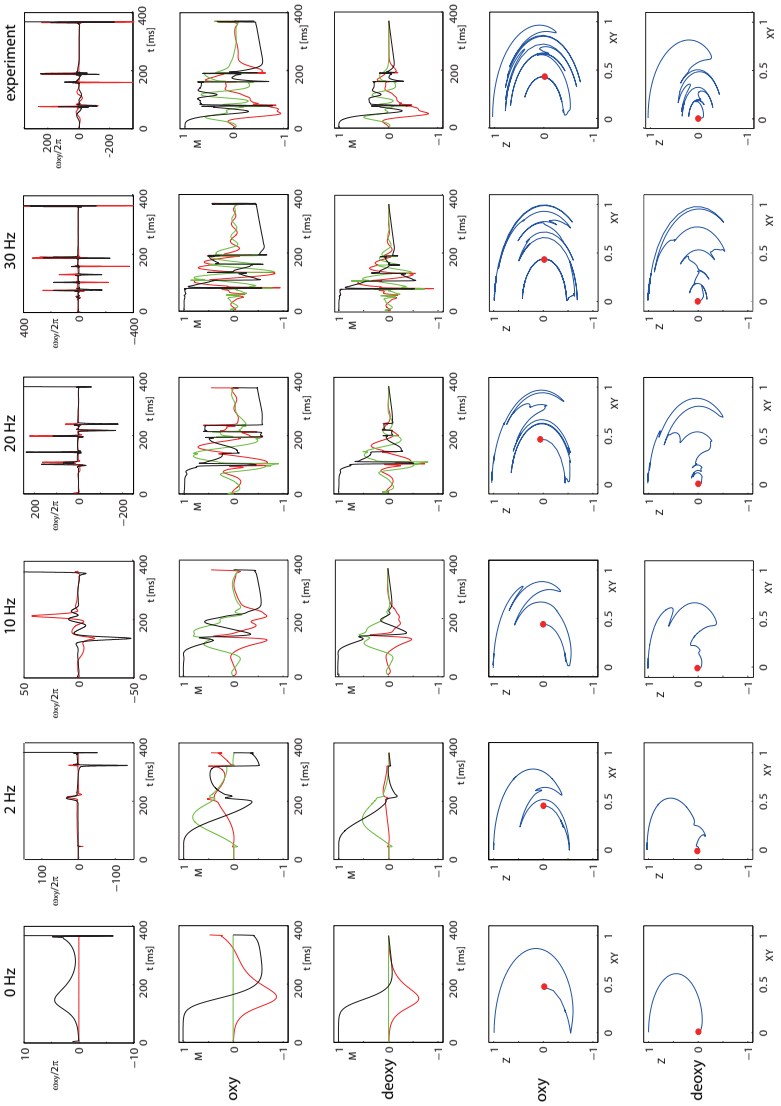

Figure 6.14: Same as in Fig. 6.13 but the dynamics of the spin with the maximum offset in the considered range has been plotted (see the text for details).

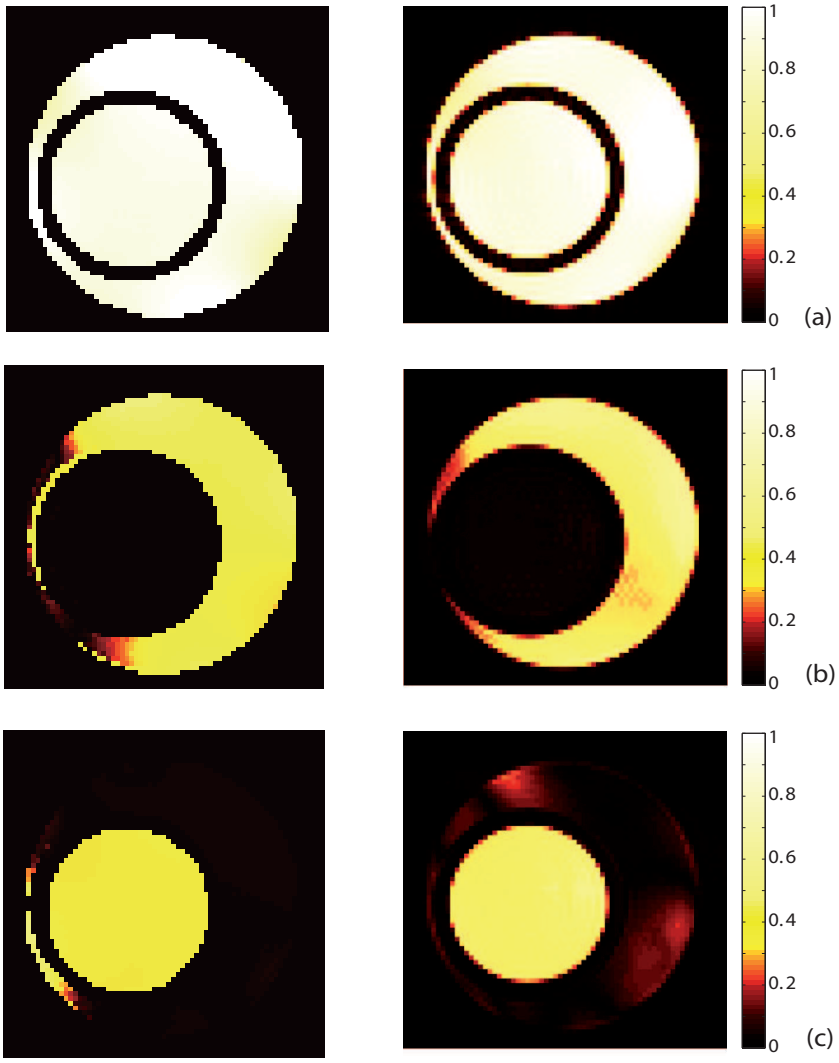

Figure 6.15: Experimental implementation (right column) of the robust optimal pulse, together with the simulation data (left column). Optimization of the contrast when the deoxygenated (b) or the oxygenated (c) blood is saturated. Figure (a) displays the reference image after the application of a 90 degree pulse.

Chapter 7

Shaped pulses for increased excitation bandwidth in EPR

7.1 Introduction

This chapter is a part of article [95] as a collaboration with the research group of Prof. T. Prisner in Frankfurt. In this project, I am responsible for the numerical pulse optimization together with the analysis of the transient effect, while the experimental part was done by Ph. Spindler of Prof. Prisner's group. Pulsed excitation has many advantages in most applications of magnetic resonance spectroscopy, like liquid and solid state NMR, EPR, DNP and imaging. The reason is the multiplex advantage, leading to a strongly increased signal-to-noise ratio of the pulse experiment compared to continuous-wave excitation [96] and the strongly enhanced possibilities to select specific interactions and to optimize polarization and coherence transfer pathways between different spin systems [96–105]. Simple rectangular pulses (commonly referred to as hard pulses) work very efficiently as long as the excitation bandwidth, defined by the magnetic field strength and pulse length of the exciting RF or MW field, exceeds the spectral width of the investigated spin system, as is the case especially in many applications in liquid state NMR [106]. Roughly speaking the excitation field strength $\omega_1 = \gamma B_1$ in frequency units has to be larger than the spectral width, where γ is the gyromagnetic ratio for the respective spin system.

However, there are many cases were the excitation field strength cannot be chosen large enough to fulfill this condition. This holds especially for solid state applications in NMR as well as EPR, where the intrinsic inhomogeneous line width can easily be in the MHz to GHz region. Such high excitation field strengths cannot be achieved because of technical limitations, such as limited excitation power, arcing or heating of the sample itself. In such cases, the classical pulse sequences usually still work, but with reduced efficiency. This strongly reduces the sensitivity of the experiment and complicates the quantitative analysis of the obtained signals. In extreme cases, the excitation bandwidth is small compared to the spectral width, so that only few spins are on-resonant and interacting with the excitation field (called A spins), while most of the spin system is not excited (called B spins). The A and B spins in such samples usually strongly interact, leading to uncontrolled polarization and coherence transfer after the RF excitation by relaxation pathways [107,108]. The excitation hole created by classical rectangular pulses with constant phase is frayed, complicating again any quantitative analysis of the time domain signal [109].

Soon the idea was followed to replace short pulses with fixed amplitude and phase by extended pulses with variable amplitude and/or phase to achieve higher excitation bandwidth for a given excitation field strength. Different approaches in this direction as 'Composite Pulses' or 'Stochastic Excitation' have been pursued in the field of NMR [103, 110–115] and EPR [5, 25, 47, 116]. More recently, Optimum Control Theory has been used very successfully in the field of NMR spectroscopy to improve excitation bandwidth and polarization and coherence transfer efficiencies in liquid and solid state NMR experiments [117–119].

Optimal control theory provides powerful analytical and numerical tools to solve very general optimization problems. Analytical solutions have been derived for time-optimal [11, 119] and relaxation-optimized [71, 73] pulse sequences in uncoupled and coupled nuclear spin systems, establishing physical limits for minimal transfer times or minimal relaxation losses, respectively. In addition to powerful analytical tools, optimal control theory also provides extremely efficient numerical algorithms for the optimization of pulse-sequences, such as the GRAPE (gradient ascent pulse engineering) algorithm, exploiting the known equation of motion for the spin system [27, 75, 117]. With this algorithm it is possible to optimize tens of thousands of pulse sequence parameters, which makes it possible to explore the physical limits of pulse performance [29, 39, 120]. As the search is not limited to previously known pulse families, the solution space is a generalization of commonly used shaped pulses parameterized by a relatively small number of Gaussian pulses or Fourier coefficients, adiabatic or composite pulses [26, 110].

The generality and flexibility of the optimal control approach allows the pulse designer to include physical effects such as relaxation [121], radiation damping [122], experimental constraints such as limited pulse amplitude or pulse power, and experimental imperfections such as B_1 inhomogeneity [123, 124] or transient effects to find highly robust pulses suitable for practical applications under realistic conditions. Furthermore, optimal control methods are not limited to the optimization of individual pulses, but can also be used to design mutually compensating sequences of pulses [39].

To transfer such concepts and ideas into the field of EPR spectroscopy is challenging because of the many orders of magnitude changed time scales and spectral widths, related to the much stronger electron spin compared to nuclear spin systems. In EPR spectroscopy typical spectral widths range from $10 - 100$ MHz for radicals, up to the GHz range for low-spin transition metal systems, arriving at the THz regime for some high spin metals and complexes. In a similar way the transverse relaxation times range from microseconds to picoseconds, depending on the chemical nature and temperature of the sample. This has to be compared to typical magnetic field strengths B_1 in the order of mT and correspondingly pulse lengths of a few nanoseconds achieved in pulse EPR experiments. Usually a microwave resonator is used to achieve such excitation field strengths at the sample. At the typical spectrometer frequencies of 9 or 34 GHz excitation frequency (X- or Q-band), the quality factor Q of the cavity limits the achievable bandwidth [125]. The corresponding response time τ_r of the mw resonator sets a natural limit to spin manipulations in the nanosecond region and introduces also a dead time for detection in the range of $50-100$ ns after the excitation pulses [126–129]. Because of this reason, most paramagnetic transition metals cannot be observed at room temperature by pulsed EPR methods, where the transversal relaxation times are shorter than the dead time of the spectrometer. At higher magnetic fields ($3.4 - 9.4$ T), corresponding to 95 and 260 GHz (W-band / sub-mm band), the situation is usually opposite. At these high frequencies the bandwidth of the microwave cavity is not the limiting factor anymore, but the accessible microwave power [5, 130, 131]. Therefore, most pulsed EPR experiments at any magnetic field strength suffer from such experimental limitations:

while field-swept EPR and FT-EPR [132–134] are restricted in their application mostly to organic radicals or to low temperatures because of the dead-time problem, other pulsed EPR experiments which involve two electron spins or a coupled electron-nuclear spin system, as for example DQ-EPR [135,136], HYSCORE [137], ESEEM [138], pulsed ELDOR or FT-EPR detected NMR [139,140] and REFINE [141] perform non-ideal because of too small excitation bandwidth and non-ideal pulse behavior. In this chaper, following things are described: the development of broadband excitation pulses for EPR spectroscopy by optimum control theory, the hardware implementation of a pulse shaping device into a commercial EleXSys pulse EPR spectrometer to accommodate the necessary fast amplitude and phase modulations, discuss specific technical limitations of the EPR spectrometer and finally speculate about the potential of this method for further EPR applications.

7.2 Materials and methods

All experiments were performed on a commercial pulse X-band EPR spectrometer (Bruker EleXSys) modified by a custom made pulse-forming unit (innovative technical systems its) (Fig. 7.1) in the group of Prof. T. Prisner in Frankfurt. This unit allows to apply extended pulses with 14 bit amplitude resolution, 1ns time resolution and a maximum pulse length of 32 μs. It consists of two parallel fast DACs with 90 degree phase shift, which drive the I and Q port of the modulator (Fig. 7.1), allowing to obtain arbitrary phase of the pulse after the mixing process. The setup includes a low-pass filter with a cutoff at 400 MHz, to remove the clock frequency residual signal. The low power output from the Bruker bridge serves as LO carrier frequency and is modulated by the two DACs from the pulse-forming unit. In order to correct the phase and amplitude imbalances of the modulator the AWG offers two adjusting possibilities. An offset can be put on each DAC output independently to minimize the LO leakage. To achieve amplitude parity between the I and Q ports of the modulator each DAC output can be scaled by a constant factor.

The output of the pulse forming unit is preamplified with 18dB by a linear amplifier to an output power of 6dBm to obtain the optimum input level for the 1kW high-power TWT amplifier (Applied System Engineering). The pulse-forming unit was synchronized with the pulse programmer (Bruker pattern jet) of the EleXSys spectrometer. At this stage a jitter of 2 ns was observed for the 2ns pattern jet. For the applications shown here the output power of the spectrometer was artificial reduced to 200 W, due to the bandwidth limitation of the microwave resonator at X-band frequencies (see below).

Experiments to monitor the bandwidth of the new excitation pulses were performed with a small single crystal (0.5x0.3x0.3 mm) of the organic conductor Fluoranthenyl-hexafluorophosphate ($(Flouranthene)_2 \bullet^+ PF_6^-$) [6]. These crystals grow in long, thin needles and exhibit a single homogeneous EPR linewidth of $\approx 1\ \mu$T at X-band frequencies and room temperature. The quadrature detected FID signal of this sample was used to measure stepwise the excitation bandwidth of the new developed pulses by changing the external magnetic field in steps of 14 μT over a total range of 7 mT (corresponding to a frequency range of $\pm$100 MHz).

The FT-EPR experiments were performed with a degassed and sealed perynaphtneyl (PNT) sample dissolved in paraffin oil (1 μM). This stable organic radical exhibits a well resolved spectrum (linewidth of $\approx 20\ \mu$T) consisting of 28 hyperfine lines from 6 equivalent protons with 17.6 MHz hyperfine coupling and 3 equivalent protons with a coupling of 5 MHz. The total width of the spectra is 121 MHz. As solid test sample, 1, 3-bis(diphenylene)-2-phenylallyl (BDPA) in polystyrene is used, which exhibits a 20MHz

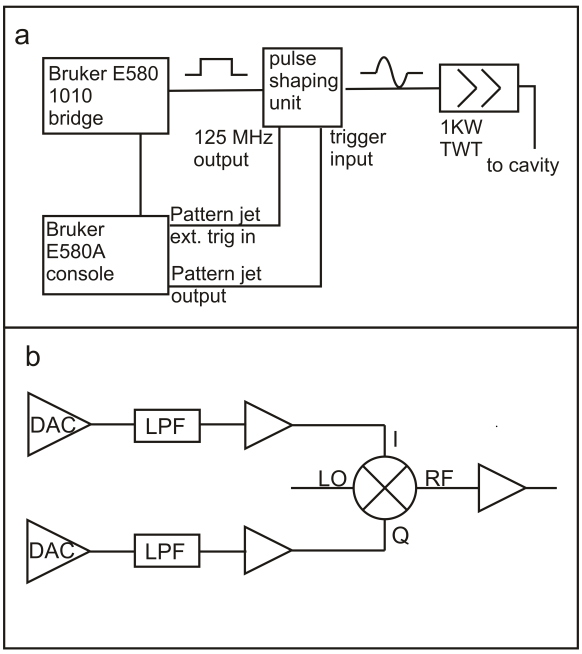

Figure 7.1: Block diagram of modified pulse X-band EPR spectrometer (a) Detail of the pulse shaping unit (b) with two 14 bit DACs operating at 1 GHz clock speed followed by a Tschebyscheff low pass filter with a cutoff frequency of 450 MHz. The modulator (Marki IQ0714LXP) operates at LO frequencies from 7 GHz to 14 GHz and offers an IF bandwidth of 500 MHz.

broad EPR line dominated by unresolved proton hyperfine interactions. This sample has a transversal relaxation time of 2 μs at room temperature.

7.3 Quality factor

For simplicity, here is focused on pulses for uncoupled spins, where the equation of motion reduces to the well-known Bloch equations. The following problem is considered: to transfer an initial magnetization vector $M(0) = (0, 0, 1)^t$(where the subscript t indicates the transpose of the vector) to a desired target state for a specified range of offsets $v_{off}^{min} \leq v_{off} \leq v_{off}^{max}$ and with a desired degree of tolerance with respect to B_1 inhomogeneity or B_1 miscalibration, which is specified by a scaling factor $s^{min} \leq s \leq s^{max}$. In order to optimize a given (shaped) pulse with x and y amplitudes $u_x(t)$ and $u_y(t)$ and overall duration T, one need to define an overall quality factor that quantifies the performance of the pulse [117]:

$$\Phi = \frac{1}{N_{off} N_s} \sum_{k=1}^{N_{off}} \sum_{k=1}^{N_s} \phi(v_k, s_l) \tag{7.1}$$

where N_{off} and N_s are the numbers of equidistant samples at offsets v_k and B_1 scaling factor s_l, repectively. Defining a final magnetization vector $M(T)$ and the target vector F, common choices for the local quality factor $\phi(v_k, s_l)$ are:

$$\phi_P(v_k, s_l) = M(T)F = \sum_{\alpha \in x,y,z}^{3} M_\alpha(T) F_\alpha \tag{7.2}$$

$$\phi_w(v_k, s_l) = \sum_{\alpha \in x,y,z} (M_\alpha(T) - F_\alpha)^2 \tag{7.3}$$

The local quality factor ϕ_P [25] is maximized. The local quality factor ϕ_w [6] is minimized and incorporates the weighting factors a_x,a_y and a_z for the x, y, and z components of the difference vector, respectively. While ϕ_P simply measures the projection of the final magnetization vector onto the target vector, ϕ_w offers more flexibility and, in particular, allows one to better defined the phase of the final magnetization vector.

7.4 Experimental results

7.4.1 Spectrometer impulse response

All passive or active microwave components cause linear or nonlinear distortions of the pulse shape. The most obvious component is the microwave resonator, which is used to increase the B_1 field strength at the sample as well as the detection sensitivity. One approach to characterize linear distortions of the system is to measure the impulse response function $h(t)$. This function is the signal response of the system to a delta-shaped input pulse excitation. Linear response theory states, that once this function is known, every output signal $y(t)$ can be calculated by convolution of the input $x(t)$ with the impulse response $h(t)$

$$y(t) = \int_{-\infty}^{\infty} h(\tau) \bullet x(t - \tau) d\tau \tag{7.4}$$

Therefore, in principle, the response function $h(t)$ can be obtained by deconvolution of the measured output signal $y(t)$ from any known input signal $x(t)$, but this is a mathematically unstable procedure. A more stable procedure is to use a pseudostochastic maximum length sequence [142] as input function $x(t-\tau)$. The cross-correlation with the output signal $y(t)$ yields the response function $h(\tau)$.

$$\int_{-\infty}^{\infty} y(t) \bullet x(t+\tau)dt = h(\tau) \tag{7.5}$$

This is derived from the autocorrelation function of the pseudostochastic sequences, which approximate a delta-function

$$\int_{-\infty}^{\infty} x(t-\tau) \bullet x(t)dt = \delta(\tau) \tag{7.6}$$

The measured output function $y(t)$ at the position of the sample was determined with a small pick-up coil brought into the stray field of the resonator. It was made out of a 0.7 m length 2.2mm diameter semi rigid cable with a SMA connector soldered at one end. The coil itself consists of a half loop of the inner conductor soldered to the shield. The coil was located immediately at the end of the cable. A Miteq DB0418LW1 broadband mixer and a 350 MHz Tektronix TDS 5034B oscilloscope were used for detection (Fig. 7.2).

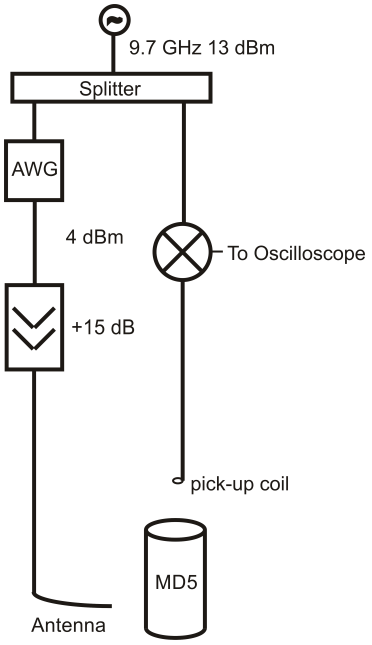

Figure 7.2: Pick-up coil test setup for measurement of the spin excitation function y(t) with the standard Bruker resonator MD 5.

The impulse response function $h(t)$ was determined with a maximum length sequence generated by a 13-bit linear feedback shift register with one XOR gate between position 12 and 13. The initial values have been set to: [1 0 1 0 0 0 1 1 0 0 0 0 1]. The step time of 1ns gives a total length of 8191 ns. The derived response function for the microwave excitations of the spins is shown in Fig. 7.3 a. To illustrate the frequency response of this excitation response function, the Fourier-Transform of $h(t)$ is depicted in Fig. 7.3

b. As can be seen most easily from the real part of the Fourier transform, $H(v)$, the excitation amplitude falls of very rapidly after a bandwidth of ±200 MHz, mainly due to the limited resonator bandwidth.

The experimental group of Prof. Prisner in Frankfurt want to investigate the feasibility of replacing classical hard pulses typically used in pulsed EPR with shaped optimal control pulses of the same peak B_1 amplitude to increase excitation bandwidth and improve performance. Experimental comparison is difficult and unreliable at frequencies where the resonator response approaches zero. Therefore, in the following applications, I design OCT pulses with a bandwidth of ±100 MHz, where the resonator has significant sensitivity, and utilize a reduced peak microwave excitation field strength of 12 MHz, corresponding to a 21 ns $\pi/2$ pulse.

7.4.2 Bandwidth optimized pulses for excitation

As a first test case for the application of optimal control pulses in EPR, the FT-EPR method is chosen . Bandwidth limitations and deadtime limit the application strongly. For the generation of magnitude mode spectra, the phase of the excited magnetization is irrelevant and hence the goal of the optimization is to maximize the transverse magnetization components, which is equivalent to minimizing the absolute value of the remaining z component of the magnetization vector at each offset within the desired bandwidth. This can be quantified using the quality factor ϕ_w of Eq. (3) with $F = (000)^t$ and $a_x = a_y = 0$, $a_z = 1$, resulting in $\phi_w(v_k, S_l) = M_z^2(T)$, which should be minimized. The corresponding adjoint state required for the GRAPE algorithm is given by $\lambda(T) = 2(00M_z)^t$. Each pulse of duration 500 ns was digitized in steps of 5 ns, resulting in 100 time slices j during which the control amplitudes $u_x(j)$ and are constant. A maximum value of $u_{max} = \sqrt{u_x^2(j) + u_y^2(j)} = 12$ MHz, corresponding to a microwave field amplitude B_1 of 0.43 mT (and a power of 160 W), was enforced using the clipping approach described in more detail in [26]. The following parameter ranges were used for offset and B_1 scaling factor s: $v_{off}^{min} = -100$ MHz, $v_{off}^{max} = 100$ MHz, $s^{min} = 0.95$, $s_{max}^{min} = 1.05$.

The total bandwidth of 200 MHz is about a factor of 4 broader than the excitation bandwidth of a classical $\pi/2$ pulse (with a length of 21ns at this MW power) as can be seen in Fig. 7.4. Fig. 7.4 c/c' shows the experimentally determined transverse signal magnitude for the classical $\pi/2$ pulse (a) and for the optimal control pulse sequence (a') as a function of frequency offset. As can be seen, the optimal control pulse indeed excites a broader spectral width as compared to a classical $\pi/2$ pulse with same maximum microwave power. The energy delivered to the electron spin system is a factor of 10 larger for the optimal control sequence applied for a total time of 0.5μs For comparison, an extreme hard pulse amplitude of about 120 MHz compared to 12 MHz for the BEBOP sequence would be required to cover the same bandwidth with comparable fidelity (c.f. Fig. 7.4 b, ignoring transient effects), which would deliver the same energy to the sample as the optimal control pulse.

The average power of the optimal control pulse is forty percent of the maximum power. The signal intensity in Fig. 7.4 c is set to 1 for an on-resonant excitation of the electron spin. The amplitudes of the transverse magnetization signal detected after the optimal control pulse sequence have been normalized with the same procedure. Then the signal amplitudes of the 21 ns $\pi/2$ is compared with the 0.5 μs long optimal control pulse as a function resonance offset, after multiplying by the frequency response of the video amplifiers. Only the magnitude of the transverse magnetization is shown since the phase was not included in the optimization of the BEBOP (broadband excitation

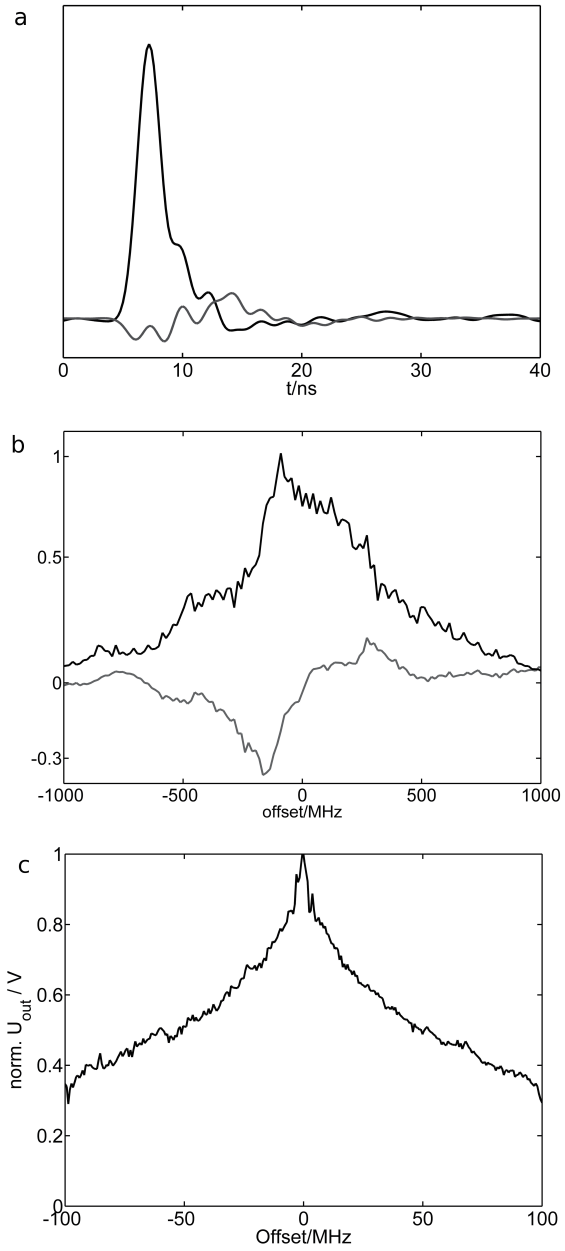

Figure 7.3: Frequency characterization of the spectrometer setup. 3a: Impulse response function and (3b) frequency response of the excitation path (black/grey real/imaginary). 3c: Frequency response of the video amplifiers set to 200MHz bandwidth.

by optimized pulses) sequence. Since the transverse magnetization decays right from the beginning of the pulse, the on-resonance signal of the BEBOP excited fluoranthenyl is 0.93 times smaller compared to the hard pulse. The loss of signal intensity at higher offsets is caused by the frequency response of the detection path dominated by the video amplifiers, as shown in Fig. 7.3 c. The influence of the resonator bandwidth itself, as shown in Fig. 7.3 b, plays a minor role for this reduced detection efficiency as a function of frequency offset in this case. Thus, very good agreement between theoretical predictions and experimental results has been obtained for the BEBOP pulse.

As a first application, the BEBOP pulse was then applied in a FT EPR experiment on PNT dissolved in paraffin oil. FID signals were recorded under the same experimental settings as described above. The same number of accumulations was chosen for BEBOP and rectangular $\pi/2$ excitation pulses. Fig. 7.5 shows the magnitude Fourier transform of the FID signals recorded 100ns after the end of the pulses. The maximum B_1 field strength was 4.3μT which corresponds to an on resonance Rabi nutation frequency of 12 MHz. For the two central lines, the FID signal detected after the BEBOP pulse is a factor of 0.6 smaller in overall signal amplitude.

Dividing the peak intensities of the lines appearing at -2.5 MHz and -38 MHz gives theoretically a factor of 3 (Fig. 7.5 a). The experimentally observed ratios of intensities, taking into account the frequency response of the video amplifier, are 3.8 and 9.3 for the BEBOP and rectangular pulse, respectively (Fig.7.5 b c). This is consistent with the simulated excitation performance shown in Fig. 7.4. More interesting is the comparison of the spectra taken with both excitations applied 53 MHz off-resonance. The spectrum taken with the rectangular $\pi/2$ pulse (Fig. 7.5 e) shows very strong distortions in the relative peak amplitudes of the hyperfine spectra of PNT, whereas the spectrum recorded with the optimal control pulse still gives a very good qualitative representation of the expected signal intensities (Fig. 7.5 d). In both cases the signal loss due to relaxation of the optimal control spectra is more than compensated by the large signal loss of the 21 ns $\pi/2$ pulse for offsets greater than 40 MHz, as shown in Fig. 7.5 e.

7.4.3 Prefocused pulse

Due to their narrower linewidth, it is in general preferable to acquire phase-sensitive spectra rather than magnitude-mode spectra. In contrast to excitation pulses with arbitrary phase considered in the previous section, this application requires excitation pulses that create transverse magnetization with a defined constant slope of the phase ϕ as a function of offset. The normalized, dimensionless phase slope R is defined as [143]

$$R = T^{-1}\partial\phi/\partial\omega_{off} = (2\pi T)^{-1}\partial\phi/\partial v_{off} \tag{7.7}$$

Ideally, an excitation pulse should have a normalized phase slope $R = 0$, in order to align all magnetization vectors at the end of the pulse. However, after an excitation pulse the resulting FID cannot be directly measured due to the finite dead time Δ_d of about 50-100 ns for X-band frequencies, during which the detected signal is distorted by resonator ringing caused by the microwave pulse.

One approach to align the transverse magnetization vectors for all resonance offsets after the dead time, i.e. to form an echo, is to use a broadband excitation pulse with $0 \leq R \leq 1$ [143], followed by a delay $\Delta_d - RT$ and an ideal refocusing pulse, which rephases all transvers magnetization components at the time Δ_d after the end of the refocusing pulse. However, the problem of this approach is that the bandwidth of conventional rectangular refocusing pulses is quite limited (on the order of the maximum pulse amplitude). Although refocusing pulses with larger bandwidth can be designed

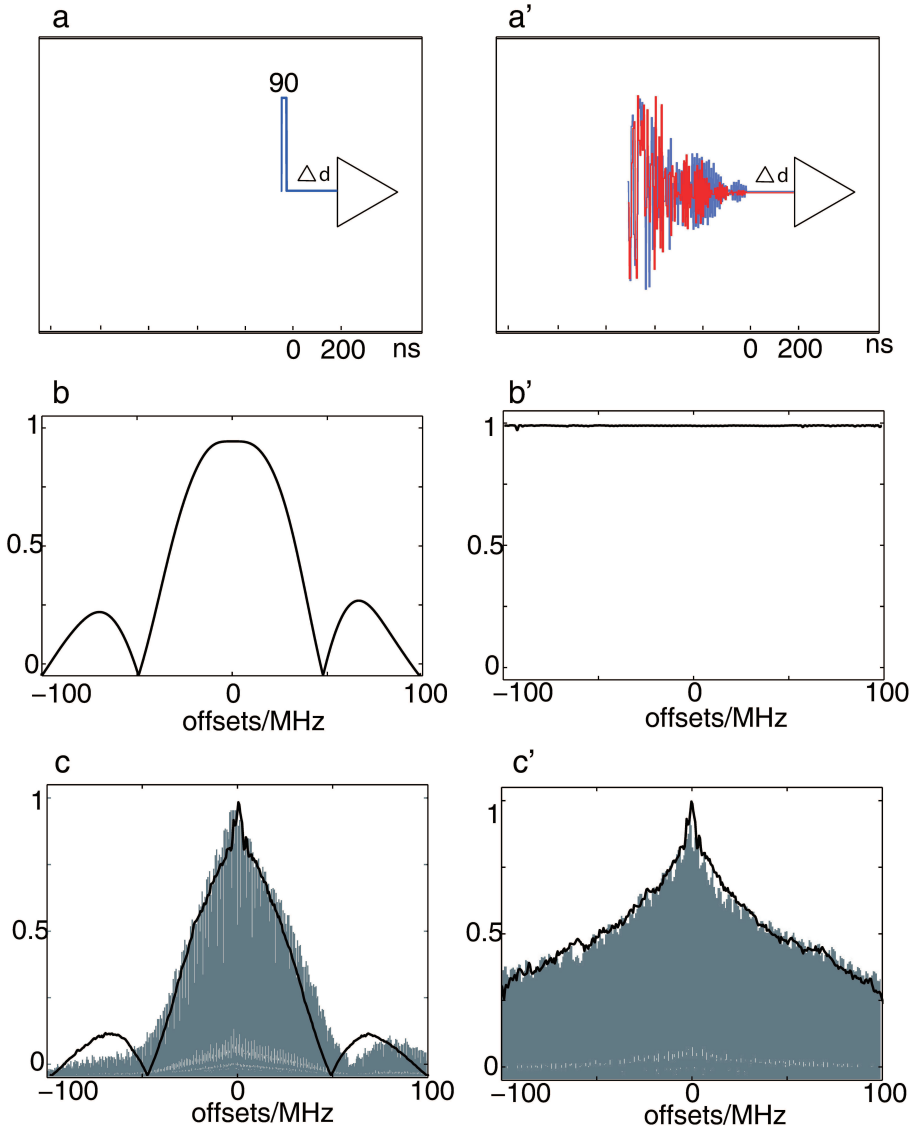

Figure 7.4: Comparison of a conventional rectangular pulse (left column) and the optimized BEBOP (broadband excitation by optimized pulses) [25]. The panels in the first row show the pulse shapes. The panels in the second row (b, b) show the simulated magnitude of the excited transverse magnetization. The black curves in the third row (c, c) represent the simulated magnitude of the transverse magnetization multiplied by the measured frequency response of the video amplifier. The grey lines in c and c' represent experimental magnitude mode spectra

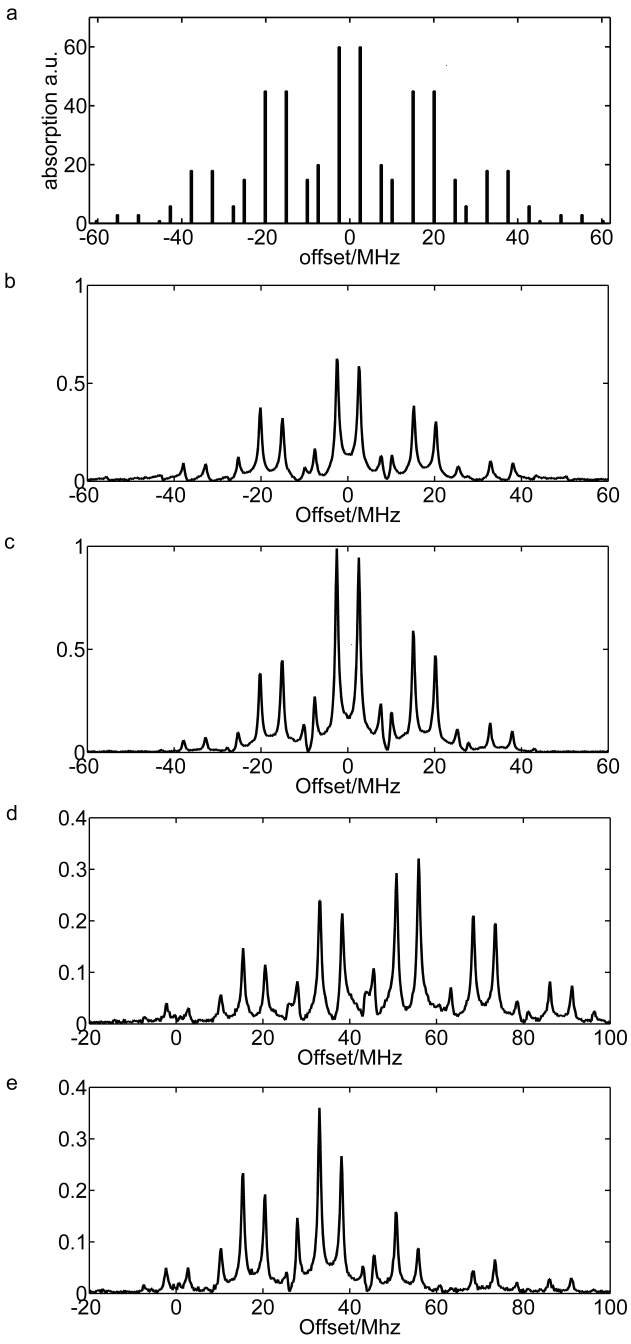

Figure 7.5: Magnitude Fourier Transform spectra of 1 mM PNT in paraffin oil measured at room temperature. Stick-diagram of hyperfine spectra (a). Experimental spectra excited in the center of the EPR spectra with the BEBOP sequence (b) and with a 20ns $\pi/2$ pulse (c). Experimental spectra excited 53 MHz off-resonance from the center of the EPR spectra with the BEBOP sequence (d) and with a 21ns $\pi/2$ pulse (e)

using optimal control based numerical algorithms such as GRAPE or constructed from broadband excitation pulses [144], the duration T_r of a refocusing pulse with similar bandwidth and quality as the excitation pulse is expected to be on the order of $2T$, where T is the duration of the excitation pulse. Hence, for this approach, the minimum time between the end of the excitation pulse and the time of the echo is given by $2\Delta_d - RT + T_r \approx 2\Delta_d + T(2 - R)$, which may result in substantial signal loss due to relaxation.

An alternative approach, is to design an excitation pulse with a negative normalized phase slope $R = -\Delta_d/T$, which will create an echo after the delay time Δ_d (i.e. after the dead time) and without the need for additional pulses [143] (see Fig. 7.6).

Excitation pulses with $R < 0$ can be viewed as an optimal combination of excitation and refocusing pulse in a single monolithic pulse with a given maximum pulse amplitude. As shown in [143], a pulse with a desired phase slope R can be optimized using the offset dependent target state

$$F(v_{off}) = [\cos(2\pi v_{off} RT), \sin(2\pi v_{off} RT), 0]^t \tag{7.8}$$

in the definition of the local quality factor ϕ_P or ϕ_w(c.f. Eqs. 2 and 3). The optimizations choses a pulse of duration 1μs which was digitized in steps of 1 ns, resulting in 1000 time slices j during which the control amplitudes $u_x(j)$ and $u_y(j)$ are constant. $R = -0.2$ is chosen, resulting in a delay between the end of the pulse and the echo formation of 200 ns. In order to minimize relaxation losses during the pulse duration of 1μs The relaxation can be included in the optimization as described in [29]. A maximum pulse amplitude of $u_{msx} = 20$ MHz was chosen and the optimized bandwidth was 200 MHz, corresponding to $v_{off}^{min} = -100$ MHz and $v_{off}^{max} = 100$ MHz. A B_1 inhomogeneity of $\pm 5\%$ was considered, corresponding to $s^{min} = 0.95$, $s^{max} = 1.05$. One approach to take into account the finite bandwidth of the probe is to restrict the largest frequency component of the pulse during the optimization [145]. The pulse shown in Fig. 7.7a was optimized using this approach to obtain a maximum bandwidth of 200 MHz, assuming it is delivered with ideal fidelity by the probe (grey line in Fig. 7.7c). However, the non-uniform frequency response of the probe at the lower frequencies comprising the pulse is still sufficient to degrade pulse output performance (black line in Fig. 7.7c). A more general approach, which allows best use of the available hardware characteristics, is discussed in the following.

7.4.4 Frequency-response-compensated pulses

Due to the finite response time of the resonator (related to the Q factor), the switching of pulse amplitude and phase during the pulse causes transient effects which result in amplitude and phase distortions of the ideal input pulse. The output pulse experienced by the electron spins can be quite different from the desired input pulse shape. The time scale of amplitude and phase transients can be described in terms of the bandwidth of the resonator. These transient effects are not significant in typical liquid-state NMR experiments performed with low-Q probes and can be neglected in designing pulses for such experiments. However, they need to be taken into account in the design of broadband EPR pulses, where typically the desired excitation bandwidth of a pulse is comparable to (or larger than) the bandwidth of the microwave transmission system including the resonator. As shown in [146], for any given input pulse, the corresponding output pulse can be predicted if the impulse response of the electronics is known (assuming a linear response system). Conversely, for any desired output pulse the corresponding input

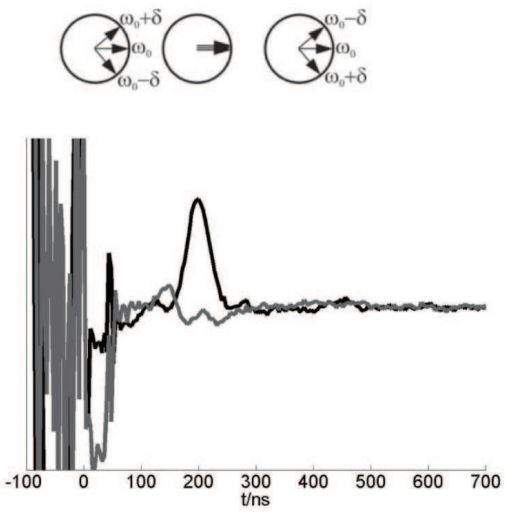

Figure 7.6: (top) Schematic representation of three spin packages in the transverse plane directly after the prefocused pulse sequence, 200 ns later, and 400 ns later, and (bottom) the experimentally observed in phase (black line) and quadrature (grey line) signal with such a pulse on a BDPA sample in polystyrene. The FID signal (echo) appears at the focus time for this sequence, which is chosen to be 200 ns after the end of the pulse.

pulse can be calculated [146]. However, the required input pulse may not be experimentally feasible e.g. because the required pulse amplitudes to be sent to the resonator may exceed the maximum amplitude provided by the pulse amplifiers. Therefore, the best approach is to take the impulse response into account in the optimization of the pulse, where constraints of input amplitude can be enforced. The relationship between the input pulse u^{in} and the output pulse u^{out} can be expressed as a convolution:

$$u^{out}(t) = h * u^{in} = \int h(\tau)u^{in}(t-\tau)d\tau \tag{7.9}$$

where $h(t)$ is the impulse response function. As discussed in the experimental section $h(t)$ can be determined experimentally by deconvoluting u^{out} (which can be measured using a pickup coil) with u^{in}. The Fourier transformation of u^{in}, h and u^{out} are related by $F(u^{out}) = F(h)F(u^{in})$ where, in the numerical calculation, u^{in} is extended by a delay corresponding to the duration during which the amplitude of the impulse response is not negligible.

Conventionally, GRAPE optimizations are based on the performance of the ideal input pulse u^{in}. In a modified version of the GRAPE algorithm, the input pulse u^{in} is optimized by maximizing the excitation profile of the resulting output pulse u^{out} . Here I used the local quality factor for the offset-dependent target state given in Eq. 7.2. Both the forward propagation of the initial magnetization $M(0)$ and the backward propagation of the adjoint $\lambda(T)$ is calculated using the output pulse u^{out}.

For each time slice j, the first order gradient of ϕ_P with respect to the output amplitudes $u_x^{out}(j)$ and $u_y^{out}(j)$ is given by

$$\frac{\partial \phi_P}{\partial u_x^{out}(j)} = M_y(j)\lambda_z(j) - M_z(j)\lambda_y(j) \tag{7.10}$$

$$\frac{\partial \phi_P}{\partial u_y^{out}(j)} = M_z(j)\lambda_x(j) - M_x(j)\lambda_z(j) \tag{7.11}$$

In order to update the input pulse u^{in}, one approach is to translate the gradient $\frac{\partial \phi_P}{\partial u_\alpha^{out}(j)}$ with respect to the output pulse into the corresponding gradient $\frac{\partial \phi_P}{\partial u_\alpha^{in}(j)}$ of the input pulse, using the impulse response function [145, 147]. Here I used the following equivalent approach: in each iteration, u^{out} is updated based on the gradient $\frac{\partial \phi_P}{\partial u_\alpha^{out}(j)}$ (e.g. by steepest descent with a small step size or by the conjugated gradient method) and the corresponding u^{in} is calculated by $u^{in} = F^{-1}(F(u^{out})/F(h))$. The constraint of the maximum allowed input pulse amplitude u_{max}^{in} is taken into account in each iteration by clipping the amplitude of u^{in} such that $u^{in}(j) \leq u_{max}^{in}$.

To summarize the procedure:
(1) create a (random) initial input pulse $u^{in(0)}$ of duration T
(2) for each iteration step k, translate the current input pulse $u^{in(k)}$ into the corresponding output pulse $u^{out(k)}$ with the help of the experimental response function h
(3) for all offsets v_k and scaling factors s_l
(a) evolve $M(t)$ forward in time under u_{out} starting from $M(0) = (001)^t$
(b) evolve $\lambda(t)$ backwards in time under u_{out} starting from $\lambda(T)$
(c) calculate the gradient $\frac{\partial \phi(v_k, s_l)}{\partial u_\alpha^{out}(j)}$
(4) calculate the overall gradient $\frac{\partial \Phi}{\partial u_\alpha^{out}(j)}$ by averaging the local gradient $\frac{\partial \phi(v_k, s_l)}{\partial u_\alpha^{out}(j)}$ for all offsets v_k and scaling factors s_l
(5) update $u^{out(k)}(j) \rightarrow u^{out(k+1)}(j) = u^{out(k)}(j) + \epsilon \frac{\partial \Phi}{\partial u_\alpha^{out}(j)}$ where ϵ is a small step size
(6) calculate the corresponding $u^{in(k+1)}$ from $u^{out(k+1)}$ with the help of the experimental response function h
(7) clip the amplitude of $u^{in(k+1)}$ if the maximum amplitude u_{max}^{in} is exceeded, i.e. if $u^{in}(j) > u_{max}^{in}$, set $u^{in}(j) = u_{max}^{in}$
(8) repeat steps (2)-(7) until a desired convergence of Φ is reached.

The efficiency of the procedure described above was tested with the fluoranthenyl sample for offsets ranging from −40 MHz to +40 MHz. Fig. 7.7 shows the comparison between a Hahn echo sequence with rectangular pulses (first column), the prefocused pulse sequence (second column) and the pre-compensated prefocused pulse sequence which takes the impulse response function (Fig. 7.3 a) into account during optimization (third column).

In the first row of Fig. 7.7, the x-component (in blue) and the y-component (in red) of the input pulse are depicted. The second row shows the simulated output pulse, as modified by the response function. The calculated x-magnetization 200 ns after the pulse is shown in the third row of Fig. 7.7. The grey line shows the performance of an input pulse from the first row, assuming it is delivered with ideal fidelity by the instrumentation. The black line represents the performance of the actual output pulse delivered to the sample. As illustrated in Fig. 7.7 c', the almost ideal performance (grey) of the faithfully delivered input pulse is severely distorted (black) by these hardware limitations. When this anticipated distortion is quantified by measuring the input response function, it can be designed into the pulse presented in the third column. Now, the performance (grey, Fig. 7.7 c") of this input pulse from row one, assumed to be unaffected by the instrumentation, is severely degraded compared to the desired performance, but the performance (black) of the actual output pulse from row two approaches the ideal. In the last row, the performance of the actual output pulse plotted in black in row three is multiplied by the measured frequency response of the video amplifier and again plotted in black. This simulates the frequency profile of the measured signal, including

instrumental effects, resulting from application of the pulses in row two. Experimental cosine Fourier-transformed FID signals of the fluoranthenyl sample are plotted as grey lines in the last row of Fig. 7.7 for both prefocused pulses. There is resonable agreement between the theoretical and experimental performance of the pulses.

Although the hard pulses in column one are relatively unaffected by these instrumental effects, they perform over a very limited bandwidth which can be significantly extended using the shaped OCT pulse in column three. The comparison was made with the same B_1 amplitude to emphasize that this conclusion and possibility is relevant for a range of EPR applications currently employing hard pulses.

7.5 Discussion

I have designed pre-compensated pulses using optimal control theory that take into account instrumental modifications of the pulse between input and output. This input pulse is then distorted by the system hardware in the precise fashion that delivers the desired optimized pulse shape to the sample. Experiments described above are the first to demonstrate the potential of this method to improve the excitation bandwidth and overcome other limitations, as, for example the dead-time of the spectrometer. Our test experiments were all performed at X-band frequencies with a reduced MW power of approximately 160 W for the BEBOP sequence and 440 W for the prefocused pulse. This allowed a quantitative comparison with rectangular pulses of the same Microwave power, by reducing the limitations of resonator bandwidth. Additionally, optimal control pulses have to be performed in the linear regime of the high power microwave amplifier. Some of these limitations will become less severe at higher microwave frequencies, where the intrinsic resonator bandwidth by far exceeds the excitation bandwidth of rectangular pulses.

The BEBOP pulse was designed for a broadband (200 MHz) excitation of transverse magnetization of arbitrary phase. Comparison of the experimental results for the BEBOP pulse with a rectangular $\pi/2$ pulse, with the same microwave excitation field strength B_1 of 0.43 mT, showed significantly broader excitation bandwidth for the optimal control pulse. This provided FT-EPR spectra with much better reproducibility of the relative signal intensities, as demonstrated on a liquid PNT sample.

Experiments also tested a pre-focused optimal control pulse producing magnetization of constant phase at a focus time of 200 ns after the pulse. This pulse was applied to a solid BDPA sample. Indeed, an echo like FID signal could be recorded 200 ns after the end of this pulse. This allows comfortable detection of the signal after the typical spectrometer dead-time of approximately 50-100 ns, making the method very promising for FT-EPR.

Limitations mostly arise from the restricted bandwidth of the excitation and detection. The microwave resonator distorts the excitation substantially, introducing artifacts and holes in the excitation pattern, as shown in Fig. 7.7. I have shown this can be compensated by measuring the excitation transfer function and taking it into account in the optimization of the pulses, as described above and illustrated in Fig 7.7. Since the coil cannot be inserted directly into the resonator it is placed in the stray field. The measured field at this position differs from the field experienced by the spin in the resonator due to the superposition of MW modes in the probe and the resonator itself. In our case this deviation is small at least in a frequency range of 80 MHz as shown in Fig. 7.7. The bandwidth of the pick up coil itself does not affect the measurement in the frequency range of interest which was verified with a network analyzer.

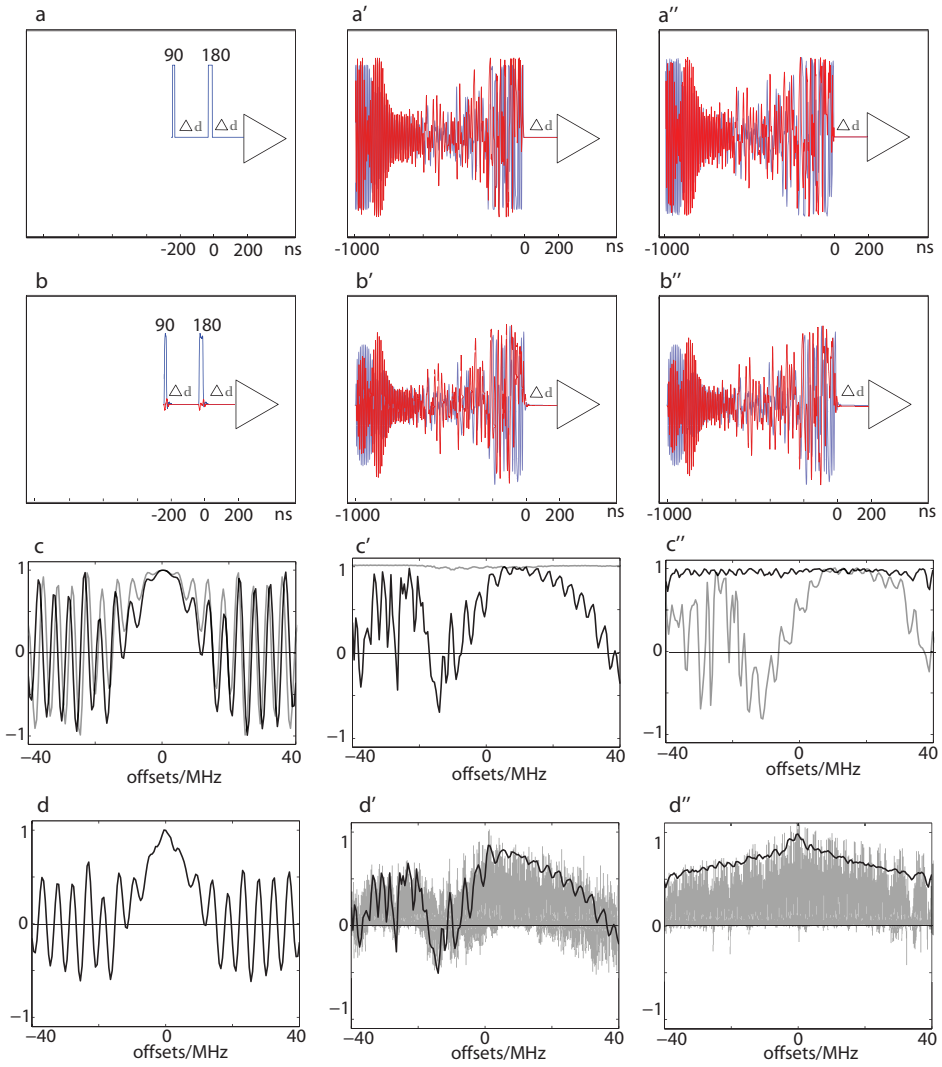

Figure 7.7: Compares conventional and optimized pulses designed to acquire self refocused signal 200 ns after the end of the last pulse. Signal (x-magnetization) is plotted as a function of resonance offset. The left column represents a conventional echo sequence based on rectangular 90° and 180° pulses. The middle and right columns represent results of optimizations without (middle column) and with (right column) compensation for instrumentinduced transient effects taken into account in the optimization. The panels in the first (a) and second (b) row show x- (red) and y-(blue) component of simulated input and output pulses, respectively. The third row (c) shows the simulated response for the input pulse (grey curves) and for the output pulse (black curves). Finally, the black curves in the fourth row (d, d', d") represent the simulated response of the output pulses multiplied by the measured frequency response of the video amplifier. In panels d' and d", experimental spectra are shown as grey curves.

Since the duration of the optimal control pulses providing increased bandwidth exceeds the length of classical rectangular pulses of the same B_1 amplitude, transverse relaxation can be even more important. In cases where the length of the OCT pulse becomes comparable to the relaxation time, compensation for relaxation has to be addressed in the optimization procedure, as described above. Higher available microwave power will shorten the length of OCT pulses for a given performance, but only by the square-root of the power. For this first application of optimal control theory to EPR, pulses were designed assuming uncoupled electron spins. Applying such pulse sequences to electronic spin systems with large anisotropic hyperfine couplings will lead to artifacts, especially for cancellation conditions. Again, these problems will be less severe at high microwave frequencies, where the nuclear Zeeman splitting exceeds the hyperfine couplings.

7.6 Summary

For the first time, optimal control theory was used to design broadband excitation pulses for EPR spectroscopy. To accommodate such sequences in a commercial pulsed X-band spectrometer, a fast amplitude and phase modulating unit has been designed and implemented. OCT broadband excitation pulse sequences have been tested and evaluated with this setup. Substantial gain in excitation bandwidth for a given microwave excitation field strength has been obtained. The pulses are also unique in that they transform magnetization as a function of resonance offset to the precise orientations in the transverse plane that subsequently precess and self-refocus during the dead-time of the EPR spectrometer detection channel. This allows dead-time free recording of the FID-signal in FT-EPR spectroscopy. Restrictions arising from the spectrometer response function are discussed and have been compensated by including this function in the optimization procedure. In addition, the pulses tolerate B_1 inhomogeneity of $\pm 5\%$. This requires a particular pulse shape that is more than difficult, if not impossible, to determine by traditional methods based on intuition or symmetry arguments. The optimization mathematics provides a means for finding such a pulse out of the vast number of possible pulse shapes. Other pulses, such as inversion pulses, will be targets for OCT-derived pulses in the future. Additionally, this method can be applied to redesign whole pulse sequences, such as the four-pulse PELDOR sequence [148] or the double-quantum filtered EPR experiment [132], which strongly suffer from imperfect polarization and coherence transfer pathways of standard pulses.

Bibliography

[1] S. J. Glaser, T. Schulte-Herbrüggen, M. Sieveking, O. Schedletzky, N. C. Nielsen, O. W. Sørensen, and C. Griesinger. Unitary control in quantum ensembles, maximizing signal intensity in coherent spectroscopy. *Science*, 280:421, 1998.

[2] L. S. Pontryagin. *The mathematical theory of optimal processes*. John Wiley and Sons, New-York-London, 1962.

[3] B. Bonnard and M. Chyba. *Singular trajectories and their role in control theory in Mathématiques and Applications*, volume 40. Springer-Verlag, Berlin, 2003.

[4] V. Jurdjevic. *Geometric control theory*. Cambridge University Press, Cambridge, 1996.

[5] N. C. Nielsen, C. Kehlet, S. J. Glaser, and N. Khaneja. Optimal control methods in NMR spectroscopy. *Encyclopedia of Nuclear Magnetic Resonance*, 9:100, 2010.

[6] T. E. Skinner, T. O. Reiss, B. Luy, N. Khaneja, and S. J. Glaser. Tailoring the optimal control cost function to a desired output: application to minimizing phase errors in short broadband excitation pulses. *J. Magn. Reson.*, 172:17, 2005.

[7] V. F. Krotov. *Global methods in optimal control theory*. Marcel Dekker, New York, Basel, Hongkong, 1995.

[8] E. Pinch. *Optimal control and the calculus of variations*. Oxford University Press, Oxford, 1993.

[9] C.G. Broyden. The convergence of a class of double-rank minimization algorithms. *J. Inst. Maths. Appl.*, 6:76, 1970.

[10] R. Fletcher. A new approach to variable metric algorithms. *Comp. J.*, 13:317, 1970.

[11] M. Lapert, Y. Zhang, M. Braun, S. J. Glaser, and D. Sugny. Singular extremals for the time-Optimal control of dissipative spin 1/2 Particles. *Phys. Rev. Lett.*, 104:083001, 2010.

[12] M. Lapert, Y. Zhang, M. Braun, S. J. Glaser, and D. Sugny. Geometric versus numerical optimal control of a dissipative spin 1/2 particle. *Phys. Rev. A*, 82:063418, 2010.

[13] G. M. Bydder, J. V. Hajnal, and I. R. Young. MRI: Use of the inversion recovery pulse sequence. *Clinical Radiology*, 53:159, 1998.

[14] S. L. Patt and B. D. Sykes. Water eliminated fourier transform NMR spectroscopy. *J. Chem. Phys.*, 56:3182, 1972.

[15] U. Boscain and B. Piccoli. *Optimal syntheses for control systems on 2-D manifolds in Mathématiques and Applications*, volume 43. Springer-Verlag, Berlin, 2004.

[16] D. Sugny, C. Kontz, and H.R. Jauslin. Time-optimal control of a two-level dissipative quantum system. *Phys. Rev. A*, 76:023419, 2007.

[17] B. Bonnard and D. Sugny. Time-minimal control of dissipative two-level quantum systems: the integrable case . *SIAM J. on Control and Optimization*, 48:1289, 2009.

[18] B.Bonnard, M. Chyba, and D. Sugny. Time-minimal control of dissipative two-level quantum systems: the generic case . *IEEE Transactions on Automatic control*, 54:2598, 2009.

[19] D. Sugny and C. Kontz. Optimal control of a three-level quantum system by laser fields plus von Neumann measurements. *Phys. Rev. A*, 77:063420, 2008.

[20] B. Bonnard, O. Cots, N. Shcherbakova, and D. Sugny. The energy minimization problem for two-level dissipative quantum systems. *J. Math. Phys.*, 51:092705, 2010.

[21] U. Boscain and B. Piccoli. *A short introduction to optimal control: controle non lineaire et applications*. LES COURS DU CIMPA, Paris, 2005.

[22] D. Sugny. Geometric optimal control of simple quantum systems. *Adv. Chem. Phys.*, 147:127, 2011.

[23] M. Lapert, Y. Zhang, S. J. Glaser, and D. Sugny. Towards the time-optimal control of dissipative spin 1/2 particles in Nuclear Magnetic Resonance. *J. Phys. B*, 44:154014, 2011.

[24] B. Bonnard and D. Sugny. *Optimal control with applications in space and quantum dynamics*, volume 5. American Institute of Mathematical Sciences, Springfield, 2012.

[25] T. E. Skinner, T. O. Reiss, B. Luy, N. Khaneja, and S. J. Glaser. Application of optimal control theory to the design of broadband excitation pulses for high resolution NMR. *J. Magn. Reson.*, 163:8, 2003.

[26] T. E. Skinner, T. O. Reiss, B. Luy, N. Khaneja, and S. J. Glaser. Reducing the duration of broadband excitation pulses using optimal control with limited RF amplitude. *J. Magn. Reson.*, 167:68, 2004.

[27] K. Kobzar, T. E. Skinner, N. Khaneja, S. J. Glaser, and B. Luy. Exploring the limits of broadband excitation and inversion pulses. *J. Magn. Reson.*, 170:236, 2004.

[28] T. E. Skinner, K. Kobzar, B. Luy, R. Bendall, W. Bermel, N. Khaneja, and S. J. Glaser. Optimal control design of constant amplitude phase-modulated pulses: application to calibration-free broadband excitation. *J. Magn. Reson.*, 179:241, 2006.

[29] N. I. Gershenzon, K. Kobzar, B. Luy, S. J. Glaser, and T. E. Skinner. Optimal control design of excitation pulses that accomodate relaxation. *J. Magn. Reson.*, 188:330, 2007.

[30] A. Bryson Jr. and Y.-C. Ho. *Applied optimal control*. Hemisphere, Washington, DC, 1975.

[31] D. Goldfarb. A family of variable metric updates derived by variational means. *Math. Comp.*, 24:23, 1970.

[32] D.F. Shanno. Conditioning of quasi-newton methods for function minimization. *Math. Comp.*, 24:647, 1970.

[33] T. Schulte-Herbrüggen, A. Spörl, and S. J. Glaser N. Khaneja. Optimal control-based efficient synthesis of building blocks of quantum algorithms seen in perspective from network complexity towards time complexity. *Phys. Rev. A*, 72:042331, 2005.

[34] H. Y. Carr and E. M. Purcell. Effects of diffusion on free precession in nuclear magnetic resonance experiments. *Phys. Rev.*, 94:630, 1954.

[35] S. Meiboom and D. Gill. Modified spin-echo method for measuring nuclear relaxation times . *Rev. Sci. Instr.*, 29:688, 1958.

[36] Navin Khaneja, Roger Brockett, and Steffen J. Glaser. Time optimal control in spin systems. *Phys. Rev. A*, 63(3):032308, 2001.

[37] Navin Khaneja, Steffen J. Glaser, and Roger Brockett. Sub-riemannian geometry and time optimal control of three spin systems: quantum gates and coherence transfer. *Phys. Rev. A*, 65(3):032301, 2002.

[38] Haidong Yuan and Navin Khaneja. Time optimal control of coupled qubits under nonstationary interactions. *Phys. Rev. A*, 72:040301, 2005.

[39] Y. Zhang, M. Lapert, M. Braun, D. Sugny, and S. J. Glaser. Time-optimal control of spin 1/2 particles in the presence of radiation damping and relaxation. *J. Chem. Phys.*, 134:054103, 2011.

[40] H. Mabuchi and N. Khaneja. Principles and applications of control in quantum systems. *International Journal of Robust and Nonlinear Control*, 15:647, 2005.

[41] S. Bloom. Effects of radiation damping on spin dynamics. *J. Appl. Phys.*, 28:800, 1957.

[42] W. S. Warren, S. L. Hammes, and J. L. Bates. Dynamics of radiation damping in nuclear magnetic resonance. *J. Chem. Phys.*, 91:5895, 1989.

[43] A. Vlassenbroek, J. Jeener, and P. Broekaet. Radiation damping in high resolution liquid NMR: A simulation study. *J chem. Phys.*, 103:5886, 1985.

[44] D. E. Rourke. Solutions and linearization of the nonlinear dynamics of radiation damping. *Concepts in Magnetic Resonance*, 14:112, 2002.

[45] M. P. Augustine. Transient properties of radiation damping. *Process in Nuclear Magnetic Resonance Spectroscopy*, 40:111, 2002.

[46] M. P. Augustine and E. L. Hahn. Radiation damping with inhomogeneous broadening: limitations of the single bloch vector model. *Concepts in Magnetic Resonance*, 13:1, 2001.

[47] N. Khaneja, T. Reiss, C. Kehlet, T. Schulte-Herbrüggen, and S. J. Glaser. Optimal control of coupled spin dynamics: design of NMR pulse sequences by gradient ascent algorithms. *J. Magn. Reson.*, 172:296, 2005.

[48] E. L. Hahn. Spin echoes. *Phys. Rev.*, 80:580, 1950.

[49] X. Mao, J. Guo, and C. Ye. Radiation damping effects of transverse relaxation time measurements . *Chem Phys Letters*, 227:65, 1994.

[50] X. Mao, J. Guo, and C. Ye. Radiation damping effects of spin-lattice relaxation time measurements . *Chem Phys Letters*, 222:417, 1994.

[51] W. Zhu, J. Botina, and H. Rabitz. Rapidly convergent iteration methods for quantum optimal control of population . *J. Chem. Phys.*, 108:1953, 1998.

[52] W. Zhu and H. Rabitz. Noniterative algorithms for finding quantum optimal controls. *J. Chem. Phys.*, 110:7142, 1999.

[53] D. Sugny, C. Kontz, M. Ndong, Y. Justum, and M. Desouter-Lecomte. Laser control in a bifurcating region. *Phys. Rev. A*, 74:043419, 2006.

[54] D. Sugny, M. Ndong, D. Lauvergnat, Y. Justum, and M. Desouter-Lecomte. Laser control in open molecular systems: STIRAP and optimal control. *J. Photochem. Photobiol. A*, 190:359, 2007.

[55] I. I. Maximov, J. Salomon, G. Turinici, and N. C. Nielsen. A smoothing monotonic convergent optimal control algorithm for nuclear magnetic resonance pulse sequence design . *J. Chem. Phys.*, 132:084107, 2010.

[56] M. Lapert, R. Tehini, G. Turinici, and D. Sugny. Monotonically convergent optimal control theory of quantum systems with spectral constraints on the control field. *Phys. Rev. A*, 79:063411, 2009.

[57] Y. Zhang, S. S. Köcher, M. Reddy, S. Caldarelli, and S. J. Glaser. Excitation of maximum quantum coherence: physical limits and practical pulse sequences. *in preparation.*

[58] Richard R. Ernst, Geoffrey Bodenhausen, and Alexander Wokaun. *Principles of nuclear magnetic resonance in one and two dimensions.* Clarendon Press, Oxford, 1987.

[59] W. P. Aue, E. Bartholdi, and R. R. Ernst. Two-dimensional spectroscopy. Application to nuclear magnetic resonance. *J. Chem. Phys.*, 64:2229, 1976.

[60] G.Bodenhausen. Multiple-quantum NMR. *Prog. NMR Spectrosc.*, 14:137, 1980.

[61] L. Braunschweiler, G. Bodenhausen, and R. R. Ernst. Analysis of networks of coupled spins by multiple quantum NMR. *Mol. Phys.*, 48:535, 1983.

[62] M. Munowitz and A. Pines. Multiple-quantum nuclear magnetic resonance spectroscopy. *Science*, 233:525, 1986.

[63] G. N. M. Reddy and S. Caldarelli. Demixing of severely overlapping NMR spectra through multiple-quantum NMR. *Anal. Chem.*, 82:3266, 2010.

[64] G. N. M. Reddy and S. Caldarelli. Maximum Quantum (MaxQ) NMR for the speciation of mixtures of phenolic molecules. *Chem. Comm.*, 47:4297, 2011.

[65] G. N. M. Reddy and S. Caldarelli. Identification and quantification of EPA 16 priority polyxyclic aromatic hydrocarbon pollutants by Maximum-Quantum NMR. *Analyst*, 137:741, 2012.

[66] M. H. Levitt and R. R. Ernst. Composite pulses constructed by a recursive expansion procedure. *J. Magn. Reson.*, 55:247, 1983.

[67] M. H. Levitt and R. R. Ernst. Multiple-quantum excitation and spin topology filtration in high-resolution NMR. *J. Chem. Phys.*, 83:3297, 1985.

[68] O. W. Sørensen. Polarization transfer experiments in high-resolution NMR spectroscopy. *Prog. NMR Spectrosc.*, 21:503, 1989.

[69] J. Stoustrup, O. Schedletzky, S. J. Glaser, C. Griesinger, N. C. Nielsen, and O. W. Sørensen. A Generalized bound on quantum dynamics: efficiency of unitary transformations between non-Hermitian states. *Phys. Rev. Lett.*, 74:2921, 1995.

[70] M. Sattler, J. Schleucher, and C. Griesinger. Heteronuclear multidimensional NMR experiments for the structure determination of proteins in solution employing pulsed field gradients. *Prog. NMR Spec.*, 34:93, 1999.

[71] Z. Tošner, T. Vosegaard, C. T. Kehlet, N. Khaneja, S. J. Glaser, and N. C. Nielsen. Optimal control in NMR spectroscopy: numerical implementation in SIMPSON. *J. Magn. Reson.*, 197:120, 2009.

[72] S. Machnes, U. Sander, S. J. Glaser, P. de Fouquières, A. Gruslys, S. Schirmer, and T. Schulte-Herbrüggen. Comparing, optimising and benchmarking quantum control algorithms in a unifying programming framework. *Phys. Rev. A*, 84:022305, 2011.

[73] P. de Fouquieres, S. G. Schirmer, S. J. Glaser, and I. Kuprov. Second order gradient ascent pulse engineering. *J. Magn. Reson.*, 212:241, 2011.

[74] K. Kobzar, T. E. Skinner, N. Khaneja, S. J. Glaser, and B. Luy. Exploring the limits of broadband excitation and inversion: II. Rf-power optimized pulses. *J. Magn. Reson.*, 194:58, 2008.

[75] J. L. Neves, B. Heitmann, T. O. Reiss, H. H. R. Schor, N. Khaneja, and S. J. Glaser. Exploring the limits of polarization transfer efficiency in homonuclear three spin systems. *J. Magn. Reson.*, 181:126, 2006.

[76] Nikolas Pomplun, Björn Heitmann, Navin Khaneja, and Steffen Glaser. Optimization of electron-nuclear polarization transfer. *Appl. Magn. Reson.*, 34:331, 2008.

[77] N. Pomplun and S. J. Glaser. Exploring the limits of electron-nuclear polarization transfer efficiency in three-spin systems. *Phys. Chem. Chem. Phys.*, 12:5791, 2010.

[78] M. Nimbalkar, R. Zeier, J. L. Neves, S. B. Elavarasi, H. Yuan, N. Khaneja, K. Dorai, and S. J. Glaser. Multiple-spin coherence transfer in linear ising spin chains and beyond: Numerically optimized pulses and experiments. *Phys. Rev. A*, 85:012325, 2012.

[79] T. Vosegaard, C. Kehlet, N. Khaneja, S. J. Glaser, and N. C. Nielsen. Improved excitation schemes for multiple-quantum magic-angle spinning for quadrupolar nuclei designed using optimal control theory. *J. Am. Chem. Soc.*, 127:13768, 2005.

[80] T. Schulte-Herbrüggen, A. Spörl, N. Khaneja, and S. J. Glaser. Optimal control for generating quantum gates in open dissipative systems. *Phys. Rev. B*, 44:154013, 2011.

[81] T. E. Skinner, N. I. Gershenzon, M. Nimbalkar, and S. J. Glaser. Optimal control design of band-selective excitation pulses that accommodate relaxation and RF inhomogeneity. *J. Magn. Reson., in press.*

[82] L. Braunschweiler and R.R. Ernst. Coherence transfer by isotropic mixing: Application to proton correlation spectroscopy. *J. Magn. Reson.*, 53:521, 1983.

[83] S. J. Glaser and J. J. Quant. Homonuclear and heteronuclear hartman-hahn transfer in isotropic liquids. In W. S. Warren, editor, *Advances in Magnetic and Optical Resonance*, volume 19, page 59. Academic Press, San Diego, 1996.

[84] A.J. Shaka, C.J. Lee, and A. Pines. Iterative schemes for bilinear operators; application to spin decoupling. *J. Magn. Reson.*, 77:274293, 1988.

[85] Navin Khaneja, Frank Kramer, and Steffen J. Glaser. Optimal experiments for maximizing coherence transfer between coupled spins. *J. Magn. Reson.*, 173(1):116, 2005.

[86] M. Lapert, Y. Zhang, M. Janich, S. J. Glaser, and D. Sugny. Exploring the physical limits of contrast in Magnetic Resonance Imaging. *submitted to Phys. Rev. Lett.*

[87] M. H. Levitt. *Spin dynamics: basics of nuclear magnetic resonance.* John Wiley and sons, New-York, 2008.

[88] M. A. Bernstein, K. F. King, and X. J. Zhou. *Handbook of MRI pulse sequences.* Elsevier, Burlington-San Diego-London, 2004.

[89] J. Pauly, P. Le Roux, D. Nishimura, and A. Macovski. Parameter relations for the Shinnar-Le Roux selective excitation pulse design algorithm. *IEEE Trans. Med. Imag.*, 10:53, 1991.

[90] G. M. Bydder and I. R. Young. MR Imaging: clinical use of the inversion recovery sequence. *Journal of Computed Assisted Tomography*, 9:659, 1985.

[91] M. Carl, M. Bydder, J. Du, A. Takahashi, and E. Han. Optimization of RF excitation to maximize signal and T2 contrast of tissues with rapid transverse relaxation. *Magnetic Resonance in Medicine*, 64:481, 2010.

[92] M. Chyba B. Bonnard and J. Marriotty. Singular trajectories and the contrast imaging problem in nuclear magnetic resonance . *submitted to SIAM J. Control. Opt.*

[93] D. O. Brunner and K. P. Pruessmann. B1 interferometry for the calibration of RF transmitter arrays . *Magn. Reson. Med.*, 61:1480, 2009.

[94] J. Frahm, A. Haase, and D. Matthaei. NMR imaging of dynamic processes using the FLASH technique . *Magn. Reson. Med.*, 3:321, 1986.

[95] Ph.E. Spindler, Y. Zhang, B. Endeward, N. Gershernzon, T.E. Skinner, S.J. Glaser, and T.F. Prisner. Shaped Optimal Control Pulses for Increased Excitation Bandwidth in EPR. *J. Magn. Reson.*, 218:49, 2012.

[96] R.R. Ernst and W.A. Anderson. Application of fourier transform spectroscopy to magnetic resonance. *Rev. Sci. Instrum.*, 37:93, 1966.

[97] P. Hu and S.R. Hartmann. Theory of spectral diffusion using an uncorrelated-sudden-jump model. *Phys. Rev. B*, 9:1, 1974.

[98] P.W. Anderson J.R. Klauder. Spectral diffusion decay in spin resonance experiments. *Physical Review*, 125:912, 1962.

[99] K.M. Salikov, D.J. Schneider, S. Saxena, and J.H. Freed. A theoretical approach to the analysis of arbitrary pulses in magnetic resonance. *Chem. Phys. Lett.*, 262:17, 1996.

[100] J. Baum, R. Tycko, and A. Pines. Broadband and adiabatic inversion of a two-level system by phase modulated pulses. *Phys. Rev. A*, 32:3435, 1985.

[101] M. H. Levitt. Composite pulses. *Prog. Nucl. Magn. Reson. Spectrosc*, 18:61122, 1986.

[102] R.R. Ernst. Nuclear magnetic double resonance with an incoherent radio-frequency field. *J. Chem. Phys.*, 45:3845, 1966.

[103] R.R. Ernst. Magnetic resonace with stochastic excitation. *J. Magn. Reson.*, 3:10, 1970.

[104] R. Kaiser. Coherent spectroscopy with noise signals. *J. Magn. Reson.*, 28:28, 1970.

[105] B. Bluemich and D. Ziessow. Nonlinear noise analysis in nuclear magnetic resonance spectroscopy. 1D, 2D, and 3D spectra. *J. Chem. Phys.*, 78:1059, 1983.

[106] J.D. Gezelter and R. Freeman. Use of neural networks to design shaped radiofrequency pulses. *J. Magn. Reson.*, 90:397, 1990.

[107] J.-M. Bohlen, I. Burghardt, M. Rey, and G. Bodenhausen. Frequency-modulated "Chirp" pulses for broadband inversion recovery in magnetic resonance. *J. Magn. Reson.*, 90:183, 1969.

[108] Ē. Kupče and R. Freeman. Adiabatic pulse for wideband inversion and broadband decoupling. *J. Magn. Reson.*, 115:273, 1995.

[109] L.A. O'Dell and R.W. Schurko. QCPMG using adiabatic pulses for faster acquisition of ultra-wideline NMR spectra. *Chemical Physics Letters*, 464:97, 2008.

[110] R. Bhattacharyya and L. Frydman. Quadrupolar nuclear magnetic resonance spectroscopy in solids using frequency-swept echoing pulses. *The Journal of Chemical Physics*, 127:194503, 2007.

[111] R.H. Crepeau, A. Dulcic, J. Gorcester, T.R. Saarinen, and J.H. Freed. Composite pulses in time domain ESR. *J. Magn. Reson.*, 84:184, 1989.

[112] T. Prisner and K.-P. Dinse. ESR with stochastic excitation. *J. Magn. Reson.*, 84:296, 1989.

[113] M. Fuhs, T.F. Prisner, and K. Mobius. Fourier transform EPR at high-field/high-frequency (3,4T/95GHz) using broadband stochastic microwave excitation. *J. Magn. Reson.*, 149:67, 2001.

[114] P.A.S. Cruickshank, D.R. Bolton, D.A. Robertson, R.I. Hunter, R.J. Wylde, and G.M. Smith. A kilowatt pulsed 94GHz electron paramagnetic resonance spectrometer with high concentration, high sensitivity, high instantaneous bandwidth, and low deadtime. *Rev. Sci. Instrum.*, 80:103102, 2009.

[115] R.H. Pursley, J. Kakareka, G. Salem, N. Devasahayam, S. Subramanian, R.G. Tschudin, M.C. Krishna, and T.J. Pohida. Stochastic excitation and Hadamard correlation spectroscopy with bandwidth extension in RF FT-EPR, Journal of Magnetic Resonance. *J. Magn. Reson.*, 62:35, 2003.

[116] N. Devasahayam, R. Murugesan, K. Matsumoto, J.B. Mitchell, J.A. Cook, S. Subramanian, and M.C. Krishna. Tailored sinc pulses for uniform excitation and artifact-free radio frequency time-domain EPR imaging. *J. Magn. Reson.*, 168:110, 2004.

[117] L.A. O'Dell, K.J. Harris, and R.W. Schurko. Optimized excitation pulses for the acquisition of static NMR powder patterns from half-integer quadrupolar nuclei. *J. Magn. Reson.*, 203:156, 2010.

[118] E. Assémat, M. Lapert, Y. Zhang, M. Braun, S. J. Glaser, and D. Sugny. Simultaneous time-optimal control of the inversion of two spin 1/2 particles. *Phys. Rev. A*, 82:013415, 2010.

[119] N. Khaneja, B. Luy, and S. J. Glaser. Boundary of quantum evolution under decoherence. *Proc. Natl. Acad. Sci. USA*, 100:13162, 2003.

[120] M. Braun and S. J. Glaser. Cooperative pulses. *J. Magn. Reson.*, 207:114, 2010.

[121] T. E. Skinner, M. Braun, K. Woelk, N. I. Gershenzon, and S. J. Glaser. Design and application of robust RF pulses for toroid cavity NMR spectroscopy. *J. Magn. Reson.*, 209:282, 2011.

[122] A. Schweiger and G. Jeschke. *Principles of pulse electron paramagnetic resonance.* Oxford University Press, Oxford, 2001.

[123] J.L. Davis and W.B. Mims. Use of a microwave delay line to reduce dead time in electron spin echo envelope spectroscopy. *Rev. Sci. Instrum.*, 52:131, 1981.

[124] G.A. Rinard, R.W. Quine, G.R. Eaton, and S.S. Eaton. 250 MHz crossed-loop resonator for pulsed electron paramagnetic resonance. *Concepts in Magnetic Resonance*, 15:37, 2002.

[125] T. Prisner, O. Dobbert, and K.P. Dinse. FT ESR study of photoinduced electron transfer. *J. Am. Chem. Soc.*, 110:1622, 1988.

[126] K.P. Dinse, M. Pluschau, G. Kroll, and T. Prisner. Photo-induced electron transfer reactions studied by fourier-transform ESR. *Bulletin of Magn. Reson.*, 11:174, 1989.

[127] T.F. Prisner and R.G. Griffin S. Un. FT-EPR at 140 GHz. *Israel Journal of Chemistry*, 32:357, 1992.

[128] T. Prisner, M. Rohrer, and K. Mobius. Pulsed 95 GHz high-field EPR heterodyne spectrometer with high spectral and time resolution. *Applied Magnetic Resonance*, 7:167, 1994.

[129] J.P. Hornak and J.H. Freed. Spectral rotation in pulsed ESR spectroscopy. *J. Magn. Reson.*, 67:501, 1986.

[130] J. Gorcester and J.H. Freed. Two-dimensional fourier transform ESR spectroscopy. *J. Chem. Phys.*, 85:5375, 1986.

[131] J. Gorcester and J.H. Freed. Two dimensional fourer transform correlation spectroscopy. *J. Chem. Phys.*, 88:4678, 1988.

[132] S. Saxena and J.H. Freed. Double quantum two dimensional Fourier transform electron spin resonance: distance measurements. *Chem. Phys. Lett.*, 251:102, 1996.

[133] P.B. Borbat and J.H. Freed. Multiple-qunatum ESR and distance measurements. *Chem. Phys. Lett.*, 313:145, 1999.

[134] P. Höfer, A. Grupp, H. Nebenfuhr, and M. Mehring. Hyperfine sublevel correlation (hyscore) spectroscopy: a 2D ESR investigation of the squaric acid radical. *Chem. Phys. Lett.*, 132:279, 1986.

[135] C. Gemperle, A. Schweiger, and R.R. Ernst. Electron-spin-echo envelope modulation with improved modulation depth. *Chem. Phys. Lett.*, 178:565, 1991.

[136] P. Schosseler, T. Wacker, and A. Schweiger. Pulsed ELDOR detected NMR. *Chem. Phys. Lett.*, 224:319, 1994.

[137] T. Wacker and A. Schweiger. Fourier-Transform EPR-detected NMR. *Chem. Phys. Lett.*, 186:27, 1991.

[138] T. Maly, F. MacMillan, K. Zwicker, N. Kashani-Poor, U. Brandt, and T.F. Prisner. Relaxation filtered hyperfine (REFINE) spectroscopy: A novel tool for studying overlapping biological electron paramagnetic resonance signals applied to mitochondrial complex I. *Biochemistry*, 43:3969, 2004.

[139] C. Kröhnke, V. Enkelmann, and G. Wegner. Radikalkationensalze einfacher Arene - eine neue Familie " organischer Metalle". *Angewandte Chemie*, 92:941, 1980.

[140] G. Sachs, W. Stocklein, B. Bail, E. Dormann, and M. Schwoerer. Electron spin relaxation of new organic conductors: fluroranthenyl radical cation salts. *Chem. Phys. Lett.*, 89:179, 1982.

[141] P.B. Sogo, M. Nakazaki, and M. Calvin. Free Radical from Perinaphthene. *J. Chem. Phys.*, 26:1343, 1957.

[142] D.D. Rife and J. Vanderkooy. Transfer-function measurement with maximum-length sequences. *J. Audio Eng. Soc.*, 37:419, 1989.

[143] N.I.Gershenzon, T.E.Skinner, B.Brutscher, N.Khaneja, M.Nimbalkar, B.Luy, and S.J.Glaser. Linear phase slope in pulse design: application to coherence transfer. *J. Magn. Reson.*, 192:235, 2008.

[144] B. Luy, K. Kobzar, T.E. Skinner, N. Khaneja, and S.J. Glaser. Construction of Universal Rotations from Point to Point Transformations. *J. Magn. Reson.*, 176:179, 2005.

[145] T.E. Skinner and N.I. Gershenzon. Optimal control design of pulse shapes as analytic functions. *J. Magn. Reson.*, 204:248, 2010.

[146] Y. Tabuchi, M. Negoro, K. Takeda, and M. Kitagawa. Total compensation of pulse transients inside a resonator. *J. Magn. Reson.*, 204:327, 2010.

[147] F. Motzoi, J.M. Gambetta, S.T. Merkel, and F.K. Wilhelm. Coarse-grained optimal control methods for fast time-varying Hamiltonians. *Phys. Rev. A.*, 64:022307, 2011.

[148] M. Pannier, S. Veit, A. Godt, G. Jeschke, and H.W. Spiess. Dead-time free measurement of dipole.dipole interactions between slectron spins. *J. Magn. Reson.*, 142:331, 2000.

Acknowledgements

I want to give my deepest thanks to Prof. Steffen J. Glaser for offering me working in his group and for his exceptional supervision during my phD.

I would like to thank all my colleagues for creating the nice working environment in the last three years. Special thanks to Dr. Michael Braun and Dr. Martin Janich for their essential helps in my thesis.

I thank my theoretical collaborators Prof. Dominique Sugny, Dr. Marc Lapert and Elie Assemat, and my experimental collaborators Prof. Thomas Prisner and Philipp Spindler.

Finally, I am very grateful to my parents and friend.